universität
innsbruck

Building a Single-Frequency Diode Laser at 405 nm for Imaging of Potassium on the Blue Transition

Master Thesis

by

Dominic M. Delmonego, BSc.

Submitted to the Faculty of
MATHEMATICS, COMPUTER SCIENCE, and PHYSICS
of the University of Innsbruck

Supervisors:
Univ.-Prof. Dr. Rudolf Grimm, Institute of Experimental Physics
Dr. Emil Kirilov, Institute of Experimental Physics

October 2020

universität innsbruck

Eidesstattliche Erklärung

Ich erkläre hiermit an Eides statt durch meine eigenhändige Unterschrift, dass ich die vorliegende Arbeit selbständig verfasst und keine anderen als die angegebenen Quellen und Hilfsmittel verwendet habe. Alle Stellen, die wörtlich oder inhaltlich den angegebenen Quellen entnommen wurden, sind als solche kenntlich gemacht.

Die vorliegende Arbeit wurde bisher in gleicher oder ähnlicher Form noch nicht als Magister-/Master-/Diplomarbeit/Dissertation eingereicht.

Datum	Unterschrift

Abstract

Within the scope of this thesis a diode laser system was built to image potassium ^{40}K on the blue transition $4S_{1/2} \leftrightarrow 5P_{3/2}$ at a wavelength of 405 nm. A commercial laser diode utilizing a GaN semiconductor material is used as light source to realize an external-cavity diode laser (ECDL) in Littrow configuration by means of a diffraction grating. Priorly, an ECDL in cat-eye configuration is set up utilizing a narrow-band interference filter, which is conceptually superior in the areas of feedback stability and cavity misalignments. But turns out to exhibit a worse tunability in connection with the used low reflection coated laser diode.

The laser is locked to the blue transition from the ground state crossover to the $5P_{3/2}$ excited state of ^{39}K. The error signal is obtained via modulation transfer spectroscopy of a heated potassium vapour cell, whereas the sidebands are generated by means of an electro-optic modulator driven by a local oscillator with frequency $f \approx 1\,\mathrm{Mhz}$. With an acousto-optic modulator in double-pass configuration the light frequency is shifted to the imaging transition. Finally, first successful attempts of absorption as well as fluorescence imaging of ^{40}K on the blue transition are presented.

Contents

1 Introduction

As the building blocks of matter, such as protons, neutrons, and electrons, fermions are of peculiar interest and better understanding of interacting fermionic systems can, inter alia, help in developing explanations for high temperature superconductivity, imagine the technological impact of a superconductor easily feasible at room temperature. Direct experimental investigations of complex quantum systems is often not feasible or possible, e.g. probing microscopic effects of solid-state systems or the core of a neutron star. Hence, an ultracold quantum gas as a quantum simulator can provide an outstanding system with great controllability to study the laws of quantum mechanics, which come more and more into play when the inter-particle distance approaches the thermal de Broglie wavelength and the wave nature of particles becomes significant. Therefore in an atomic gas experiment one needs to reach ultra low temperatures, which has been greatly facilitated by the invention of the laser, more specifically the laser cooling of neutral atoms [1]. By means of laser radiation trapping mechanisms can be realized too [2–4], which is an essential precondition to reach the quantum-degenerate regime, which manifests in Bose-Einstein condensation of bosonic [5–7] and Fermi degeneracy of fermionic gases [8–10].

In the DyK experiment at the Institute of Experimental Physics in Innsbruck strongly interacting fermionic mixtures of dysprosium and potassium are studied [11]. These two species were chosen to meet certain considerations, some of them are:

- introduction of a mass-imbalance
- experimental accessibility, i.e. feasible transitions for laser cooling [12], broad Feshbach resonances[13]
- already brought to quantum degeneracy [14, 15]
- certain stable isotopes, which would add some flexibility

Thus, the two species ^{161}Dy and ^{40}K are chosen. With a mass ratio around four the imbalance is not too high to suffer from extensive three-body losses [16, 17], but high enough to exhibit an enhancement effect on the formation of exotic quantum phases or lead to new types of pairing mechanisms [18–22]. Furthermore, ^{161}Dy, as an open f-shell lanthanide, offers a high magnetic dipole moment in the very ground state, introducing dipolar scattering as an additional interaction mechanism compared to alkali metals. As a result, thermalization of a fermionic single species spin-polarized sample can be achieved at ultra low temperatures [23]. With non-magnetic atoms the Pauli exclusion principle suppresses the interaction of identical fermions by s-wave scattering, which is

the dominant partial wave in ultracold gases, where higher partial waves freeze out by reduction of the temperature. Nevertheless, ^{40}K can be sympathetically cooled via ^{161}Dy by s-wave interaction.

A schematic view of the vacuum apparatus used to generate the Dy-K mixture is depicted in Fig. 1.1. Thereby approximately 10^7 Dy and 2×10^5 K atoms, with a

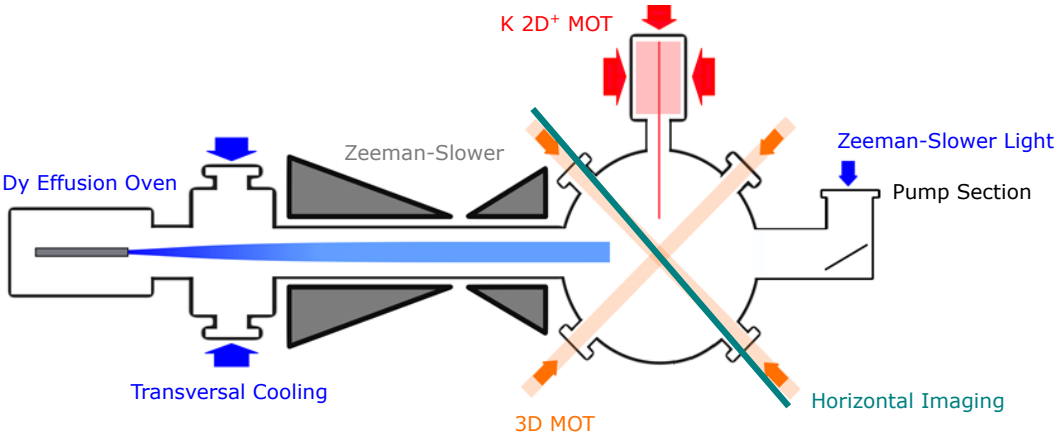

Figure 1.1: Schematic view of the main parts of the vacuum apparatus. From an effusion oven an atomic beam of dysprosium is first collimated by a transversal cooling stage (421 nm), then cooled via a Zeeman-Slower (421 nm) and guided to the main chamber, where the slow enough atoms are collected by a 3D MOT (626 nm). Potassium out of an enriched dispenser is gathered in a separate 2D$^+$ MOT (767 nm) and transported to the 3D MOT (767 nm) in the main chamber by a pushing beam via a differential pumping tube. After additional cooling mechanisms both species are sequentially loaded into a red-detuned optical dipole trap (not shown explicitly). Whereas potassium is held in the trap while dysprosium is loaded from the effusion oven. The atoms are imaged in the horizontal direction by means of absorption imaging. Along the vertical direction fluorescence imaging is utilized (not shown explicitly).

temperature of a few tens of µK and phase-space density around 10^{-4}, can been captured and spin-polarized in an optical dipole trap operated at $\lambda = 1070\,\text{nm}$. Then the mixture is loaded into a much narrower dipole trap operated at 1064 nm and cooled by ramping down the power in a two-step process, thus the atoms are cooled evaporatively and subsequently brought to degeneracy, whereby K is sympathetically cooled by Dy. Finally, the ^{161}Dy-^{40}K mixture can reach temperatures well below the Fermi temperatures $T_{\text{F, Dy}}$, $T_{\text{F, K}}$ of the corresponding species, with atom numbers at the higher end of 10^3, depending on the exact number ratio of the two species. As Dy is the cooling agent of K, the amount of K atoms strongly affect the evaporation process of Dy. For further details consider [24].

2 Motivation on the Blue Transition

Before I focus on the blue transition of potassium ^{40}K I first want to give a short overview on the topic of atom imaging itself and the experiment it will be used to. Then I state the level scheme of ^{40}K and describe the properties of the relevant transitions. Finally I focus on the possible advantages and disadvantages using the blue transition for resonant atom imaging.

2.1 Optical Imaging of Atoms

In the research field of ultracold atoms it is necessary to probe atomic clouds in order to study their behaviour. This can be done by optical diagnostics, where the atom-light interaction is exploited to gain information on the atoms. These interactions include absorption, re-emission, and phase-shift of the probe light which forms the base of the corresponding absorption, fluorescence, and dispersion imaging methods [4].

Thereby the atom cloud can be assumed as an dielectric medium, where the interaction with the light field, with frequency ω, is specified by the complex dielectric permittivity function $\varepsilon(\omega)$, related with the fundamental electromagnetic wave equation. By applying the *plane wave solution* the permittivity function can be split into a real and imaginary part, leading to the refractive index n_{ref} and extinction coefficient κ, consequently describing the dispersive and absorptive effect. But the relation is nontrivial, in particular $\varepsilon = (n_{\mathrm{ref}} + i\kappa)^2$. Here, one can also introduce the well-known complex index of refraction $n_{\mathrm{ref}}^{\mathrm{c}} = \sqrt{\varepsilon} = n_{\mathrm{ref}} + i\kappa$.

Now, considering a single atom the atomic polarizability α_{pol} is the parameter which connects the atom with an external field, moreover it is the proportionality factor[1] between the induced dipole moment and the electric field. From the quantum mechanics point of view the dipole moment is replaced by the dipole operator and the level structure of the atom has to be taken into account too. By assuming a two-level system (TLS) with ground $|g\rangle$ and excited state $|e\rangle$ separated by the transition energy $\hbar\omega_0$, one needs to consider the optical Bloch equations (OBE) to describe the interaction of an atom with a monochromatic light field, with frequency ω and the reduced Planck constant $\hbar$, adequately [25]. However, by just considering the steady state solution, the OBE break

[1] In detail it is a tensorial quantity, as the electric field and the dipole moment are complex vectorial quantities.

down into a simple rate equation and the excited state population $\rho_{\mathrm{ee}}^{\mathrm{ss}}$[2] is given by [25, 26]

$$\rho_{\mathrm{ee}}^{\mathrm{ss}} = \frac{\frac{1}{2}\frac{I}{I_{\mathrm{sat}}}}{1 + \frac{I}{I_{\mathrm{sat}}} + \left(\frac{\Delta}{\Gamma/2}\right)^2}, \tag{2.1}$$

with the natural decay rate $\Gamma = \tau_{\mathrm{eg}}^{-1}$, or inverse lifetime τ_{eg} of the excited to the ground state, the detuning $\Delta = \omega - \omega_0$ of the light field from the atomic resonance, the light intensity I and the saturation intensity I_{sat}. Furthermore the total photon scattering rate R_{sc} can be denoted by an exponential decay rate $R_{\mathrm{sc}} = \Gamma\rho_{\mathrm{ee}}^{\mathrm{ss}}$, just considering spontaneous emission and neglecting stimulated radiation. Now, the (optical) scattering cross section σ can be defined as the proportionality factor between the incident light intensity I and the - by the atom - scattered optical power σI. It is known that power equals energy per time and therefore the relation to the total photon scattering rate is $R_{\mathrm{sc}}\hbar\omega_0 = \sigma I$ and the scattering cross section becomes

$$\sigma(I) = \frac{\sigma_0}{1 + \frac{I}{I_{\mathrm{sat}}} + \left(\frac{\Delta}{\Gamma/2}\right)^2}, \tag{2.2}$$

with the on-resonance ($\Delta = 0$) cross section $\sigma_0 = {}^{\hbar\omega_0\Gamma}/_{2I_{\mathrm{sat}}}$ for a two-level atom. For circularly polarized light ($\sigma^{\pm}$) it further simplifies to $\sigma_0^{\sigma^{\pm}} = {}^{3\lambda^2}/_{2\pi}$, with $I_{\mathrm{sat}} = {}^{\hbar\Gamma c\pi}/_{3\lambda^3}$, the speed of light in vacuum c and the transition energy expressed as wavelength λ [25]. Moreover the cross section $\sigma(I)$ is indirectly dependent on the (x, z)-coordinates because of the spatial distribution of the incident beam $I(x, y, z)$, while y represents the beam propagation axis. But in the low intensity regime ($I \ll I_{\mathrm{sat}}$) the dependence of the cross section on the light intensity drops out:

$$\tilde{\sigma} = \frac{\sigma_0}{1 + \left(\frac{\Delta}{\Gamma/2}\right)^2} \tag{2.3}$$

and a simple description, where the probe beam is just attenuated and phase shifted, is possible. Additionally the cloud needs to be optically thin[3] along the optical axis too. This applies if re-absorption is negligible and therefore the atomic sample requires to be dilute along the y-direction. Then the column density $\tilde{n}(x, z)$ can be calculated by integrating the atom density distribution $n(x, y, z)$ along the light propagation axis: $\tilde{n}(x, z) = \int n(x, y, z)\,\mathrm{d}y$.

Let us now return to the idea of a complex index of refraction $n_{\mathrm{ref}}^{\mathrm{c}}$ and consider an ingoing well collimated[4] laser beam propagating in vacuum along the y-axis and sufficiently expanded to be considered as plane wave at the scale of the atomic cloud.

[2] The density operator $\boldsymbol{\rho}$ for a TLS written in the 2×2 matrix representation incorporates on the diagonal elements the ground and excited state population and on the off-diagonal elements the transition probabilities from ground to excited state and vice versa.

[3] In the topic of ray optics also known as thin lens approximation, where a lens is supposed to be thin when the incident ray exits the optical element at the same position (x, z) where it entered.

[4] Since a laser beam can be well approximated as a Gaussian beam, well collimated in this context supposes a Rayleigh length much longer than the extent of the object.

Also, if the changes of the refractive index of a medium are only small for distances compared to the wavelength, the medium can be considered to be locally homogeneous. This is satisfied by the assumption of optical thinness for now. Additionally the medium is assumed to be linear, isotropic, and (weakly) dispersive. Then the wave function has to obey the vectorial Helmholtz equation and a fundamental solution are plane waves:

$$\mathbf{E}(\mathbf{r},t) = \mathbf{E}_0 \mathrm{e}^{i(\mathbf{k}\cdot\mathbf{r}-\omega t)}, \tag{2.4}$$

with the wavevector $\mathbf{k}$, spatial position $\mathbf{r} = (x, y, z)$ and in general complex field amplitude $\mathbf{E}_0$. The dispersion relation is given by $k = n_{\mathrm{ref}}^{\mathrm{c}}\, \omega/c$, with the wavenumber $k = |\mathbf{k}|$. As the vectorial Helmholtz equation can be separated for each spatial component, it is sufficient to consider the scalar equivalent along the k-direction $\mathbf{k} = k \cdot \mathbf{e}_y$, with the unit vector $\mathbf{e}_y$ in y-direction:

$$E_y(y,t) = E_0 \mathrm{e}^{i(k\cdot y-\omega t)}, \tag{2.5}$$

with the incident scalar field amplitude E_0. After interaction with the object the electric field can again be described by a plane wave

$$E_y^{\mathrm{new}}(y,t) = E_0 t_{\mathrm{tr}} \mathrm{e}^{i(k\cdot y-\omega t+\varphi)} = E_y(y,t)\, t_{\mathrm{tr}}\, \mathrm{e}^{i\varphi}, \tag{2.6}$$

due to the assumptions made above, but with a change in amplitude and phase, indicated by the damping factor t_{tr} and phase shift φ, respectively. By considering the dispersion relation and the complex index of refraction of the medium the phasor can be written as

$$\mathrm{e}^{iky} = \exp\left(i\frac{\omega}{c} n_{\mathrm{ref}}^{\mathrm{c}} y\right) = \exp\left(-\frac{\omega}{c}\kappa y + i\frac{\omega}{c} n_{\mathrm{ref}} y\right). \tag{2.7}$$

Thereby the damping factor, which is also called the transmission coefficient, is expressed by the modulus of Eq. (2.7) and can be written in terms of a field absorption coefficient $\alpha_f = \frac{2\pi\kappa(\omega)}{\lambda_0} = k_0\kappa(\omega)$, or in terms of the absorption cross section $\tilde{\sigma}$ and density distribution n, whereas the extinction coefficient $\kappa(\omega)$ can be weakly dispersive and $\lambda_0 = {}^{2\pi}/_{k_0} = {}^{2\pi c}/_{\omega}$ denotes the vacuum wavelength. Integrating over the thickness of the medium Δy for a slowly varying refractive index yields [4]

$$t_{\mathrm{tr}} = \exp\left(-\int_{\Delta y} \alpha_f \,\mathrm{d}y\right) = \exp\left(-\int_{\Delta y} \frac{n\tilde{\sigma}}{2}\,\mathrm{d}y\right) = \exp\left(-\frac{\tilde{n}\tilde{\sigma}}{2}\right). \tag{2.8}$$

For a travelling wave the change of phase velocity inside a medium compared to the speed of light in vacuum generally leads to a phase shift φ, arising due to the change of the real part of the refractive index $n_{\mathrm{ref}}(\omega)$. For an atomic cloud near resonance the phase shift can be determined by [4]

$$\varphi = -\frac{\tilde{n}\tilde{\sigma}}{2}\frac{\Delta}{\Gamma/2}\,. \tag{2.9}$$

Hence, to obtain the density distribution of an atom cloud, in particular the column density $\tilde{n}(x,z)$, either the transmission coefficient $t_{\mathrm{tr}}(x,z)$ or the phase shift $\varphi(x,z)$ can be measured, represented by absorptive and dispersive imaging methods, respectively. Therefore (local) homogeneity and linearity is utilized to obtain the position dependent values of $t_{\mathrm{tr}}(x,z)$ and $\varphi(x,z)$ at a small area around the position (x,z).

2.1.1 Absorption Imaging

A camera, CCD or CMOS technology, is just sensitive to intensities and not the phase of electric fields, whereas the intensity of a (quasi-)monochromatic wave is defined by the absolute square of the complex field amplitude. Therefore Eq. (2.6) becomes

$$I = I_0 t_{\mathrm{tr}}^2 = I_0 e^{-\tilde{n}\tilde{\sigma}} = I_0 e^{-\tilde{\tau}}, \tag{2.10}$$

well known as Beer's law with the optical depth $\tilde{\tau} = \tilde{n}\tilde{\sigma} = -\ln(t_{\mathrm{tr}}^2) = \ln(I_0/I)$ and the corresponding light intensities $I_0 = |E_0|^2$, $I = |E_y^{\mathrm{new}}|^2$ before and after the medium. Often the optical density $OD = \tilde{\tau}/\ln(10) = \tilde{\tau}\log_{10}(\mathrm{e}^1)$ is used in this case, which is based on the common logarithm[5] as opposed to the natural logarithm, but this quantity is ambiguous as in this case actually the absorbance is meant for the optical density. Therefore the optical depth $\tilde{\tau}$ is used throughout this thesis.

Now, the atom cloud is illuminated by resonant laser light and the attenuated beam with intensity $I_{\mathrm{atoms}}(x, z)$ is recorded by a camera, illustrated in Fig. 2.1. The difference with a second picture, denoted by intensity $I_{\mathrm{laser}}(x, z)$, but without atoms results in the shadow cast by them. In order to account for camera dark current and other

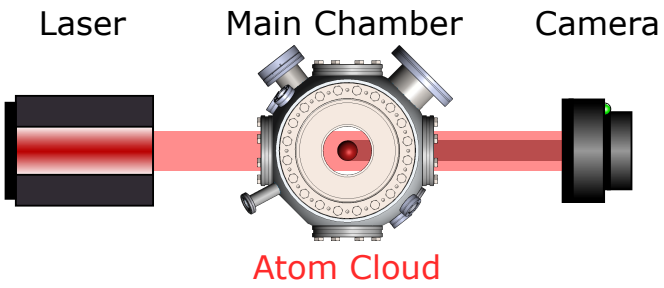

Figure 2.1: Schematic illustration of the absorption imaging method. All optical elements crucial for beam shaping and the camera objective are omitted for simplicity. The atom cloud is illuminated by a resonant laser source and the shadow cast by them is recorded by a camera aligned to it. From that the column density $\tilde{n}(x, z)$ of the atoms can be derived.

background light a third picture is taken without atoms and probe light, denoted by intensity $I_{\mathrm{bg}}(x, z)$. Then the optical depth $\tilde{\tau}(x, z)$ can be calculated with

$$\tilde{\tau}(x, z) = \ln\left[\frac{I_{\mathrm{laser}}(x, z) - I_{\mathrm{bg}}(x, z)}{I_{\mathrm{atoms}}(x, z) - I_{\mathrm{bg}}(x, z)}\right] \tag{2.11}$$

and so the column density $\tilde{n}(x, z)$ of the atom cloud. Therefore the cross section $\tilde{\sigma}$ needs to be known at the specific light parameters and atomic resonance. This reveals already the main advantage of the absorption imaging technique, namely the simplicity,

[5] logarithm with base 10

as there are in principle no elaborate calibrations necessary because only relative intensities need to be determined in Eq. (2.11) and all proportionality factors drop out if they are constant over time.

From the measured column density $\tilde{n}(x, z)$ the total atom number N can be determined by integrating over the spatial coordinates (x, z):

$$N = \iint_{\mathbb{R}^2} \tilde{n}(x, z)\,\mathrm{d}x\,\mathrm{d}z \approx \iint_{A_{\mathrm{im}}} \tilde{n}(x, z)\,\mathrm{d}x\,\mathrm{d}z\,, \tag{2.12}$$

assuming an imaging area A_{im} much larger than the extent of the atom cloud. To reconstruct the three-dimensional (3D) atom density distribution $n(x, y, z)$ one can either utilize the inverse Radon transform together with two-dimensional (2D) projections along an infinite number of angles [27], or if the atom cloud is cylindrically symmetric the inverse Abel transform [28]

$$n(\varrho, z) = -\frac{1}{\pi} \int_r^\infty \frac{\mathrm{d}\tilde{n}(x, z)}{\mathrm{d}x} \frac{1}{\sqrt{x^2 - \varrho^2}}\,\mathrm{d}x \tag{2.13}$$

can be applied, with the radial dimension $\varrho = \sqrt{x^2 - y^2}$ in the (x, y)-plane. For further informations consider [28, 27].

The exact imaging time, i.e. camera exposure time and laser pulse length, was not considered yet as it is not important for the principles of absorption imaging, but practically two opposing effects limit the possible time range. Short imaging pulses lead to a poor signal-to-noise ratio (SNR) and long pulses cause motion blurring of the imaged atoms and can induce a large amount of heat to the sample. The former is mostly due to photon shot noise limitation as well as camera read noise and the second due to Brownian motion of the atoms and multiple transfers of photon recoil energies [4]. To minimize the shot noise the number of scattered photons should be as high as possible, but for absorptive imaging techniques using resonant light this leads to a tremendous heating of the sample, as every absorbed photon transfers one recoil energy, classifying this approach as a destructive imaging method. Additionally re-absorption events must be kept low, which can be achieved by reducing the optical depth, either by reducing the cloud density due to free-flight expansion, considered in Section 2.1.3, or by using off-resonant light, considered in Section 2.1.4. Also high intensity absorption imaging can be utilized to diminish the effect of re-absorption due to saturation of the atoms in the first place [29].

The effect of motion blurring for long imaging times is especially relevant for detection of small features, e.g. vortices in a superfluid sample, or if the imaging system has a small depth of focus by using a microscope objective with a high numerical aperture (NA), which is usually the case to achieve high imaging resolutions. Then it further raises the necessity of a large number of scattered photons per atom, but now in a short amount of time and therefore high intensity absorption imaging is often favoured over the low intensity counterpart.

High Intensity Absorption Imaging

For higher intensities if saturation is not negligible, Beer's law in the simple form of Eq. (2.10) needs to be enhanced, as the cross section is no longer independent on the light intensity I. Additionally one has to keep in mind that in practise the two-level assumption for an atom is not strictly valid and the on-resonance cross section σ_0 depends on the polarization of the probe beam as well as on the structure and population of the atomic states, especially the Zeeman sublevels. Therefore a dimensionless parameter α is introduced to account for these effects, resulting in the effective saturation intensity $I_{\mathrm{sat}}^{\mathrm{eff}} = \alpha I_{\mathrm{sat}}$ and the effective resonant cross section $\sigma_0^{\mathrm{eff}} = {}^{\sigma_0}/_{\alpha}$. The corresponding differential equation reads as follows [30, 31]

$$\mathrm{d}I(x,z) = -n(x,y,z)\sigma_0^{\mathrm{eff}} \frac{1}{1 + \frac{I(x,z)}{I_{\mathrm{sat}}^{\mathrm{eff}}} + \left(\frac{\Delta}{\Gamma/2}\right)^2} I(x,z)\mathrm{d}y\,. \tag{2.14}$$

Integrating both sides along y leads to

$$\sigma_0^{\mathrm{eff}}\tilde{n}(x,z) = \left[1 + \left(\frac{\Delta}{\Gamma/2}\right)^2\right] \cdot \ln\left[\frac{I_{\mathrm{laser}}(x,z) - I_{\mathrm{bg}}(x,z)}{I_{\mathrm{atoms}}(x,z) - I_{\mathrm{bg}}(x,z)}\right] + \left[\frac{I_{\mathrm{laser}}(x,z) - I_{\mathrm{atoms}}(x,z)}{I_{\mathrm{sat}}^{\mathrm{eff}}}\right], \tag{2.15}$$

which correctly becomes Eq. (2.10) in the low intensity regime, where just relative intensities are relevant. But at high intensities they need to be determined in units of the effective saturation intensity and therefore a calibration is mandatory. For that purpose several approaches have been worked out [31–33], but Hueck et al. present a robust and precise technique to determine the effective saturation intensity and will be explained in the following [33]. But it requires an additional imaging axis perpendicular to the axis of the main imaging because this method analyses the momentum transferred by the imaging light on the main axis, schematically shown in Fig. 2.2. However, for probing atom clouds in ultracold experiments often two separate imaging systems are a priori implemented on different axes.

The signal output of each pixel with index (i,j) of a camera is given by the number of counts $C(i,j)$, which is proportional to the number of photons hitting this pixel and therefore proportional to the light intensity integrated over the pixel area A_{px}, divided by the photon energy $\hbar\omega$ and integrated over the exposure time t_0. Then the magnification of the imaging system M connects the intensity at the object plane with the intensity at the imaging plane and together with the overall conversion efficiency η, which incorporates the quantum efficiency (photons to photoelectrons), the conversion factor (photoelectrons to counts), and the transmission of the imaging system, the number of counts can be written as

$$C(i,j) = \frac{\eta}{M^2\hbar\omega} \int_{t_0} \iint_{A_{\mathrm{px}}} I(x,z)\,\mathrm{d}A\,\mathrm{d}t \;\approx\; \eta\,\frac{I(x_i,z_i)A_{\mathrm{px}}t_0}{M^2\hbar\omega}\,. \tag{2.16}$$

By assuming constant system parameters M, A_{px}, η, photon energies, and exposure time, the saturation intensity only needs to be determined as a count rate $C_{\mathrm{sat}}^{\mathrm{eff}}$, too and the enhanced Beer's law changes to

$$\sigma_0^{\mathrm{eff}}\tilde{n}(i,j) = \left[1+\left(\frac{\Delta}{\Gamma/2}\right)^2\right]\cdot\ln\left[\frac{C_{\mathrm{atoms}}(i,j)-C_{\mathrm{bg}}(i,j)}{C_{\mathrm{laser}}(i,j)-C_{\mathrm{bg}}(i,j)}\right]+\left[\frac{C_{\mathrm{laser}}(i,j)-C_{\mathrm{atoms}}(i,j)}{C_{\mathrm{sat}}^{\mathrm{eff}}}\right]. \quad (2.17)$$

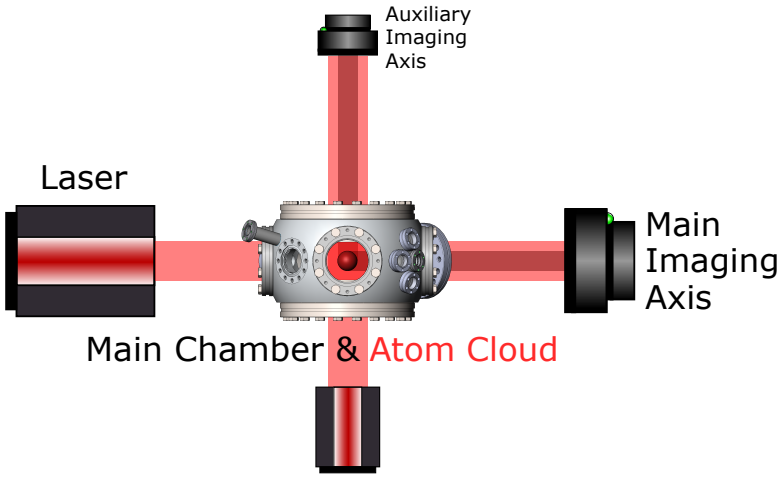

Figure 2.2: Schematic illustration of the calibration method for high intensity absorption imaging by Hueck et. all [33]. All optical elements crucial for beam shaping and the camera objective are omitted for simplicity. The atom cloud is illuminated by a resonant laser source on the main imaging axis and thereby travelling along this direction. With an auxiliary imaging system on an axis perpendicular to the main imaging axis the position after some time-of-flight is recorded. The light intensity I_{laser} of the accelerating beam is recorded as count rate C_{laser} by means of the main imaging camera which is going to be calibrated. By increasing the intensity I_{laser} the flight distance saturates and the effective saturation count rate $C_{\mathrm{sat}}^{\mathrm{eff}}$ can be determined.

Considering a trapped atom cloud which will be illuminated by a short resonant laser pulse on the main imaging axis (y-axis) after the trapping potentials are switching off. The transferred momentum of an atom along the y-direction is then given by the photon recoil momentum multiplied by the amount of scattered photons. Whereas the resonant photon scattering rate, regarding Eq. (2.1) with $\Delta = 0$, saturates with increasing intensity I_{laser} like

$$R_{\mathrm{sc},0}(I_{\mathrm{laser}}) = \frac{\Gamma}{2}\frac{s_0}{1+s_0}, \quad (2.18)$$

with the saturation parameter given by $s_0 = {}^{I_{\mathrm{laser}}}/_{I_{\mathrm{sat}}^{\mathrm{eff}}} = {}^{C_{\mathrm{laser}}}/_{C_{\mathrm{sat}}^{\mathrm{eff}}}$. After some time-of-flight (TOF) the atoms are recorded on an auxiliary imaging path oriented orthogonal

to the y-axis. The measured flight distance Δy is thereby proportional to the transferred momentum and subsequently the photon scattering rate R_{sc}. Accordingly,

$$\Delta y(I_{\mathrm{laser}}) \propto \frac{s_0}{1+s_0} \quad \longrightarrow \quad \Delta y(I_{\mathrm{laser}})\Big|_{I_{\mathrm{laser}}=I_{\mathrm{sat}}^{\mathrm{eff}}} = \frac{\Delta y_{\mathrm{max}}}{2} \tag{2.19}$$

the maximum flight distance $\Delta y_{\mathrm{max}} = \Delta y(I_{\mathrm{laser}} \gg I_{\mathrm{sat}}^{\mathrm{eff}})$ is related to the effective saturation intensity $I_{\mathrm{sat}}^{\mathrm{eff}}$ respectively count rate $C_{\mathrm{sat}}^{\mathrm{eff}}$. Quantitatively the flight distance is given by the displacement of the cloud center with and without prior TOF, determined by applying a Gaussian fit to the density profile recorded with the auxiliary system. Thus all parameters of the auxiliary system conveniently drop out as the count rate C_{laser} is measured at the main imaging system and $C_{\mathrm{sat}}^{\mathrm{eff}}$ can be determined by fitting Eq. (2.18) to the recorded data for various laser intensities I_{laser}.

By further including laser detuning ($\Delta \neq 0$) the functional dependence of the cloud position $y = y_0 + \Delta y$ can be described by

$$y(I_{\mathrm{laser}}, \Delta) = y_0 + \tilde{\eta}\frac{\Gamma}{2}\frac{s_0}{1 + s_0 + \left(\frac{\Delta}{\Gamma/2}\right)^2}, \tag{2.20}$$

with the (arbitrary) initial cloud position y_0 and conversion factor $\tilde{\eta}$, which incorporates the transformation between the scattering rate R_{sc} and the cloud position on the image plane. In this way the laser frequency can be calibrated too, by maximizing the cloud displacement. Furthermore this approach does not suffer from any influences on atom number fluctuations as well as lensing effects in a dense atom cloud [33].

But for higher intensities ($s_0 > 1$) the resonance with respect to the cloud displacement is blue-shifted due to the Doppler effect, but can be compensated by using a chirped laser pulse[6] on the main imaging axis. By choosing the right chirp rate the laser pulse stays resonant during the acceleration of the atoms and the cloud displacement can again be maximized to further improve the calibration. As a second approach Eq. (2.20) can be fitted to the recorded data for various laser intensities I_{laser} and detunings Δ, whereas $\tilde{\eta}$, s_0, and y_0 are left as fit-parameters. Comparing the fitted parameter s_0 to the corresponding C_{laser} reveals the effective saturation count rate $C_{\mathrm{sat}}^{\mathrm{eff}}$, too.

In Situ Absorption Imaging

By utilizing the TOF method, considered in Section 2.1.3, inter alia the momentum distribution of an atomic sample can be deduced. As a complement in situ imaging allows to extract spatial density properties directly while the atoms are in-trap, but thereby still influenced by the external potentials, which can be disadvantageous for the imaging, although it rises the possibility to study the influence of the density on a varying

[6] A chirped laser pulse put simply: incorporates light, which changes its frequency gradually with time, whereas increasing frequency is known as up-chirp and decreasing frequency as down-chirp, respectively.

potential. Thus new observables can be extracted more easily, e.g. density fluctuations and the density-density correlation function [29]. But the quantitative interpretation of an image is more difficult, as the spatially varying potential alters the atom-light interaction leading to spatially varying absorption properties. Another major issue with in situ absorption imaging is the high optical depth of the sample, which leads to a strongly nonlinear optical response and the assumptions made earlier prior Section 2.1.1 no longer hold. However, using (quasi-)2D samples oriented in parallel to the imaging plane and generated by a strong axial confinement, e.g. a narrow optical lattice, greatly reduce the optical density along the imaging direction. But therefore it is important, if an axial optical lattice is used, that the atomic sample occupies only a single lattice layer, which can be experimentally challenging to achieve.

In principle recording an in situ image is done analogously to the standard absorption imaging illustrated in Fig. 2.1. But due to the missing cloud expansion prior imaging, where the cloud diameter can be easily extended by an order of magnitude, a system with high NA is mandatory. As a result the depth of focus is strongly limited and the number of scattered photons per atom needs to be maximized, consequently. Thus high intensity imaging is utilized and the effect of motion blurring can be minimized with short imaging pulses or strongly trapped atoms. Additionally, saturation effects reduce the influence on re-absorption and multiple scattering events drastically, otherwise nonlinear corrections are essential for 2D samples whose axial extents are usually smaller than the imaging wavelength [29]. However, with saturation the enhanced Beer's law (Eq. (2.15)) can be used to determine the column density $\tilde{n}(x, z)$ as in the 3D case with low optical density. But the lattice depth needs to be sufficiently deep as additional heating mechanisms due to the imaging light lead to a higher equilibrium temperature during the imaging sequence.

However, to determine the resolution R of a diffraction limited imaging system usually the Rayleigh criterion $R = {}^{0.61\lambda}/_{NA}$ is applied, whereas practically the resolution is typically limited by optical aberrations. Therefore a model for the exit pupil function $p(r, \theta)$ of the optical system is introduced. The exit pupil is a concept to simplify some properties of a complex imaging system, where several openings, also called apertures, limit the amount of light to pass, e.g. a lens with finite diameter, or in the description of ray optics, it determines the angle of the ray bundles allowed to pass. The most dominant or limiting aperture is then called the aperture stop, although it need not be physically the smallest opening due to image magnifications, etcetera. An image of this aperture stop is then called exit pupil, thus the exit pupil is the mapping of the aperture stop at the imaging plane and can be modelled as [29]

$$p(\varrho, \theta) = U\left(\frac{\varrho}{a}, \theta\right) \exp\left[i\Theta\left(\frac{\varrho}{a}, \theta\right)\right], \tag{2.21}$$

with the polar coordinates ϱ, θ on the exit pupil, the transmittance function $U(\tilde{\varrho}, \theta)$, the limiting aperture stated as the radius a of the exit pupil, and the wavefront aberration function $\Theta(\tilde{\varrho}, \theta)$. The transmittance function U can be empirically described by [29]

$$U(\tilde{\varrho}) = H(1 - \tilde{\varrho}) \exp\left(-\frac{\tilde{\varrho}}{b}\right), \tag{2.22}$$

while $H(x)$ represents the Heaviside step function to describe the sharp cut off due to the aperture stop and $\exp\left(-\tilde{\varrho}/b\right)$ accounts for the effect that at larger incident angles, or in other words farther away from the optical axis at the axial position of the exit pupil, the transmittance gets smaller with a characteristic parameter b because of the limited angular aperture of optical elements[7]. Additionally, the Heaviside step function leads to the occurrence of the well-known Airy pattern at the image plane due to diffraction, assuming a point-like object and an aberration-free imaging system, except for a finite aperture. The radius of the Airy disk can then be used to define the smallest distance of two points which are still distinguishable. Therefore the Airy disk on the image plane can be projected on the object plane and be related to the NA, finally yielding the Rayleigh criterion for minimal distances in the object plane. Thus the following approximation of the wavefront aberration function can be used, if the optics are of high quality, otherwise more terms need to be included [29]

$$\Theta(\tilde{\varrho},\theta) \approx S_0\rho^4 + \alpha\rho^2\cos[2(\theta-\phi)] + \beta\rho^2, \tag{2.23}$$

with the spherical aberration described by S_0, the astigmatism α, the azimuthal angle ϕ, and the parameter β describing the defocus aberration occurring during an imaging sequence when the atoms are moving out of the focal plane.

Further absorption imaging of a 2D gas with an imperfect imaging system is considered. From scattering theory one knows that in the far-field limit the resulting field of an incident plane wave interacting with a single point object can be decomposed into a spherical and again a plane wave describing the scattered and unscattered field. By considering a coherent source with constant phase and amplitude E_0 the scattered and incident field interferes with each other at the imaging plane. Therefore the spherical wave needs to pass the imaging system and is altered by it corresponding to the Fourier transform of the exit pupil function $p(\mathbf{k})$ at the image plane [34]. With many atoms located at individual positions $\mathbf{r}_j$ in the object plane and total number density $n_\delta(\mathbf{r}) = \sum_j \delta(\mathbf{r}-\mathbf{r}_j)$, the scattered field in total at the image plane can be composed of the individual contributions with each amplitude $\varepsilon \propto E_0 \mathrm{e}^{i\varphi}$ from Eq. (2.6). Due to the superposition principle of electric fields, as linearity is assumed, the total field yields

$$\Delta E(\mathbf{k}) = \sum_j \varepsilon p(\mathbf{k}-\mathbf{k}_j), \tag{2.24}$$

whereas $\mathbf{k}$ and $\mathbf{r}$, corresponding to the image and object plane, are related via $\mathbf{r} = \mathbf{k}\cdot ad$, with aperture a from above and $d = \lambda/(2\pi NA)$ [35]. With the decomposition of scattered and unscattered field Eq. (2.6) can be rewritten to achieve an approximation for the transmission $t_{\mathrm{tr}}^2 = I/I_0 = |E_0+\Delta E|^2/|E_0|^2 = |1+\Delta E/E_0|^2 \approx 1 + 2\Re(\Delta E/E_0)$ for small $|\Delta E/E_0|^2 \ll 1$ and real part function $\Re(c)$, $c \in \mathbb{C}$. Together with the enhanced Beer's law from Eq. (2.15), but on resonance: $\tilde{n} \propto -\ln(t_{\mathrm{tr}}^2) + (1-t_{\mathrm{tr}}^2) I_0/I_{\mathrm{sat}}$, [8], the atomic column density can be approximated by

$$\tilde{n} \approx \tilde{n}_{\mathrm{exp}} \propto -2(1+I_0/I_{\mathrm{sat}})\cdot\Re(\Delta E/E_0) \propto \sum_j \Re[\mathrm{e}^{i\varphi}p(\mathbf{k}-\mathbf{k}_j)], \tag{2.25}$$

[7] Especially relevant if optical coatings are in use, which is usually the case.

[8] Mind the sign due to the inverse function argument of the logarithm.

for small $|{}^{\Delta E}/_{E_0}|^2 \ll 1$ and $[\Re({}^{\Delta E}/_{E_0})]^2 \ll 1$ in order to approximate the logarithm $\ln(1+\epsilon) \approx \epsilon$, for $\epsilon \ll 1$ and $\Re({}^{\Delta E}/_{E_0}) \approx \Re(\Delta E) \cdot \Re({}^{1}/_{E_0})$.

Next, the point spread function $PSF(\mathbf{r})$, as another system parameter, for a coherent light source can be introduced as follows [35]

$$PSF(\mathbf{r}) \propto \Re[\mathrm{e}^{i\varphi} p(\mathbf{k})]\Big|_{\mathbf{k}={}^{\mathbf{r}}/_{ad}}, \tag{2.26}$$

including an appropriate normalization $\int PSF(\mathbf{r})\,\mathrm{d}^2 r = 1$. For an incoherent source the PSF is related to $|p(\mathbf{k})|^2$ since then the superposition principle holds for light intensities, in contrast to the electric field as above. Further the modulation transfer function $\mathcal{M}(\mathbf{k}) = |PSF(\mathbf{k})|$ and image response function $\mathcal{M}^2(\mathbf{k}) = |PSF(\mathbf{k})|^2$ can be defined [35]. For a full analysis of the PSF including Nijboer-Zernike diffraction the appendix of [35] and [36] is highly recommended.

Now a camera with finite sized pixels is considered, whereby the magnification is chosen such that the pixel size projected to the object plane is smaller than the imaging resolution. Then the PSF can be seen constant over a single pixel and the atom number density $n_{\mathrm{exp}}(\mathbf{r}_j)$ recorded at the pixel position $\mathbf{r}_j$ in the object plane can be written as [29]

$$\tilde{n}_{\mathrm{exp}}(\mathbf{r}_j) \equiv \frac{N_j}{A_{\mathrm{px}}} \approx \int n(\mathbf{r}) PSF(\mathbf{r}_j - \mathbf{r})\,\mathrm{d}^2 r, \tag{2.27}$$

with the pixel area A_{px}, the atom number N_j at pixel j, and the atom density $n(\mathbf{r})$ of a 2D sample. Next, the connection to the measurable atom density fluctuation $\delta n(\mathbf{r}) = n(\mathbf{r}) - \langle n(\mathbf{r})\rangle$, with mean value $\langle n(\mathbf{r})\rangle$, can be made via [29]

$$\langle |\delta n_{\mathrm{exp}}(\mathbf{k}_l)|^2\rangle \approx \langle |\delta n(\mathbf{k}_l)|^2\rangle\, \mathcal{M}^2(\mathbf{k}_l), \tag{2.28}$$

utilizing the discrete Fourier transform for a function $f(r)$: $F_l = \sum_j f_j \mathrm{e}^{-ik_l r_j}$ as an approximation for small spatial frequencies $\mathbf{k}_l = \frac{2\pi}{L}(l_x, l_z)$ compared to the inverse pixel size $\sqrt{A_{\mathrm{px}}^{-1}}$, with image length L and index l. Finally the real atomic density fluctuation in k-space can be expressed with the so-called static structure factor [29]

$$S(\mathbf{k}) = \frac{\langle |\delta n(\mathbf{k})|^2\rangle}{N}. \tag{2.29}$$

A concept to describe the scattering behaviour of a sample, with the total atom number N, e.g. $S(\mathbf{k}) = 1$ holds for an uncorrelated sample, i.e. a thermal non-interacting gas, where shot noise is the dominant noise source and thereby responsible for the density variations from shot to shot. Thus recording in situ images of an uncorrelated sample can be used to obtain the density fluctuations of the actual atomic sample and subsequently to characterise the imaging system. Therefore the model for the exit pupil function defined above is used to apply a fitting routine to determine the modulation transfer function of the optical system. From that the static structure factor of a sample with correlated fluctuations can be determined to characterise the new sample in turn,

including all imaging aberration which are included by the defined model function of the exit pupil function, as in Eq. (2.21).

Finally, to describe the thermodynamics of a given system the equations of state (EOS) are used. If the sample is in thermal equilibrium: $\nabla\mu(\mathbf{r}) + \nabla V(\mathbf{r}) = 0$ and the external potential $V(\mathbf{r})$ is varying slowly at position $\mathbf{r}$, the local-density approximation (LDA) can be applied. Therefore the system is assumed to behave locally the same way as a well chosen uniform system, i.e. it can be divided into many subsystems. This can be exploited with in situ imaging, where the density $n(\mathbf{r}, T)$ of a system in equilibrium with temperature T is recorded at all positions $\mathbf{r}$ with potential $V(\mathbf{r})$ and it is then possible to directly extract the EOS $n(\mu, T)$ assuming LDA with $\mu(\mathbf{r}) = \mu_0 - V(\mathbf{r})$. Although μ_0 and T need to be determined separately, e.g. if the atom cloud has residual thermal components it can be obtained from fitting routines applied to that part, whereas the zero point of the trap potential is defined as the trap center, accordingly the chemical potential $\mu_0 = \mu(\mathbf{r} = 0)|_{V(\mathbf{r}=0)\equiv 0}$ [29].

Concluding, if the experimentally challenging requirements for in situ imaging can be fulfilled, in situ imaging is a powerful technique to probe an atomic quantum gas.

2.1.2 Fluorescence Imaging

Absorption and fluorescence imaging are very similar techniques, as they both rely on the absorptive effect of the atoms on a light field. But the latter one evaluates the re-emitted photons and not the missing ones. Therefore the camera axis needs to be off the beam propagation axis of the excitation laser, schematically shown in Fig. 2.3. Otherwise unscattered light can enter the camera and distort the evaluation. The atom cloud is further assumed to behave as a point emitter at the focal position of the imaging lens, which is approximately the case if the focal length is much longer than the diameter of the cloud. Then with no magnetic field present the fluorescence light is isotropically distributed over a 4π solid angle and the imaging system collects the fractional amount[9] $\frac{1}{2}[1 - \cos(\theta_0)]$, with its acceptance half-angle θ_0. Therefore a dilute sample, regarding re-absorption effects, is more crucial as compared to absorption imaging because on the one hand there the acceptance angle can be made small to minimize the already small fractional amount of fluorescence light and on the other hand with a not dilute sample fluorescence light emitted at different positions of the cloud has a different probability to reach the camera without being re-absorbed, wherefore the outcome can be distort significantly for fluorescence imaging. However, with a nonzero static magnetic field the dipole moments of the atoms are aligned corresponding to the external field and the radiation is not isotropic anymore. Corresponding to dipole radiation in the far-field, the lowest intensity of the light emission can be recorded with the dipole moments aligned to the imaging axis and the highest intensity with an orthogonal alignment. Therefore the external magnetic field is usually aligned perpendicular to the camera axis

[9] Obtained by dividing the solid angle of a cone, $\int_0^{2\pi}\int_0^{\theta_0}\sin(\vartheta)\,\mathrm{d}\vartheta\,\mathrm{d}\varphi$, by the total surface area of the unit sphere, $\int_0^{2\pi}\int_0^{\pi}\sin(\vartheta)\,\mathrm{d}\vartheta\,\mathrm{d}\varphi = 4\pi$.

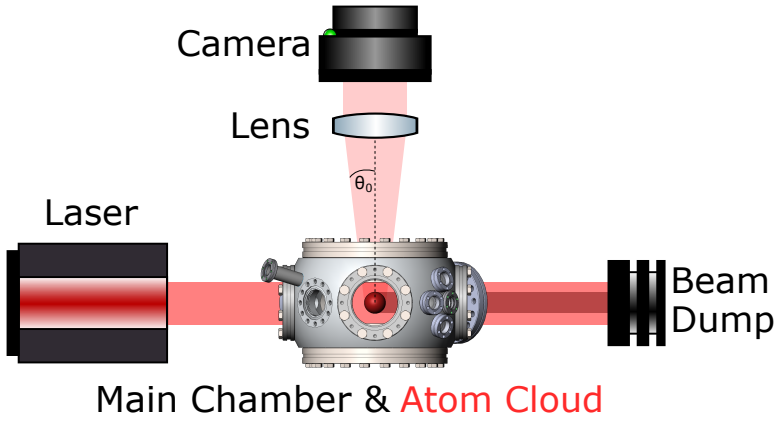

Figure 2.3: Schematic illustration of the fluorescence imaging method. All optical elements crucial for beam shaping and the camera objective are omitted for simplicity, except for the first converging lens nearest to the atoms. It determines the acceptance half-angle θ_0 and thereby the fractional amount of the fluorescence light that can be collected by the imaging system. Therefore the atom cloud is illuminated by a resonant laser source, but now the camera needs to be installed off-axis by at least θ_0 in order to avoid unscattered photons to hit the camera. In principle the actual camera angle is not important because if the magnetic field is zero, the fluorescence light is isotropically distributed. But the camera signal depends on a few external parameters, e.g. the detector efficiency η and the angle θ_0, elaborating the calibration a lot compared to absorption imaging, with respect to the determination of the column density $\tilde{n}$.

for fluorescence imaging to maximize the recorded radiation. As opposed to absorption imaging, where fluorescence light, emitted along the imaging axis, is unwanted and slightly distorts the outcome, but it can then be suppressed greatly by means of an external magnetic field aligned along the imaging axis.

Clearly, the signal strength overall is much weaker, but on one side the camera signal can in principle be enhanced by simply increasing the detection time, although the system must not change significantly over time then. On the other side extraction of a low intensity signal is usually in favour compared to the determination of a small difference in high intensity images. Also the background signal is mostly just limited by the camera dark noise and not additionally by fluctuations of the laser intensities between two corresponding pictures, with and without atoms. Whereas with fluorescence imaging any residual intensity noise is integrated over the whole imaging time. But the signal calibration is more difficult since the excitation beam is attenuated while travelling through the atomic cloud and depends on the local atomic density $n(x, y, z)$, especially along the camera axis y, thereby the local light intensity $I_{\text{local}}(x, y, z)$ needs to be used

instead. Then the camera signal $W(x, z)$ is given by [37]

$$W(x,z) = \frac{1-\cos(\theta_0)}{2}\eta \int_0^{t_0} \int n(x,y,z)\frac{\Gamma}{2}\frac{I_{\mathrm{local}}(x,y,z)}{I_{\mathrm{sat}} + I_{\mathrm{local}}(x,y,z)}\,\mathrm{d}y\,\mathrm{d}t, \tag{2.30}$$

with the detector efficiency η and the imaging time t_0, whereas Γ and I_{sat} are the same as for absorption imaging, assuming a dilute cloud and a resonant probe beam. Whereas the density of the atom cloud and the intensity of the probe beam are considered to be time-independent during imaging, accordingly the signal is directly proportional to t_0 [37]. Thus, the accuracy of the recorded signal is furthermore dependent on the accurate determination of a few external parameters, e.g. η, θ_0, t_0, and the intensity distribution of the excitation beam, whereas the imaging time t_0 can be considered to be the easiest one. The detector efficiency η incorporates, among other things, the quantum efficiency of the camera and the transmission coefficients of the optical elements in the imaging path, especially the vacuum windows, which can be significantly angle- and polarization-dependent, although these windows are specifically coated. Also the determination of the spatial intensity distribution of the probe light can be challenging, as it would be in principle necessary to ascertain it at the position of the atoms inside the vacuum chamber, which cannot be done for obvious reasons. Thus some assumptions need to be made here too.

In the case of absorption imaging these external parameters θ_0, η, and t_0 conveniently drop out of the equation if the corresponding pictures are recorded with the same apparatus and imaging time, what for the former can be assumed to be true and the error of time measurements can be made negligibly small.

2.1.3 Time-of-Flight (TOF) Expansion

To obtain high-contrast absorption images the optical depth $\tilde{\tau}$ of the sample should be near unity [4]. But in typical atom traps this condition is not met and it is necessary to reduce the density, e.g. by free-flight expansion. Therefore the trapping potentials are switched off quickly and the cloud expands for a variable amount of time t, typically a few microseconds. Additionally, as the cloud size increases too, it can be easier to detect small features of the sample, e.g. vortices in a Bose-Einstein condensate (BEC). But one has to keep in mind that the in-trap density evolves differently for different types of particles, atom interactions, and trap geometries [38].

However, if interactions are negligible the TOF expansion behaves as a Fourier transformation between real- and momentum-space, revealing the momentum distribution of the cloud, as the non-interacting atoms expand ballistically in space. Together with the atom statistic and the trap geometry the temperature of the sample can be derived subsequently. At first, it is assumed that the sample is at thermal equilibrium before being released from the trap, which is just possible if the atoms are allowed to interact with each other, but during expansion the interaction should be negligible. Therefore it is necessary to control the atom-atom-interaction during the experiment and this can

be done by utilizing a so-called (magnetic) Feshbach resonance [39]. It occurs when the energy of two colliding atoms coincide with the energy of a quasi-bound molecular state. An external magnetic field can then be used to tune the energy levels relative to each other, thereby it is necessary that the involving states have different magnetic moments, otherwise there would be no relative change in energy possible with an external magnetic field.

Next, the evolution of the atom density during TOF needs to be known in order to choose an appropriate fitting curve applicable to the recorded optical depth, e.g. via absorption imaging, after TOF. But the in-trap density prior TOF needs to be defined beforehand. For an ideal non-interacting Fermi gas the average occupancy of the single particle state i, with energy E_i, is given by the Fermi-Dirac distribution function

$$f_{\mathrm{FD}}(E_i) = \frac{1}{\exp\left(\frac{E_i-\mu}{k_{\mathrm{B}}T}\right)+1}, \tag{2.31}$$

with the Boltzmann constant k_{B}, the absolute temperature T and the chemical potential μ. In a three-dimensional (3D) harmonic trap some energy states are degenerate, therefore it is necessary to introduce a function for the density of states [40]

$$g(E) = \frac{E^2}{2(\hbar\bar{\omega})^3}, \tag{2.32}$$

with the trap frequencies $\omega_x\omega_y\omega_z = \bar{\omega}^3$. It reveals the amount of states within the energy interval $(E, E+\mathrm{d}E)$ and is valid in the continuum limit for a large amount of states [40]. The total number of trapped fermions N can then be obtained by integrating over the total energy and in the low temperature limit ($T \to 0$) the highest occupied energy is denoted by the Fermi energy E_{F}, leading to

$$N = \int_0^\infty f_{\mathrm{FD}}(E)g(E)\,\mathrm{d}E\Big|_{T\to 0} = \int_0^{E_{\mathrm{F}}} f_{\mathrm{FD}}(E)g(E)\,\mathrm{d}E = \frac{1}{6}\left(\frac{E_{\mathrm{F}}}{\hbar\bar{\omega}}\right)^3. \tag{2.33}$$

Subsequently the Fermi temperature can be denoted by

$$T_{\mathrm{F}} = \frac{E_{\mathrm{F}}}{k_{\mathrm{B}}} = \frac{\hbar\bar{\omega}}{k_{\mathrm{B}}}(6N)^{\frac{1}{3}}. \tag{2.34}$$

In phase-space with position and momentum $(\mathbf{r}, \mathbf{p})$ the Fermi-Dirac distribution function, in the Thomas-Fermi approximation, can be written as

$$f_{\mathrm{FD}}(\mathbf{r}, \mathbf{p}) = \frac{1}{\exp\left(\frac{\mathbf{p}^2/2m+V(\mathbf{r})-\mu}{k_{\mathrm{B}}T}\right)+1} \tag{2.35}$$

in the semi-classical approach, where $V(\mathbf{r})$ denotes the potential energy and m the particle mass. The density $n_{\mathrm{F}}(\mathbf{r})$ can then be determined via integration over momentum-space and adding of a normalization factor [27]

$$n_{\mathrm{F}}(\mathbf{r}) = \frac{1}{(2\pi\hbar)^3}\int f_{\mathrm{FD}}(\mathbf{r}, \mathbf{p})\,\mathrm{d}\mathbf{p} = -\frac{1}{\lambda_{\mathrm{dB}}^3}\mathrm{Li}_{3/2}\left[-\exp\left(\frac{\mu - V(\mathbf{r})}{k_{\mathrm{B}}T}\right)\right], \tag{2.36}$$

with the thermal de Broglie wavelength $\lambda_{\mathrm{dB}} = {}^{h}/\sqrt{2\pi m k_{\mathrm{B}} T}$ and the polylogarithm function $\mathrm{Li}_s(y) = \sum_{k=1}^{\infty} ({}^{y^k}/_{k^s})$.

Considering a cylindrically symmetric cloud under TOF, with expansion time t. Then the integrated density $\tilde{n}_{\mathrm{F}}^{\mathrm{TOF}}(x,z,t) = \int n_{\mathrm{F}}^{\mathrm{TOF}}(\mathbf{r},t)\,\mathrm{d}y$ can be determined by applying a rescaling parameter $\gamma_j(t) = \sqrt{1+(\omega_j t)^2}$ to the spatial coordinates $\tilde{x}_j(t) = {}^{x_j}/_{\gamma_j(t)}$ and by considering the equivalent problem, with spatial coordinates $j \in \{x,y,z\}$, thus [38, 41]

$$\tilde{n}_{\mathrm{F}}^{\mathrm{TOF}}(x,z,t) = \\ -\frac{1}{\gamma_x(t)\gamma_z(t)}\frac{m(k_{\mathrm{B}}T)^2}{2\pi\hbar^3\omega_x}\mathrm{Li}_2\left[-\exp\left(\frac{\mu}{k_{\mathrm{B}}T} - \frac{mx^2\omega_x^2}{2k_{\mathrm{B}}T\gamma_x(t)} - \frac{mz^2\omega_z^2}{2k_{\mathrm{B}}T\gamma_z(t)}\right)\right]. \quad (2.37)$$

But the cloud expansion becomes isotropic at large TOF times ($\omega_j t \gg 1$), leading to

$$\tilde{n}_{\mathrm{F}}^{\mathrm{TOF}}(x,z,t) \propto -\frac{1}{t^2}\mathrm{Li}_2\left[-\exp\left(\frac{\mu}{k_{\mathrm{B}}T} - \frac{m(x^2+z^2)}{2k_{\mathrm{B}}Tt^2}\right)\right], \quad (2.38)$$

without dependence of the polylogarithm function on the trap frequencies. Hence, the temperature can be extracted from the width of the cloud via a polylogarithm fit onto the optical depth with known scattering cross section, expansion time, and the particle mass.

In the high temperature limit ($T \gg T_{\mathrm{F}}$) the cloud density from Eq. (2.36) becomes Gaussian as expected for an ideal thermal gas and the same considerations as above in the long time limit lead to [38]

$$\tilde{n}_{\mathrm{th}}^{\mathrm{TOF}}(x,z,t) \propto -\frac{1}{t^2}\exp\left(-\frac{m(x^2+z^2)}{2k_{\mathrm{B}}Tt^2}\right). \quad (2.39)$$

Therefore the temperature can also be obtained separately from a Gaussian fit to the thermal part of the sample, if it is in thermal equilibrium. Wherefore the TOF method is a powerful tool for probing ultracold atoms.

Although imaging by preceding TOF expansion is a destructive method, the resonant excitation beam required for an absorptive imaging method introduces heat to the atomic sample anyway and would influence the atomic sample in-trap. Therefore, while imaging the fluorescence light, one can either continuously drive a cooling transition and keep the atomic sample trapped, e.g. in an optical lattice, or reduce the strength of the absorptive atom-light interaction, e.g. by detuning the probe light off-resonant. Properties of the cloud can then be extracted via dispersive effects. Considering Eq. (2.9) together with the cross section in the low intensity limit in Eq. (2.3) reveals a inverse proportionality

$$\varphi \propto \frac{1}{\Delta} \quad (2.40)$$

of the detuning Δ in the far off-resonance limit ($\Delta \gg {}^{\Gamma}/_{2}$). By contrast with the inverse quadratic proportionality

$$\tilde{\tau} \propto \frac{1}{\Delta^2} \quad (2.41)$$

of the optical depth $\tilde{\tau}$ from Eq. (2.10). In other words, the dispersive effects dominate in the far off-resonance limit and heating due to the absorption of imaging light is negligible, therefore often considered as non-destructive imaging technique.

2.1.4 Dispersive Imaging

Dispersive imaging methods are often used to image atom clouds in situ, when high optical densities or significant heating effects forbid the use of absorptive imaging techniques. The properties of the cloud can then be extracted from the phase of the light field, but a conversion into intensity variations is thereby necessary, which can be detected by a camera subsequently. There are several different techniques very common in the field of atom microscopy, but I just want to mention the dark-field imaging as well as the phase-contrast method based on reference [4], as the former is conceptually one of the simplest dispersive methods.

It is well known that an object at one focal plane of a lens exhibits its Fourier transform at the other focal plane [42]. With that it is possible to separate scattered from unscattered light with spatial filtering at the Fourier plane. For example a tiny opaque object blocks the unscattered light whereas the scattered light is just negligibly attenuated leading to an image without a bright background, schematically shown in Fig. 2.4. As introduced in Eq. (2.6) the electric field E after interaction with the atoms is given

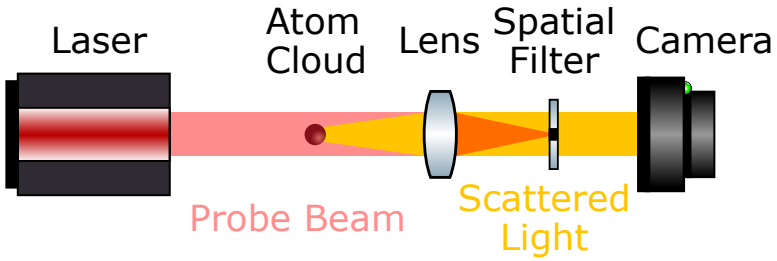

Figure 2.4: Schematic illustration of the dark-field imaging method. All optical elements crucial for beam shaping and the camera objective are omitted for simplicity, except for the first converging lens nearest to the atoms. The atom cloud is illuminated by a coherent light source and scatters part of the light. The unscattered light is blocked by an opaque filter at the Fourier plane of a lens and just the scattered light hits the camera. This leads to a conversion of phase shifts into intensity variations, only which can be recorded by a camera. Especially for transparent phase objects, e.g. an atom cloud with an off-resonant probe beam, this technique is in principle superior compared to solely absorptive approaches.

by

$$E = E_0 t_{\mathrm{tr}}\, \mathrm{e}^{i\varphi} = E_0 + \Delta E \tag{2.42}$$

and can be decomposed into ΔE and E_0, the scattered and unscattered (incident) field, respectively. The recorded dark-field intensity signal I_{df} is then given by the square of

the absolute value of the difference ΔE:

$$I_{\mathrm{df}} = |E - E_0|^2 = I_0 \left[1 + t_{\mathrm{tr}}^2 - 2t_{\mathrm{tr}} \cos(\varphi)\right]. \tag{2.43}$$

It is clearly visible that it is not only just filtering the bright background intensity, but also converting phase informations into intensity variations, wherefore it is a dispersive imaging technique. By considering small phase shifts φ, Eq. (2.43) simplifies to

$$I_{\mathrm{df}}\Big|_{\varphi\to 0} \approx I_0 \left[(1 - t_{\mathrm{tr}})^2 + t_{\mathrm{tr}}\varphi^2\right]\Big|_{t_{\mathrm{tr}}\to 1} \propto \varphi^2, \tag{2.44}$$

making this technique better suited for objects with high transparency, or in other words far off-resonant to an atomic transition, compared to absorption imaging. By determination of the phase shift the column density $\tilde{n}$ can then be extracted by utilizing Eq. (2.9).

In the case of phase-contrast imaging the unscattered light at the Fourier plane is not blocked, but phase shifted by $\pm\,\pi/2$ with a phase plate leading to interference between scattered and unscattered light at the imaging plane. The intensity signal is given by [4]

$$I_{\mathrm{pc}} = \left|\Delta E + E_0 \mathrm{e}^{\pm i\pi/2}\right|^2 = \left|E_0 t_{\mathrm{tr}} \mathrm{e}^{i\varphi} - E_0 + E_0 \mathrm{e}^{\pm i\pi/2}\right|^2 = I_0 \left[2 + t_{\mathrm{tr}}^2 - 2\sqrt{2}\, t_{\mathrm{tr}} \cos\left(\varphi \pm \frac{\pi}{4}\right)\right] \tag{2.45}$$

and can be simplified for small phase shifts to

$$I_{\mathrm{pc}}\Big|_{\varphi\to 0} \approx I_0 \left[1 + (1 - t_{\mathrm{tr}})^2 \pm 2t_{\mathrm{tr}}\varphi\right], \tag{2.46}$$

revealing a linear relation in φ, in contrast to a quadratic relation in the case of dark-field imaging. Accordingly phase-contrast imaging leads to a better SNR compared to dark-field imaging for small phase shifts. Nevertheless choosing, fabricating, and aligning the appropriate phase plate can be very challenging in the experiment since the effect on the scattered light should be negligible while the unscattered light is affected and therefore phase-contrast is not automatically favoured over dark-field imaging [43, 44].

2.2 Simplified Absorption Imaging Procedure for a DyK Mixture

First it needs to be distinguish between horizontal and vertical imaging. Where for the former resonant absorption imaging with one sCMOS camera[10] for both species and for the second fluorescence imaging with a EMCCD cameras[11] is realized. For beam overlapping dichroic mirrors are used to ensure the same imaging angle for both species.

[10] Andor - NEO 5.5 sCMOS
[11] Andor - iXon Ultra 897 EMCCD

On potassium the broad D2 line with 767 nm and on dysprosium the broad 421 nm line with both having σ^+polarization are used. Now, for absorption imaging as mentioned in Section 2.1.1 two times two plus one picture for the two species plus one for the background are needed. The temporal sequence with some standard time values is:

- time-of-flight (TOF) expansion
- obtaining $I_{\mathrm{out,\,K}}$ for K, with atoms present, accumulated over 10 µs
- variable time delay of at least 0.5 µs
- obtaining $I_{\mathrm{out,\,Dy}}$ for Dy, with atoms present, accumulated over 10 µs
- 40 ms after $I_{\mathrm{out,\,K}}$ is recorded, $I_{\mathrm{in,\,K}}$ is obtained for K, without atoms present, accumulated over 10 µs
- 40 ms after $I_{\mathrm{out,\,Dy}}$is recorded, $I_{\mathrm{in,\,Dy}}$ is obtained for Dy, without atoms present, accumulated over 10 µs
- Finally, the background I_{bg} is recorded with the imaging light switched off.

Then, Eq. (2.11) can be used to determine the corresponding optical depths.

2.3 The Blue Transition of ^{40}K

The term *blue transitions* of potassium refers to the transitions from the $4S_{1/2}$ ground state to the $5P_J$ states with the next higher principal quantum number as the wavelengths are in the deep blue regime around 405 nm. The total angular momentum quantum number is thereby denoted by J and can attain the values $J \in \{1/2, 3/2\}$. The level scheme of ^{40}K is summarized in Fig. 2.5, with a focus on the states $5P_{3/2}$, $4P_{3/2}$, and $4S_{1/2}$. Thereby I am interested in the transition involving the $5P_{3/2}$ excited and $4S_{1/2}$ ground state together with the comparison to the well-known D2 line ($4P_{3/2} \leftrightarrow 4S_{1/2}$) of potassium.

The first and obvious advantage of the blue line is a lower wavelength λ. Consequently the diffraction limit is lower too, due to the direct proportionality with the wavelength. Therefore a higher imaging resolution can be achieved, assuming a diffraction limited microscope objective.

Secondly, it is far off-resonant to the MOT light on the infrared (IR) D2 line, therefore an influence on the blue imaging path due to any stray light can be very well suppressed by optical bandpass filters. Additionally imaging on the blue line would in principle be possible with an still active IR MOT. But one has to keep in mind that the absorption rate on the blue transition is altered while the atoms are cycling the D2 transition, albeit it becomes negligible in the low intensity regime. Also the cloud is influenced as absorption of imaging light induces heat to the sample, which needs to be incorporated when interpreting recordings.

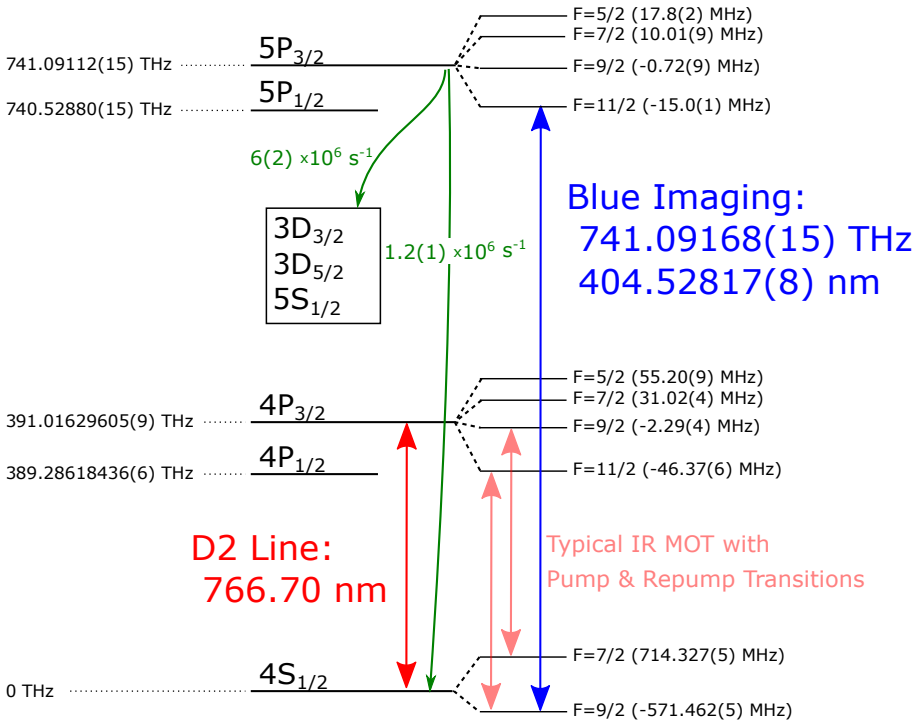

Figure 2.5: Summarized level scheme of ^{40}K with the possible decay modes of the excited state $5P_{3/2}$, indicated by the green arrows. The transition to the $4S_{1/2}$ ground state can either take place directly via emission of a blue photon or via a multi-photon cascade. The corresponding (effective) decay rates are $\Gamma^{\text{eff}}_{\text{multi}} \approx 6(2) \times 10^6\,\text{s}^{-1}$ and $\Gamma_{\text{direct}} \approx 1.16(9) \times 10^6\,\text{s}^{-1}$ respectively [45, 46]. Whereas the multi-photon decays are summarized by a single effective decay rate in order to compare it to the direct blue transition. For clarity the outlined distances are not in scale with the true energy level splittings of each state. Also the hyperfine (HF) splitting of the $5P_{3/2}$ state is much smaller than for the $4P_{3/2}$ state, shortly explained by the larger average electron distance from the nucleus. The big blue arrow denotes the HF-resolved transition used for blue imaging and the light red arrows denote the transitions used for a typical infrared MOT utilizing the D2 line. As repumper the same infrared transition ($F = 7/2 \leftrightarrow F' = 9/2$) is used in both cases. The error on the linewidth of the very precisely known D2 line is omitted for reasons of clearness. (Figure based on [45, 47, 46].)

Thirdly, imaging of ^{161}Dy is already realized on the blue, using the broad 421 nm transition. Accordingly, realizing imaging of ^{40}K on the blue too, would equalize the diffraction limited resolutions more closely and it would make the design process of an imaging objective easier, including the coating effort.

But there are also some drawbacks which need to be mentioned. Therefore the properties of the blue transition are more closely compared to the D2 line in Table 2.1. The natural linewidth $\Gamma/2\pi$ of the D2 line is just given by the decay rate to the ground state since it is a closed transition. By contrast the blue transition is not closed and the direct

	$4P_{3/2} \leftrightarrow 4S_{1/2}$	$5P_{3/2} \leftrightarrow 4S_{1/2}$
Wavelength λ	766.7006747(2) nm	404.52847(8) nm
Frequency ν	391.01629605(9) THz	741.09112(15) THz
Linewidth $\Gamma/2\pi$	6.04(1) MHz	1.19(2) MHz
Sat. Intensity I_{sat}	1.752(3) mW cm^{-2}	23(2) mW cm^{-2}
Cross Section	0.2807(7) µm^2	0.010(1) µm^2
Branching Ratio	1 (closed)	$1/6.4(7)$
Steady-State Pol.	100 %	61(1) %
Depumping Prob.	0 %	18(2) %

Table 2.1: Summarized properties of the D2 line and the *blue D2 line* of ^{40}K. The transition energies are determined experimentally [45] and listed in wavelength and frequency units, as well as the linewidths via measurements of the (total) lifetimes of the excited states [45, 48]. The branching ratio states the chance for a direct decay to the ground state vs. a multi-photon cascade and depends on the individual decay rates of the different decay channels. The steady-state polarization represents the amount of atoms being in the lowest Zeeman sublevel ($m_F = +9/2$) of the $|F = 9/2\rangle$ ground state while driving at I_{sat} and the depumping probability indicates the percentage of atoms decaying from the $|F' = 11/2, m_{F'} = +11/2\rangle$ excited state to the dark $|F = 7/2, m_F\rangle$ ground state manifold, raising the necessity of a repumping laser, whereby only electric-dipole transitions are considered. (Based on [46, 37].)

single photon transition $5P_{3/2} \leftrightarrow 4S_{1/2}$ exhibits a decay rate of $\Gamma_{\text{direct}} \approx 2\pi \times 185(14)$ kHz. Nevertheless, other decay channels cause a broadening of the $5P_{3/2}$ excited state leading to a linewidth of $\Gamma_{\text{direct}} + \Gamma^{\text{eff}}_{\text{multi}} = \Gamma_{\text{sum}} \approx 2\pi \times 1.19(2)$ MHz. Whereas the total decay rate was determined by an additional measurement of the total lifetime of the excited state, thus 134(2) ns [48], leading to a more accurate result compared to the combined error of the decay rates shown in Fig. 2.5.

The saturation intensity of the closed D2 transition can be calculated by [25]

$$I_{\text{sat}} = \frac{h\nu^3\Gamma\pi}{3c^2} = \frac{h\Gamma c\pi}{3\lambda^3} \tag{2.47}$$

and the cross section by

$$\sigma_0 = \frac{h\nu\Gamma}{2I_{\text{sat}}}, \tag{2.48}$$

as introduced in Section 2.1. For the open transition the evaluation is much more elaborate, requiring calculations including multi-level OBE. Therefore all relevant $|n, J, F, m_F\rangle$ electronic states need to be included and the corresponding set of linear equations $\dot{\mathbf{y}} = \mathbf{A}\mathbf{y}$ need to be solved for $\mathbf{y}(t)$ via diagonalisation of the matrix $\mathbf{A}$, whereas the total system is approximated by effective two-level systems. The steady-state solution ρ^{ss}_{ee} for the desired excited state is obtained by letting $t \to \infty$, then the excitation properties can be calculated similar to a standard TLS, for details consider the appendix of [37]. But it is necessary to include a repump beam into this calculations, otherwise the total population would be transferred into the dark $|F = 7/2, m_F\rangle$ ground state manifold for $t \to \infty$.

The repumper drives the transition $|4S_{1/2}, F = 7/2\rangle \leftrightarrow |4P_{3/2}, F' = 9/2\rangle$, as indicated in Fig. 2.5 and is assumed to be strong enough to be not the limiting factor [46].

Now comparing the two transitions in Table 2.1 reveals at first an absorption cross section for the blue transition which is 28 times smaller, therefore the atom-light interaction is that much weaker. For imaging purposes it implies the need of a higher exposure time in order to achieve the same signal strength, as the optical depth is smaller too. But this can also be advantageous because the atoms are less disturbed and the sample can have a higher density without the risk of too many re-absorption processes. For in situ imaging this is especially important since the atom density cannot be reduced by free-flight expansion. Additionally by varying the strength of the repumping laser the atoms can be partially pumped into the dark $|F = 7/2, m_F\rangle$ ground state and as a result the effective optical density can be reduced in a controlled way.

For fluorescence imaging the branching ratio is of peculiar interest because it states the probability of a direct single photon decay versus a multi-photon decay process. The latter of which cannot be detected by the imaging system leading to a weaker fluorescence signal. In average only every sixth decay is carried out by emitting a single blue photon, but it can in principle be compensated by a longer camera exposure time. Additionally, the available multi-photon decay channels give rise to the depumping probability, so that the transition is not closed and 18(2) % of the atoms decay to the $|F = 7/2, m_F\rangle$ ground state manifold. Also the spin polarization of the atoms is not preserved as only 61(1) % of them remain in the lowest Zeeman sublevel ($m_F = +9/2$) of the $|F = 9/2, m_F\rangle$ ground state manifold while driving the transition a I_{sat}.

3 Building a Blue Laser

That light influences macroscopic objects were known well before Maxwell's theory of electromagnetism, but it allowed a clear description of the observed phenomenons. At that time high intensity lamps were utilized to demonstrate radiative effects on micro- and macroscopic objects. Nevertheless, the invention of the laser made light assisted atom manipulations concrete and precisely controllable. The potential of laser light was soon recognized and has meanwhile become indispensable in every modern experiment involving manipulations of atoms, ions, or composites of them [49]. There exists countless different schemes and techniques to obtain laser light on a vast range of wavelengths and power [42, 50].

In this chapter I want to cover some possibilities for building a coherent blue light source, but first the requirements on the source need to be determined. In this case an atomic transition will be addressed, wherefore the properties described in Section 2.3 are relevant, especially the wavelength $\lambda \approx 404.5\,\mathrm{nm}$ and the natural linewidth $\Gamma \approx 2\pi \times 1.2\,\mathrm{MHz}$. For absorption and fluorescence imaging the laser linewidth needs to be at least as small as the transition linewidth in order to still meet the resonance condition. But first some fundamental properties of lasing are summarized as entry point of the topic. Followed by the description of two schemes for a diode laser system.

3.1 Fundamental Prerequisites of Lasing

The word *laser* itself is an acronym and stands for light amplification by stimulated emission of radiation. This already reveals the underlying key principle of lasing, stimulated emission, as it is a coherent mechanism to amplify light. But a laser is not just an optical amplifier it is a complete oscillator, i.e. it consists of an amplifying part together with a positive feedback loop. Referring to electronic oscillators, stable oscillation can build up if the overall gain of the system is greater than the overall loss and if the phase shift of a single round trip is a multiple of 2π. Then the signal is amplified on each round trip until the amplifier necessarily saturates, the gain reduces subsequently and a steady-state is reached when the reduced gain equals the loss.

Usually the principal parts of a laser system are categorized by three components:

- The **gain** or **active medium** behaving as an optical amplifier, with the underlying process of stimulated emission,
- the **pump source** providing external energy to the amplifier, which mainly utilizes an electrical or optical pumping mechanism,

- and the **resonator** as positive feedback loop, which can be an optical or electrical feedback, or both, e.g. an optical cavity consisting of two mirrors.

For a simple description it is sufficient to describe the active medium as an ensemble of atoms approximated as TLS with a ground $|1\rangle$ and excited state $|2\rangle$ separated by the energy $E = h\nu_{12} = \hbar\omega_{12}$ as well as the level populations[1] N_1 and N_2, respectively. Phenomenologically three mechanisms are possible for an atom to interact with a light field of spectral energy density[2] $\rho(\omega)$ and frequency $\omega \simeq \omega_{12}$ in close proximity to the atomic resonance:

- **Absorption**: If an atom is in the stable ground state $|1\rangle$ it can absorb a photon with energy $\hbar\omega$ and undergo a transition to the upper state $|2\rangle$. The probability for that process is proportional to the absorption cross section $\sigma_{12}(\omega)$ and the photon flux density[3] $F = {}^{I}/_{\hbar\omega}$, with the light intensity I. The rate of absorption events is then given by
$$\left.\frac{\mathrm{d}N_2}{\mathrm{d}t}\right|_{\text{absorp.}} = N_1\sigma_{12}F = N_1B_{12}\rho, \tag{3.1}$$
which can also be expressed with the well-known Einstein coefficient for absorption B_{12}.

- **Stimulated emission**: An atom, initially in the excited state $|2\rangle$, can be stimulated by an incident light wave, with frequency ω, to emit a photon with the same frequency ω, phase, polarization, and direction of the ingoing radiation. The rate of this coherent process can be described by
$$\left.\frac{\mathrm{d}N_2}{\mathrm{d}t}\right|_{\text{st.em.}} = -N_2\sigma_{21}F = -N_2B_{21}\rho, \tag{3.2}$$
with the stimulated emission cross section σ_{21} and the Einstein coefficient for stimulated emission B_{21}.

- **Spontaneous emission**: An excited atom can also spontaneously decay via emission of a photon with frequency ω_{12} independently of external fields. As an incoherent process the phase, polarization, and direction of the emitted radiation are randomly distributed. The corresponding rate equation reads as follows
$$\left.\frac{\mathrm{d}N_2}{\mathrm{d}t}\right|_{\text{sp.}} = -\frac{N_2}{\tau_{\text{sp}}} = -N_2A_{21}, \tag{3.3}$$
with the spontaneous emission lifetime τ_{sp} and the Einstein coefficient for spontaneous emission $A_{21} = {}^{1}/_{\tau_{\text{sp}}}$. Additionally, an excited atom can undergo a non-radiative decay process too, e.g. via collisional interactions, which can also be described by an exponential decay with the non-radiative lifetime τ_{nr}, whereby the overall lifetime τ_2 of the state $|2\rangle$ is further given by $\tau_2 = \left(\tau_{\text{sp}}^{-1} + \tau_{\text{nr}}^{-1}\right)^{-1}$.

[1] Strictly speaking it is a population density, i.e. number of atoms per unit volume.
[2] The spectral energy density $\rho(\omega)$ represents energy per unit volume and frequency interval.
[3] The photon flux density F represents the number of photons per second and unit area.

Altogether the rate equation for the upper state population N_2 can be written as [25]

$$\frac{\mathrm{d}N_2}{\mathrm{d}t} = N_1 B_{12}\rho - N_2 B_{21}\rho - N_2 A_{21}, \tag{3.4}$$

whereas the assumption of a TLS constrains

$$\frac{\mathrm{d}N_1}{\mathrm{d}t} = -\frac{\mathrm{d}N_2}{\mathrm{d}t}. \tag{3.5}$$

At thermal equilibrium the rate equation equals zero and the populations N_1^{eq}, N_2^{eq} settle to the value given by the Boltzmann distribution at temperature T

$$\frac{N_2^{\mathrm{eq}}}{N_1^{\mathrm{eq}}} = \frac{g_2}{g_1}\exp\left(-\frac{\hbar\omega}{k_{\mathrm{B}}T}\right), \tag{3.6}$$

with the degeneracies g_1, g_2 of the upper and lower state, which can also just be seen as statistical weight factors and are set equal, $g_1 = g_2$, for convenience.

Now assuming black-body radiation, as the atom is placed inside a cavity resonator at thermal equilibrium, the corresponding spectral energy density can be determined by the Planck distribution law

$$\rho(\omega) = \frac{h\omega^3}{\pi^2 c^3}\frac{1}{\exp\left(\frac{\hbar\omega}{k_{\mathrm{B}}T}\right) - 1}, \tag{3.7}$$

with the mode density $2\omega^2/\pi c^3$ per unit volume and frequency interval. Hence, the three Einstein coefficients can be set into relation by inserting Eqs. (3.6) and (3.7) into Eq. (3.4), thus [25]

$$A_{21} = \frac{h\omega^3}{\pi^2 c^3} B_{21} \tag{3.8}$$

$$B_{12} = B_{21} \quad \Longleftrightarrow \quad \sigma_{12} = \sigma_{21} \equiv \sigma. \tag{3.9}$$

The spontaneous emission lifetime is further given by [50]

$$\tau_{\mathrm{sp}} = \frac{1}{A_{21}} = \frac{3h\varepsilon_0 c^3}{2\omega_{12}^3 n_{\mathrm{ref}} |d_{12}|^2}, \tag{3.10}$$

with the vacuum permittivity ε_0, the vacuum speed of light c, the refractive index n_{ref} of the active medium, and the dipole matrix element $d_{12} = \langle\psi_1|\, e\mathbf{r}\, |\psi_2\rangle$, where e is the elementary electron charge, $\mathbf{r}$ the position operator, and $|\psi_i\rangle$ are the eigenstates of the TLS and therefore $|\psi_1\rangle \mathrel{\widehat{=}} |1\rangle$ and $|\psi_2\rangle \mathrel{\widehat{=}} |2\rangle$, respectively. The transition cross section σ is connected via [42]

$$\sigma(\omega) = \frac{c^2\pi}{2\omega_{12}^2 n_{\mathrm{ref}}^2}\frac{1}{\tau_{\mathrm{sp}}} g_{\mathrm{ls}}(\omega) = \frac{\pi\omega_{12}|d_{12}|^2}{3\varepsilon_0 hcn_{\mathrm{ref}}} g_{\mathrm{ls}}(\omega), \tag{3.11}$$

where g_{ls} is the normalized lineshape function of the atomic transition, which includes broadening effects, e.g. due to spontaneous emission or collisional interactions, and can

be described by a convolution of a Lorentzian and Gaussian function for homogeneous and inhomogeneous broadenings, respectively.

Considering Eq. (3.4), while neglecting spontaneous emission, the change of the photon flux $\mathrm{d}F$ per length $\mathrm{d}z$ of the active medium in z-direction can be written as

$$\frac{\mathrm{d}F}{\mathrm{d}z} = (N_2 - N_1)\sigma F(z) = \gamma_{\mathrm{gain}} F(z), \tag{3.12}$$

with the gain coefficient[4] $\gamma_{\mathrm{gain}} = (N_2 - N_1)\sigma$. Thereby light is coherently amplified if the amount of stimulated emission is greater than the absorptive counterpart, which is fulfilled if a so-called population inversion $N = N_2 - N_1 > 0$ is established. But at thermal equilibrium this is not possible, at least for temperatures around 300 K, since it is Boltzmann distributed then. Therefore a pump source needs to be introduced to drive the system out of equilibrium, but for a TLS, even with an infinitely strong pump, i.e. $\rho \to \infty$, a population inversion in steady-state is not possible, since Eq. (3.4) leads to a maximum value of $N = 0$, thus equal population. Therewith at least three energy levels need to be involved, whereas in practise often a four-level pumping scheme is in use, as shown in Fig. 3.1. But the medium still needs to obey certain criteria to

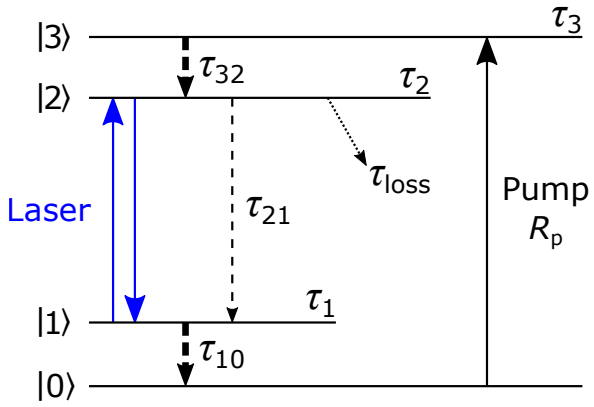

Figure 3.1: Illustration of a pumping scheme for a four-level system. Induced processes are depicted as solid arrows and spontaneous emission as dashed arrow. The lasing transition involves the two states $|2\rangle$ and $|1\rangle$. Now, the pump source transfers atoms form the ground state $|0\rangle$ to the excited state $|3\rangle$ and a subsequent rapid decay to state $|2\rangle$ is necessary to achieve a population inversion on state $|2\rangle$. Also a rapid decay from state $|1\rangle$ to $|0\rangle$ is required to keep the absorption of the lasing transition low. The combined lifetime τ_i covers all decays from the upper state $|i\rangle$ to any lower state, whereas the lifetime τ_{ij} covers all decay mechanisms from state $|i\rangle$ to $|j\rangle$, and τ_{loss} comprises the photons lost from the system, e.g. scattered out of the cavity, or finite cavity mirror reflectivity, or general internal loss mechanisms.

achieve a population inversion. First, the lower state $|1\rangle$ of the lasing transition needs to be drained quickly to the ground state $|0\rangle$, which can be done either by spontaneous

[4]The gain coefficient γ_{gain} represents the increase in number of photons per unit length.

emission or non-radiative decay mechanisms, the combined lifetime for both processes is included in τ_1. Then the pump source strongly pumps the population from state $|0\rangle$ to the uppermost state $|3\rangle$ at a pump rate R_p, which is assumed to be constant, wherefore the ground state $|0\rangle$ needs to be seen as an inexhaustible reservoir. The lifetime τ_{32} again needs to be small to enable a fast decay to the upper lasing state $|2\rangle$, such that an effectively unpopulated state $|3\rangle$ can be assumed. Hence, the rate at which state $|2\rangle$ is populated can be approximated by ${\mathrm{d}N_2}/{\mathrm{d}t}|_\mathrm{pump} \approx R_\mathrm{p}$. Additional decay paths with respect to the upper lasing state are summarized by the combined lifetime τ_2, which needs to be sufficiently long to be able to accumulate significant population in state $|2\rangle$. Thus, the rate equations for the two lasing states can be written as

$$\frac{\mathrm{d}N_2}{\mathrm{d}t} = R_\mathrm{p} - (N_2 - N_1)B_{21}\rho - N_2\frac{1}{\tau_2} \tag{3.13}$$

$$\frac{\mathrm{d}N_1}{\mathrm{d}t} = (N_2 - N_1)B_{21}\rho + N_2\frac{1}{\tau_{21}} - N_1\frac{1}{\tau_1} \tag{3.14}$$

and again, by considering the steady-state solution, ${\mathrm{d}N_1}/{\mathrm{d}t} = {\mathrm{d}N_2}/{\mathrm{d}t} = 0$, the steady-state population difference $N_\mathrm{ss} = N_2 - N_1|_{t\to\infty}$ results in

$$N_\mathrm{ss} = \frac{R_\mathrm{p}\tau_2\left(1 - \frac{\tau_1}{\tau_{21}}\right)}{1 + B_{21}\rho\left[\tau_2 + \tau_1\left(1 - \frac{\tau_2}{\tau_{21}}\right)\right]}. \tag{3.15}$$

To obtain population inversion, $N_\mathrm{ss} > 0$, the lower lasing state $|1\rangle$ has to be drained faster than it is populated by the lasing transition, i.e. at steady-state $\tau_1 < \tau_{21}$. But by including stimulated emission too, the condition $\tau_1^{-1} > \tau_{21}^{-1} + B_{21}\rho$ has to be satisfied instead. Further, by adding Eqs. (3.13) and (3.14) at steady-state, the pump just needs to compensate the population lost from the lasing transition that is $R_\mathrm{p} = N_1\tau_1^{-1} + N_2(\tau_{20}^{-1} + \tau_\mathrm{loss}^{-1})$, since $\tau_2^{-1} = \tau_{20}^{-1} + \tau_{21}^{-1} + \tau_\mathrm{loss}^{-1}$. Although under lasing operation the stimulated part has to be considered too [51].

Next, the active medium is put inside a cavity and a strong population inversion is assumed. While the light field inside the resonator starts to build up by stimulated emission the inversion starts to decrease, implying a reduction of the gain coefficient γ_gain too, known as saturation of the active medium. Once the medium is fully saturated the population inversion has reduced to the threshold value N_th and an equilibrium is reached where the gain equals the total losses. Thus,

$$\mathrm{e}^{2\gamma_\mathrm{gain}d_\mathrm{gain}} \cdot \mathrm{e}^{-2\gamma_\mathrm{loss}d_\mathrm{cav}} = 1 \quad \Leftrightarrow \quad N_\mathrm{th} = \frac{\gamma_\mathrm{loss}}{\sigma}\frac{d_\mathrm{cav}}{d_\mathrm{gain}}, \tag{3.16}$$

with the cavity length d_cav, the length of the active medium d_gain, and the loss coefficient[5]

$$\gamma_\mathrm{loss} = \frac{1}{\tau_2 c} \approx \frac{1}{\tau_\mathrm{loss} c}, \tag{3.17}$$

[5] Analogously, the loss coefficient γ_loss represents the decrease in number of photons per unit length.

where the cavity photon lifetime $(\gamma_{\text{loss}}c)^{-1} \approx \tau_{\text{loss}}$ is usually dominated by the external loss mechanisms as introduced in Fig. 3.1. Clearly, the threshold population inversion N_{th} is independent of the pump rate, but it sets the minimum pump rate R_{p}^{th} necessary for lasing operation. Below threshold, light is exponentially damped inside the cavity, wherefore ρ can be set to zero in Eq. (3.15) and together with the assumption $\tau_1 \ll \tau_{21}$ the threshold pump rate is given by

$$R_{\text{p}}^{\text{th}} \approx \frac{N_{\text{th}}}{\tau_2} \approx \frac{N_{\text{th}}}{\tau_{\text{loss}}}. \tag{3.18}$$

Therefore increasing the pump rate increases the population inversion and above threshold the photon flux starts to increase too, until the population inversion is reduced back to its threshold value. Thus, under lasing operation the population always remains at the threshold value such that the gain equals unity and the oscillation is stable. In other words, by further increasing the pump rate just the light intensity increases, illustrated in Fig. 3.2.

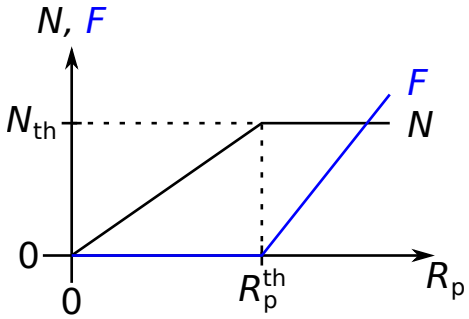

Figure 3.2: The population inversion N and the photon flux F are schematically plot against the pump rate R_{p}. Below threshold the internal photon flux is damped to zero, whereas spontaneous emission is neglected. Above threshold the flux increases proportional to the pump rate, as the population inversion is constrained to its threshold value N_{th} due to the saturation of the gain medium.

The laser output power P_{out} is finally determined by the out-coupling coefficient of the laser cavity, e.g. the transmittance T_{out} of the out-coupling cavity mirror, multiplied by the internal photon flux F and photon energy $\hbar\omega$. But a higher transmittance also reduces the internal photon flux, since the transmittance contributes to the total loss of the cavity. Referring to small-signal considerations, there exists an optimum value $T_{\text{out}}^{\text{max}}$ to maximize the output power [42]

$$T_{\text{out}}^{\text{max}} \approx \sqrt{\Gamma_{\text{gain}}^0 \tilde{\Gamma}_{\text{loss}}} - \tilde{\Gamma}_{\text{loss}}, \tag{3.19}$$

whereas Γ_{gain}^0 represents the small-signal gain and $\tilde{\Gamma}_{\text{loss}}$ comprises the total loss of the cavity except for the out-coupling mirror. For example the small-signal gain of a linear Fabry-Perot cavity can be determined by $\Gamma_{\text{gain}}^0 = 2\gamma_{\text{gain}}^0 d_{\text{gain}}$, since the active medium is passed twice in one round trip, with the small-signal gain coefficient $\gamma_{\text{gain}}^0 = N_{\text{ss}}^0 \sigma$ and the

equilibrium population inversion $N_{\mathrm{ss}}^0 \approx R_{\mathrm{p}}\tau_2$ in absence of amplifier saturation. Again, considering a linear cavity, the total loss $\tilde{\Gamma}_{\mathrm{loss}}$ can be expressed as $\tilde{\Gamma}_{\mathrm{loss}} = 2(\gamma_{\mathrm{loss}} - \gamma_{\mathrm{m1}})d_{\mathrm{cav}}$, with the loss coefficient of the out-coupling mirror $\gamma_{\mathrm{m1}} = -\frac{1}{2d_{\mathrm{cav}}}\ln(1 - T_{\mathrm{out}})$.

However, as simple summary: above threshold the output power can be determined by

$$P_{\mathrm{out}} = \hbar\omega\eta_{\mathrm{s}}(R_{\mathrm{p}} - R_{\mathrm{p}}^{\mathrm{th}})V, \tag{3.20}$$

where V is the volume of the active medium, assuming an uniform pumping of the medium and η_{s} represents the slope efficiency of the laser, i.e. it states the relation between pump power and output power, thus the efficiency of laser radiation. It further involves the pump efficiency, the out-coupling efficiency, the quantum efficiency, etcetera [50].

To obtain a stable oscillator beside the gain condition also the phase condition has to be fulfilled, i.e. a phase shift of a multiple of 2π per round trip is needed to achieve a positive feedback. Therefore the condition $k2d_{\mathrm{cav}} = \mathbb{Z}\cdot 2\pi$ sets the oscillation frequencies supported by the resonator, with the wavenumber $k = {}^{2\pi}/_{\lambda} = {}^{2\pi\nu}/_{c} = {}^{\omega}/_{c}$ and the mirror spacing d_{cav} of a Fabry-Perot resonator, for example. The mode spacing is given by the free spectral range $FSR = {}^{c}/_{2d_{\mathrm{cav}}}$ and the mode linewidth $\Delta\nu_{\mathrm{R}}$ is connected via the Finesse $\mathcal{F}$ of the cavity: $FSR \approx \mathcal{F}\cdot\Delta\nu_{\mathrm{R}}$. The energy density of the light field is then concentrated on a few stable resonator modes with central frequencies ν_i and $i \in \mathbb{Z}$. If the gain coefficient saturates homogeneously only a single resonator mode ν_0 survives, since homogeneous gain saturation reduces the population inversion uniformly and therefore affects all modes equally. In the end only that mode exhibiting the lowest loss still fulfils the lasing condition, while all other modes are exponentially damped to zero, illustrated in Fig. 3.3.

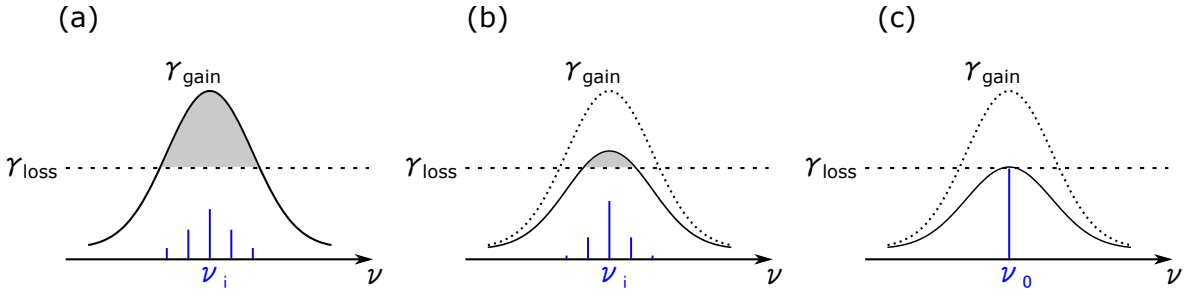

Figure 3.3: In a homogeneously broadened active medium the gain coefficient $\gamma_{\mathrm{gain}}(\nu)$ is reduced uniformly over the frequency range ν, while the light intensity builds up immediately after laser turn-on. Occupied laser modes are depicted as blue delta peaks and regions above threshold are shaded in grey. (a) At the beginning all resonator modes above the lasing threshold, given by the loss coefficient γ_{loss}, are occupied. (b) The effect of gain saturation reduces the gain coefficient, wherefore the outermost modes drop below the threshold and start to vanish. (c) Finally the peak of the gain equals the loss coefficient and only one mode still meets the threshold condition and therefore concentrates the energy density in it.

In an inhomogeneously broadened medium spectral multi-mode (MM) lasing is possible because different resonator modes utilize different spectral regions of the gain coefficient, e.g. they interact with different groups of atoms. Therefore the part of the population inversion of one mode is unaffected by the reduction of another mode, since one mode only reduces a small spectral part of the gain coefficient. This effect is known as *spectral hole burning*, assuming the width of the spectral hole to be smaller than the resonator mode spacing otherwise mode competition would again lead to a suppression of modes [42]. Another effect, called *spatial hole burning*, can also lead to MM lasing. Thereby different modes occupy different spatial regions within the active medium. This can be due to formation of standing waves in a linear resonator or by different available transversal modes of the resonator, which simply have a different spatial distribution and as a consequence the gain saturates inhomogeneously, leaving enough inverted population for other modes to survive.

Nevertheless, to achieve single-mode (SM) operation other longitudinal modes can be suppressed by the use of frequency-selective elements placed inside the resonator. Thereby the loss coefficient is increased at the undesired frequency regions, leading to a dominant mode at the chosen frequency. To suppress other transversal modes, for example an aperture can be added in order to selectively attenuate unwanted spatial modes and maintain transversal SM lasing. Additionally, instabilities and fluctuations of the resonator and the gain material lead to temporal variations of the gain and loss coefficient and further alters the laser frequency. These effects are known as technical noise and are also governed by the linewidth $\Delta\lambda$ as an important parameter of a laser system. But also more fundamental effects contribute to the laser linewidth too, whereas in principal it needs to be distinguished between three different types of noise sources [51]:

- **Spontaneous emission:** For commonly used active media this effect is negligible because the stimulated emission is concentrated to very few and narrow resonator modes as well as to a very narrow spatial direction of emission. In contrast, the spontaneously emitted photons are statistically distributed in frequency space, with respect to the transition lineshape, as well as spatial direction, leading to a suppression over many magnitudes.

- **Amplitude fluctuations:** The number of photons n_{ph} contributing to stimulated emission is statistically fluctuating over time and can be described by the Poissonian distribution, with standard deviation $\sqrt{\bar{n}_{\mathrm{ph}}}$, thus a relative standard deviation of $\sqrt{\bar{n}_{\mathrm{ph}}}^{-1}$, respectively. Even by assuming a very low mean value of $\bar{n}_{\mathrm{ph}} \approx 10^{15}$ photons per second[6] yields a standard deviation of $\sqrt{\bar{n}_{\mathrm{ph}}} \approx 10^{7.5}$ and therefore a small contribution.

- **Phase fluctuations:** If a photon is spontaneously emitted into the lasing mode it is amplified by stimulated emission and overlaps with the already existing coherent light wave. The contribution to the total amplitude is thereby small, but the phase

[6] A value of 10^{15} photons per second corresponds to a very low power of 1 mW inside a cavity at a wavelength of $\lambda = 633\,\mathrm{nm}$.

of this light wave is statistically distributed, since spontaneous emission is a random process. Thus phase fluctuations are introduced to the laser light.

Altogether the fundamental linewidth $\Delta\nu_\mathrm{L}$, as a lower boundary without technical noise, is given by [51]

$$\Delta\nu_\mathrm{L} = \frac{\pi h\nu_\mathrm{L}\Delta\nu_\mathrm{R}^2(N_\mathrm{sp} + N_\mathrm{therm} + 1)}{2P_\mathrm{out}}, \tag{3.21}$$

with the lasing frequency $\nu_\mathrm{L} = c/\lambda$, the resonator linewidth $\Delta\nu_\mathrm{R}$, the optical output power P_out, and the number of photons N_therm and N_sp, which are emitted into the lasing mode by means of thermal and spontaneous processes. At room temperature the number of thermally emitted photons is negligibly small, at least at common optical frequencies. The lowest value for spontaneously emitted photons is $N_\mathrm{sp} \geq 1$, since at least one photon needs to start the lasing operation. With that, the well-known Schawlow-Townes linewidth can be obtained [52]

$$\Delta\nu_\mathrm{L} \geq \frac{\pi h\nu_\mathrm{L}\Delta\nu_\mathrm{R}^2}{P_\mathrm{out}}. \tag{3.22}$$

Clearly, the resonator linewidth strongly affects the laser linewidth, as well as the optical power does because both influence the ratio between stimulated and spontaneous emission, i.e. the narrower the resonator transition the less likely a photon is spontaneously emitted into the lasing mode and the higher the power the smaller the contribution of spontaneously emitted photons compared to the stimulated ones.

Since the Schawlow-Townes linewidth fundamentally limits the achievable linewidth of a laser system, it is obviously favourable to approach this value. Unfortunately in practice often the technical noise by far dominates the contribution to the actual linewidth, with one prominent exception, the bare laser diode. Due to its tiny cavity spacing, leading to a poor resonator linewidth, it results in a laser linewidth not far above the Schawlow-Townes linewidth. Nevertheless, various techniques can be utilized to externally reduce the linewidth of a laser system, whereas some are covered in the following sections, especially regarding diode laser systems.

3.2 External-Cavity Diode Laser (ECDL)

The core component of a diode laser is clearly the laser diode (LD), whereby further external components are added to enhance the properties of it, e.g. linewidth reduction and frequency selection. The LD as a coherent semiconductor photon source offers unique features like high efficiency, small component size, or high cost effectiveness. But also suffers from large manufacturing tolerances, leading to an often different behaviour of diodes which are basically from the same type.

In the first subsection the LD is introduced, followed by the two types of external-cavity diode laser[7] (ECDL) configurations used throughout this thesis.

[7] Also called extended-cavity diode laser, as one facet of the LD acts as a cavity mirror.

3.2.1 Laser Diode (LD)

A LD consists of different semiconductive materials and, as common in solid matter, a large number of atoms are involved. Thus, considering single atomic states is no longer practicable, instead a description via electronic band structures can be used. Thereby energy bands represent a quasi-continuous energetic region which electrons can occupy, in contrast to energetically forbidden regions called band gaps. The distribution of occupied energy states is governed by the Fermi-Dirac statistic, whereas at zero temperature the Fermi energy E_F states the energy of the highest occupied state. For temperatures above absolute zero the Fermi level μ needs to be utilized then. Further, usually only two out of a large amount of energy bands need to be considered for a sufficient description of many properties of crystalline solid matter. These two energy bands are known as valence band (VB) and conduction band (CB), which are separated by a band gap with energy E_g. The Fermi level thereby defines the VB and CB, whereas for semiconductors the Fermi level lies in between the lower-lying VB and the upper CB, implying a fully occupied VB and a completely empty CB at $T = 0$, similar to insulators. Therefore there exists no strict distinction between insulators and semiconductors, but for the latter usually the band gap is small enough that at room temperature a non-negligible amount of electrons can be thermally excited to the CB [53].

To add free charge carriers[8] to the system it is doped with another atomic species, whereas usually it is distinguished between p- and n-doped materials which either add quasi-free electron holes or electrons, respectively. If they are brought together a so-called p-n junction is formed at the interface between the two materials. At equilibrium a space charge region, or depletion layer, is established where nearly all free charge carriers cancel each other out due to their opposite charge. This is initiated by a diffusive process because a p-doped (n-doped) material has an excess of free electron holes (electrons) in contrast to the other material. But every recombined and thereby lost electron-hole pair leaves a negatively and positively charged immobile ion at the p-doped and n-doped material near the p-n junction, leading to the formation of an electric field, which is opposed to the diffusion process and an equilibrium can be established. The spatial extent of the depletion layer is inversely proportional to the dopant concentration, which can be explained by the fact that a stronger doped material also has a higher density of immobile ions and therefore creates a stronger electric field which counteracts the diffusion process. To again populate the CB (VB) with free electrons (holes) an electrical current needs to be injected by applying a positive voltage high enough to overcome the electric field at the depletion zone, this is known as forward biasing a p-n junction. Charge carriers are then supplied by the current source and travel, roughly speaking, from the outer edge of the device, i.e. electrons from the n-doped and holes from the p-doped side, through the p-n junction and quickly recombine with the vastly available oppositely charged carriers there. Whereas every recombination process provides an

[8] Charge carriers which contribute to the material conductivity are the negatively charged electrons in the CB and the positively charged electron holes in the VB, or shortly just called holes. The selected atoms used as dopants have an additional weakly bound charge carrier each, which is already released at room temperature and contributes to the conductivity.

excess energy $\gtrsim E_g$, which can be disposed via a radiative or non-radiative process, e.g. emission of a photon or phonon, respectively. Electron-hole pairs can also be created via absorption of photons with high enough energy, as well as stimulated emission is possible too. For all three processes shown in Fig. 3.4 the corresponding states need to be

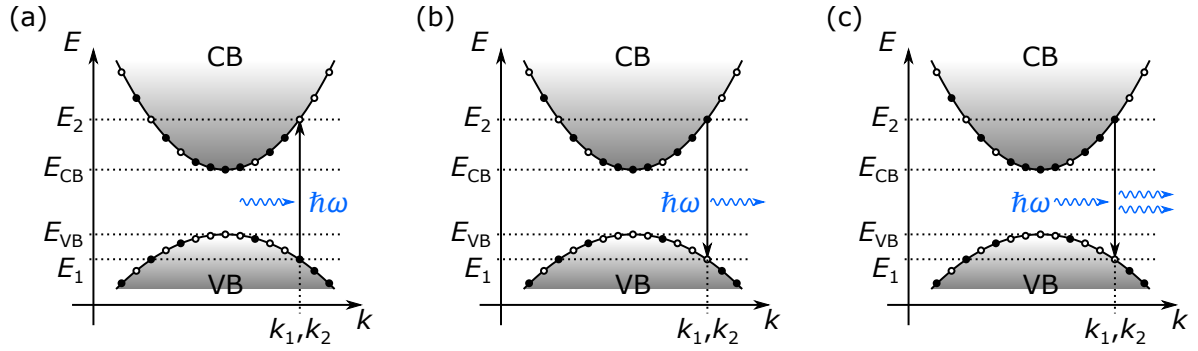

Figure 3.4: Schematic energy-momentum diagram $E(k)$ for a direct-bandgap p-n junction, i.e. the energy minimum E_{CB} of the CB and the energy maximum E_{VB} of the VB coincide at the same wavenumber k, with $E_g = E_{CB} - E_{VB}$. The energy states are quantized (depicted as small circles, black means occupied by an electron and white not) and can be well approximated by a parabola $E \propto k^2$ near the minimum or maximum, respectively. The wavenumbers k are equally spaced by π/d, with the crystal lattice constant d of the semiconductor material. Conservation of energy as well as momentum need to be fulfilled for every electron-hole pair generation or recombination process. Therefore, by just considering radiative processes, the photon energy $\hbar\omega$ needs to equal the energy difference of the two involved states, e.g. $E_2 - E_1 = \hbar\omega$. Additionally, the momentum difference of the electron, with momentum $\hbar k_2$, and the hole, with $\hbar k_1$, must equal the photon recoil, i.e. $k_2 - k_1 = 2\pi/\lambda$. But the momentum of the photon is negligibly small compared to the huge range of allowed momentum values which can be occupied by the charge carriers, wherefore the condition $k_2 \approx k_1$ can be assumed to hold [42]. Considering the three possible mechanisms for interaction with light: (a) absorption of a photon leads to the generation of an electron-hole pair, (b) spontaneous recombination leads to a spontaneously emitted photon, and (c) induced recombination leads to stimulated emission of a photon.

available and occupied, e.g. for photon emission an electron needs to occupy a state with energy E_2 and momentum k in the CB and a hole needs to occupy a state with energy E_1 and momentum k in the VB. The density of states available for photon interaction is given by the so-called optical joint density of states[9] $\varrho(\omega)$ which can be considered as a material parameter and increases with $\varrho(\omega) \propto \sqrt{\hbar\omega - E_g}$ [42]. The occupancy probability, an the other hand, is given by the Fermi distribution, i.e. the Fermi function for emission $f_e = f_{CB}(E_2)[1 - f_{VB}(E_1)]$ and for absorption $f_a = [1 - f_{CB}(E_2)]f_{VB}(E_1)$,

[9] The optical joint density of states $\varrho(\omega)$ incorporates the density of states of the CB and the VB. It expresses the number of states per unit volume and frequency interval [42]. Sometimes just called density of states, for the sake of convenience.

with the Fermi functions

$$f_{\mathrm{CB;\,VB}}(E) = \left[\exp\left(\frac{E-\mu_{\mathrm{CB;\,VB}}}{k_{\mathrm{B}}T}\right)+1\right]^{-1} \tag{3.23}$$

of the CB and VB, as well as the Fermi levels μ_{CB} and μ_{VB}, respectively.

The actual transition probability can similarly be described as in the case of a TLS considered in Section 3.1, but now with the lifetime τ_{r} of a radiative electron-hole recombination process. Hence, the spectral absorption and emission rates are determined by [42]

$$r_{\mathrm{absorp.}}(\omega) = F_\omega \frac{1}{\tau_{\mathrm{r}}} \frac{c^2\pi}{2\omega^2 n_{\mathrm{ref}}^2} \varrho(\omega) f_{\mathrm{a}}(\omega) \tag{3.24}$$

$$r_{\mathrm{st.em.}}(\omega) = F_\omega \frac{1}{\tau_{\mathrm{r}}} \frac{c^2\pi}{2\omega^2 n_{\mathrm{ref}}^2} \varrho(\omega) f_{\mathrm{e}}(\omega) \tag{3.25}$$

$$r_{\mathrm{sp.}}(\omega) = \frac{1}{\tau_{\mathrm{r}}} \varrho(\omega) f_{\mathrm{e}}(\omega), \tag{3.26}$$

with the spectral photon flux density F_ω per unit frequency. Therefore the product $\varrho(\omega) f_{\mathrm{e}}(\omega)$ is the analogon to $g_{\mathrm{ls}}(\omega) N_2$ for emission and $\varrho(\omega) f_{\mathrm{a}}(\omega)$ with $g_{\mathrm{ls}}(\omega) N_1$ for absorption, where g_{ls} is the lineshape function of the gain medium. Further the gain coefficient γ_{LD} again results from the difference between stimulated emission and absorption, thus

$$\gamma_{\mathrm{LD}}(\omega) = \frac{1}{\tau_{\mathrm{r}}} \frac{c^2\pi}{2\omega^2 n_{\mathrm{ref}}^2} \varrho(\omega) f_{\mathrm{g}}(\omega), \tag{3.27}$$

with the Fermi inversion factor $f_{\mathrm{g}}(\omega) = f_{\mathrm{e}}(\omega) - f_{\mathrm{a}}(\omega)$ being analogous to the population inversion $N = N_2 - N_1$ from above.

Accordingly, the p-n-type semiconductor forms the active medium necessary for laser operation, whereas the pumping mechanism is given by the injected current provided by a power supply with injection rate R_{p}, giving the number of generated electron-hole pairs per second and unit volume. At steady-state the charge carrier densities can be denoted by $n_{\mathrm{e}} = n_{\mathrm{e},\,0} + \Delta n_{\mathrm{e}}$ and $n_{\mathrm{h}} = n_{\mathrm{h},\,0} + \Delta n_{\mathrm{h}}$ for electrons and holes, respectively, whereas $n_{\mathrm{e},\,0}$ ($n_{\mathrm{h},\,0}$) denotes the electron (hole) density at thermal equilibrium and $\Delta n_{\mathrm{e}} = \Delta n_{\mathrm{h}} = \Delta n = \tau R_{\mathrm{p}}$ the excess carrier concentration originating from the injected current i, with the total lifetime $\tau = (\tau_{\mathrm{r}}^{-1} + \tau_{\mathrm{nr}}^{-1})^{-1}$ of the electron-hole pairs, combining radiative, τ_{r}, and non-radiative, τ_{nr}, decays. Considering an electric current flow i perpendicular to the plane of the active region with thickness d_{gain} and area A, the pump rate is given by the number of electron-hole pairs generated per unit time, hence

$$R_{\mathrm{p}} = \frac{i}{eAd_{\mathrm{gain}}}, \tag{3.28}$$

with the electron charge e.

However, the spectral distribution of the gain coefficient, i.e. the gain profile of the LD, is further determined by the density of states $\varrho(\omega)$ along with the Fermi inversion

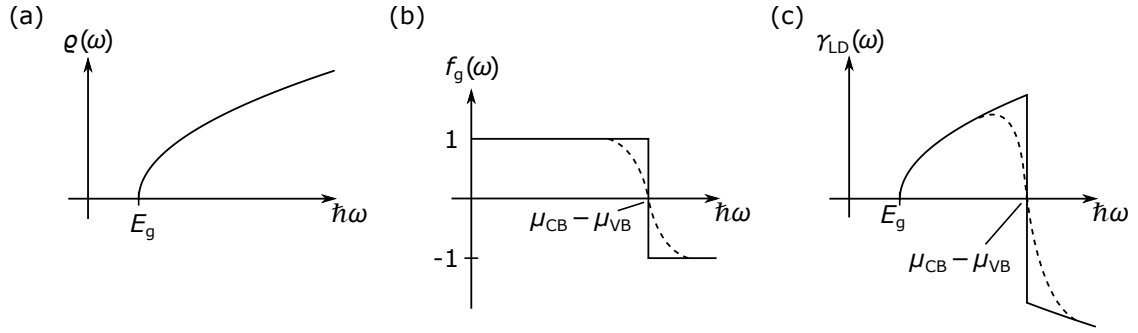

Figure 3.5: The optical joint density of states $\varrho(\omega)$ and the Fermi inversion factor $f_\mathrm{g}(\omega)$ determine the spectral shape of the gain coefficient $\gamma_\mathrm{LD}(\omega)$, with photon frequency ω. The gain profile is clearly asymmetric, but smoothes out with increasing temperature (solid curves at $T = 0$ and dashed curves at $T > 0$). The change with temperature depends on the Fermi functions and is just exemplified here, but with increasing temperature the peak gain is reduced and shifted to lower photon frequencies. Additionally, the bandgap energy E_g is shifted too, but strongly depends on the semiconductor material, e.g. for GaN it shifts to lower energies with increasing temperature [54]. Clearly, amplification is just possible within the spectral region $E_\mathrm{g} < \hbar\omega < \mu_\mathrm{CB} - \mu_\mathrm{VB}$.

factor $f_\mathrm{g}(\omega)$ and therefore depends nonlinearly on the temperature T and the injection rate R_p. The temperature dependence directly arises from the Fermi functions, whereby the peak gain is shifted as well as the peak value, as depicted in Fig. 3.5. The dependence on the pumping rate and thereby the excess carrier density Δn is less straight forward, but can be stated at $T = 0$ via the change of the Fermi levels [42]

$$\mu_{\mathrm{CB;\,VB}}(\Delta n) = E_{\mathrm{CB;\,VB}} \pm (3\pi^2)^{2/3} \frac{\hbar^2}{2m_{\mathrm{e;\,h}}} \Delta n^{2/3}, \tag{3.29}$$

with the effective mass of the electron m_e and hole m_h, respectively, which can be seen as material parameters in this context. Further the condition $\Delta n \gg n_{\mathrm{e},0}, n_{\mathrm{h},0}$ needs to hold in order to neglect the equilibrium electron (hole) density, which is usually fulfilled for decent pumping rates. Thus by increasing Δn, the difference $\mu_\mathrm{CB} - \mu_\mathrm{VB}$ between the Fermi levels increases too, as well as the number of possible transitions for light amplification, since there are simply more states occupied by electrons (holes) in the CB (VB). Therefore the upper energy threshold of γ_LD in Fig. 3.5 is shifted to higher frequencies as well as the peak value increases too. To summarize, a higher pump rate increases the bandwidth and the magnitude of the LD gain profile, but in a non-trivial way. Nevertheless, the peak value of the gain coefficient [42]

$$\max(\gamma_\mathrm{LD}) \propto \Delta n - \Delta n_\mathrm{th}$$

can be linearly approximated with respect to the excess carrier density Δn and is valid well above the threshold[10] Δn_th. It is determined via the threshold pump rate R_p^th,

[10] The excess carrier density threshold Δn_th is also called the transparency carrier density, as absorption and emission balance each other at this value, wherefore the material is effectively transparent then.

respectively the injected current threshold i_{th}, where the total gain equals the total loss. Thus, in relation to Eqs. (3.20) and (3.28), the optical output power P_{out} above threshold is proportional to the electrical current i via

$$P_{\mathrm{out}} = \eta_{\mathrm{s}} \frac{\hbar\omega}{e}(i - i_{\mathrm{th}}), \tag{3.30}$$

where the slope efficiency η_{s} states the number ratio between the emitted photons and the injected electrons per time and therefore directly relates to the efficiency, i.e. external current versus emitted optical power.

Again, the threshold pump rate $R_{\mathrm{p}}^{\mathrm{th}}$ can only be lowered by reduction of the total losses, assuming the same gain material. But in practice often just the threshold current i_{th} is considered, with the aim to increase the effectiveness of the injected current, in other words, achieving a higher pump rate with the same injected current. But this is only possible by decreasing the volume of the active region, which can be seen with Eq. (3.28). Therefore a so-called double heterostructure is utilized, where two junctions between two different semiconductor materials are formed, more precisely a p-p-n heterojunction structure, depicted in Fig. 3.6. Thus, a p-doped material offer-

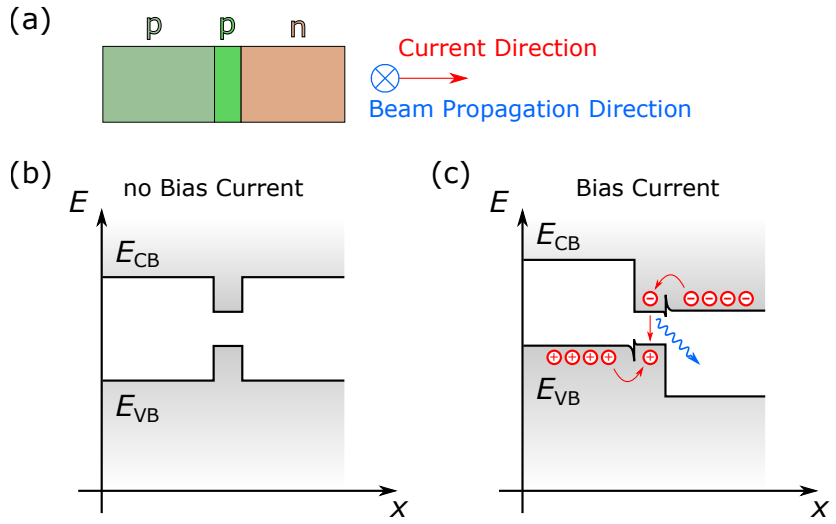

Figure 3.6: (a) The structure of a p-p-n-type double heterojunction, with the direction of the injected current and the emerging light beam. This structure is utilized to enable a much lower lasing threshold current i_{th}. (b) At thermal equilibrium without a bias current the CB and the VB offer a discrete energy jump at the interface of the two different materials. (c) After applying a forward current the electrons (holes) injected at the edge of the n-doped (p-doped) semiconductor are confined to a small region provided by the lower bandgap material. The potentials of the CB and VB change due to the external current, leaving a negligible barrier for the charge carries to enter the low bandgap region, but a significant potential well for leaving the region [50]. Therefore the electron-hole recombinations are concentrated to that zone, causing a substantially higher excess charge carrier concentration, thus a lower threshold current.

ing a lower bandgap E_{g1} is surrounded by a p- and n-doped material with a higher bandgap $E_{g2} > E_{g1}$. The bandgap difference offers a potential barrier for the charge carriers, which thereby can be confined to a small region, smaller than the carrier diffusion length would be in the same semiconductor material. The result is a much higher current density with the same injected current. Additionally, the radiation generated in the active region, i.e. now mainly the p-doped material with lower bandgap, does not suffer from excessive re-absorption in the surrounding materials, since the bandgaps substantially differ. Further, a semiconductor material with lower bandgap almost always has a higher refractive index compared to a high-bandgap material [50]. Thus, a waveguiding mechanism can be realized to also confine the light field near the active region, causing a higher field intensity as well as the possibility to achieve lasing at a single transversal mode along the current direction.

By also making use of a confinement along the lateral direction, i.e. perpendicular to the p-n current direction and perpendicular to the beam propagation direction, the concentration of charge carriers, as well as photons, can be further increased. Therefore the area of the injected current is constricted to a small stripe through the pn junction by decreasing the size of the contact metal pad, where the semiconductor is contacted to the environment, and surrounding it with an isolating material. Thus, the gain coefficient varies in the lateral direction due to the change of the excess carrier concentration, wherefore the light field is (weakly) guided to regions offering a higher gain during lasing operation. The dependence of the refractive index on the current density further provides a weak field confining mechanism, since a higher current density yields a slightly higher refractive index, known as the gain-guiding mechanism [55].

By further implementing a material with lower conductivity, higher bandgap, and lower refractive index outside of the symbolic narrow stripe indicated by the contact metal pad along the current direction, an index-guiding mechanism is achieved, illustrated in Fig. 3.7. Thereby the current density is confined due to the change of the electrical resistance, the electron-hole pair recombination events are confined due to the different bandgaps, and the waveguiding mechanism is achieved via the change of the refractive index, which is ideally only supporting a single transversal mode along the lateral direction, too. In practice the gain-guided LDs are easier to fabricate, but index-guided LDs offer a much higher and more stable field confinement. Thus, the former are typically used as a high power optical pumping source and the latter as a single transversal mode laser with a low current threshold [50]. Finally the light field is confined in two dimensions leaving the third as light propagation direction, referred as longitudinal direction as opposed to the two transversal directions.

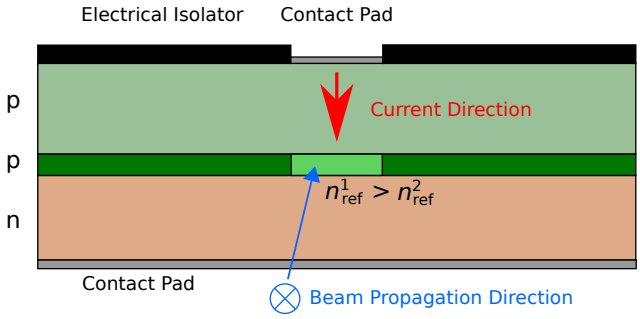

Figure 3.7: Schematic of a p-p-n-type double heterojunction index-guiding laser structure.

To actually achieve lasing operation the semiconductor gain material needs to be placed inside a resonator to establish a positive feedback, thus stable oscillation. The most straight-forward method is to directly use the end facets of the semiconductor as cavity mirrors, since the commonly used materials offer a adequate refractive index step with respect to surrounding air. These types are known as edge-emitting Fabry-Perot diodes. But the medium cannot be considered purely homogeneous, wherefore the refractive index is usually stated as an effective refractive index $n_{\mathrm{ref}}^{\mathrm{eff}}$ with typical values $n_{\mathrm{ref}}^{\mathrm{eff}} \approx 3 \ldots 3.5$ [50]. In contrast, the refractive index of gallium nitride (GaN) semiconductor material is approximately 2.5 at a wavelength of 400 nm [54]. The reflectance R at the interface layer in the case of normal incidence can be calculated by using the Fresnel equations, thus

$$R = \left| \frac{n_{\mathrm{ref}}^{\mathrm{eff}} - 1}{n_{\mathrm{ref}}^{\mathrm{eff}} + 1} \right|^2 , \tag{3.31}$$

with typical values of 30(10) %. For single-side emission of laser radiation one facet usually offers a high reflectivity, wherefore the other facet dominates the contribution to the cavity Finesse, respectively the cavity photon lifetime.

Nevertheless, the free spectral range FSR^{LD} of the cavity is determined by the optical path length along the longitudinal direction, thus $n_{\mathrm{ref}}^{\mathrm{eff}} \cdot d_{\mathrm{cav}}^{\mathrm{LD}}$, with the physical semiconductor length $d_{\mathrm{cav}}^{\mathrm{LD}}$. Typical values of the optical path length are below 1 mm, leading to a free spectral range of $FSR^{\mathrm{LD}} \approx 150\,\mathrm{GHz}$. Considering a LD based on GaN the gain profile at room temperature can be approximated by a Gaussian function with a bandwidth of 2 nm, whereas the center wavelength can be manufactured in the range of $370 \ldots 500\,\mathrm{nm}$ [55, 54]. By comparing the bandwidth to the free spectral range, it turns out that the number of supported LD cavity modes is relatively small. But usually the saturation of the gain medium is at least weakly inhomogeneous, e.g. due to spectral hole burning, which probably leads to a MM operation with a dominate mode close to the center of the gain profile. Also increasing the pump rate typically increases the number of oscillating modes, but in close vicinity to the threshold this is not true. There, an enhancement of the pump rate can actually increase the power of the main mode because the initial gain is too small beforehand, wherefore the homogeneous saturation effect is too weak to effectively suppress other modes. The dominance of the main mode is quantified phenomenologically by the so-called side-mode suppression ratio $SMSR = 10\log(P_1/P_2)$, with the optical output power of the main mode P_1 and the second strongest mode P_2. Typically, Fabry-Perot LDs can reach a $SMSR$ of up to 20 dB [50]. However, due to the poor Finesse of the LD cavity the linewidth is not much smaller than the free spectral range, although further linewidth broadenings due to technical noise sources are not considered yet. Thus, for linewidth reduction and stability enhancement external components are utilized, most notably and conceptually easiest is to place the LD as gain material inside an external cavity, with enhanced cavity length and Finesse. Thereby the back facet of the LD usually serves as the end mirror of the external cavity and the front facet can be anti-reflection (AR) coated in order to minimize influences on the mode selection, which can greatly increase the tunability, but usually only has a small effect on the linewidth itself [56]. Then to facilitate wavelength

selection, frequency selective elements can be placed inside the cavity too. Thereby the attenuation is artificially increased at undesired spectral regions and due to mode competition a lasing mode near the desired frequency is more favourable to sustain. Further without an AR coated front facet a coupled cavity system is established by the internal and external cavity, leading to an additional spectrally dependent attenuation, which can either help to suppress side-modes for a more stable SM operation or interfere with the mode selection. It depends strongly on the coupling strength of the cavities and on several external parameters because the internal LD cavity cannot be controlled independently as compared to a standalone intracavity etalon, for example. Thus, it cannot be stated universally valid that an AR coated LD is always superior to a non-coated LD in the case of an ECDL system.

However, principally an ECDL addresses the following three main purposes: enhancement or enablement of wavelength tunability, linewidth reduction, and stability enhancement. Although linewidth and stability are closely related attributes, the former is often considered on short-term time scales, with respect to the experiment execution time, whereas the latter is generally used over the entire time scale. Further considerations can be found at the beginning of Chapter 4. Nevertheless, all ECDL systems have in common that the enhancement is accomplished via implementation of an external optical feedback loop. In the following subsections two types of ECDLs are considered, the first is based on an interference filter in a so-called cat-eye configuration and the second is based on the commonly known grating design in Littrow configuration.

3.2.2 ECDL in Cat-eye Configuration

Although the idea of utilizing an interference filter (IF) as wavelength selective element together with a cat-eye reflector, i.e. a combination of a lens and a mirror, to form a ECDL is not new [57], the cat-eye configuration is not a very common ECDL design, yet. This was probably due to the limited availability and high costs of a narrow bandwidth interference filter together with its limited peak transmission capabilities in the past. However, major improvements in the field of dielectric coatings lead to a better availability of narrow-band filters on a very broad wavelength region.

The main advantage of the cat-eye design, schematically shown in Fig. 3.8, arises from the fact that the frequency selection and the feedback generation is done by two distinct elements: the IF and the cat-eye reflector. It is advantageous because the beam diameter at both elements can differ, such that at the reflector the spot size can be made small in order to improve the feedback stability and much bigger at the wavelength selector. In contrast, by using a grating as wavelength discriminator, a bigger beam diameter is unavoidable because the achievable resolution is proportional to the spot size [51]. Therefore with an ECDL, where the grating combines the frequency selective element and the outcoupler, a compromise between resolution and alignment stability needs to be made. Additionally, the grating is often attached to a spring-loaded mount to enable fine changes of the grating angle, thus making it especially sensitive to acoustics and mechanical vibrations. Surely these drawbacks can be overcome with a more complex

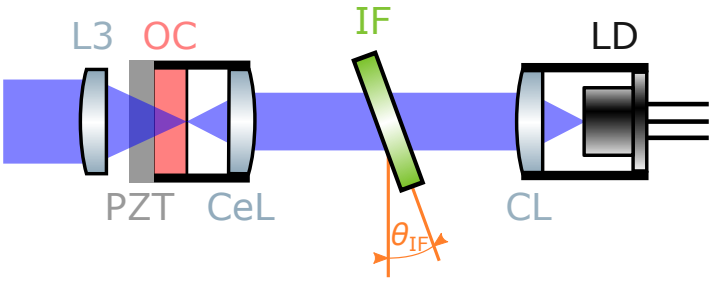

Figure 3.8: Optical setup of an ECDL in cat-eye configuration. The laser diode (LD) is mounted together with an aspheric lens (CL) inside a collimation tube, which is also thermally in contact with the LD and a thermal control. The collimated beam is guided through a narrow passband interference filter (IF), which is mounted on a rotation stage for coarse wavelength selection. The cat-eye reflector is formed by the cat-eye lens (CeL) and the outcoupler (OC), i.e. a partially reflective mirror. To enable cavity length tuning the cat-eye reflector is fitted on a piezoelectric transducer (PZT), whereas the distance between CeL and OC remains fixed. Another lens (L3) finally collimates the beam before laser output.

grating design ECDL [58], but the IF implementation is conceptually superior in the areas of feedback stability and cavity misalignments especially with respect to acoustic noise sources [57, 59, 60]. Specifically, low-complex ECDL systems benefit from the conceptual advantages of the cat-eye design.

Mode Selection, Tunability, and Wavelength Sensitivity

The laser frequency is not solely determined by the transmission window of the IF[11], it is also correlated to the LD gain profile, the LD cavity, and the external cavity formed with the OC mirror[12]. In Fig. 3.9 the transmission of each component as well as the gain profile is depicted. Analogously, Fig. 3.10 shows the same plot, but with an AR coated LD.

Next, to alter the frequency the following parameters can be utilized:

- the LD temperature T_{LD},
- the LD injection current i_{LD},
- the mirror spacing of the external cavity, via a voltage u_{pzt} applied to a PZT,
- and the IF angle θ_{IF}.

The effects of these parameters on different laser properties are thereby not independent of each other and are summarized in Table 3.1. Additionally, the parameters act on different time scales, from fast to slow: i_{LD}, u_{pzt}, θ_{IF}, T_{LD}. Thus, in a closed-loop application the unfavourable correlation can be handled well. Furthermore the effects

[11] Semrock LL01-407-12.5 bandpass filter is used here.
[12] Partially reflective mirror with 20 % reflectivity at the front surface and <0.5 % at the back surface.

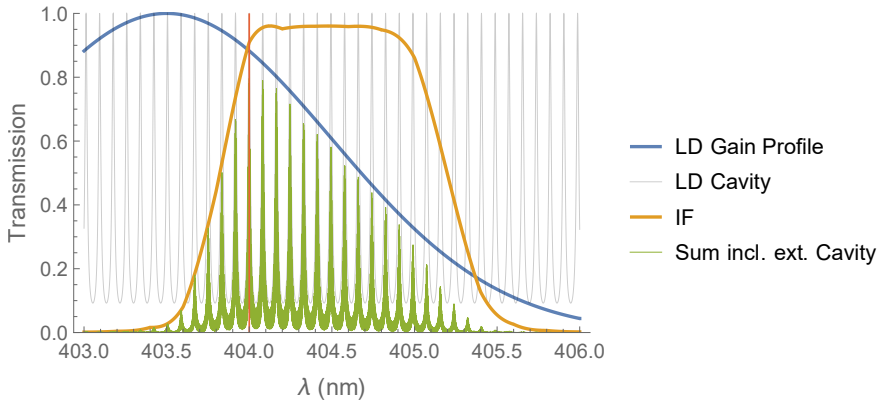

Figure 3.9: The transmission of each part together with the gain profile reveals the most favourable lasing mode (red line). The IF is rotated to a center wavelength of 404.5 nm. Thereby it is clearly visible that a sharp edge of the IF is more important than a narrow bandwidth. Additionally the finite slope of the gain profile, approximated by a Gaussian function, is of prime importance too. Further due to the narrow gain bandwidth of GaN diodes, the LD needs to be well chosen to fit the desired wavelength region without utilizing extreme LD temperatures. Due to the small FSR of the external cavity the modes are not distinguishable in this graphic.

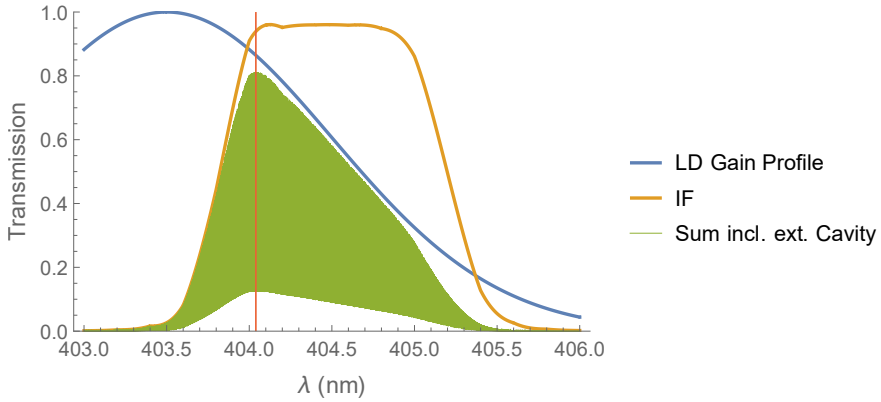

Figure 3.10: Analogous to Fig. 3.9, but with an AR coated LD. It can be advantageous for the tunability, but as a higher number of modes compete it can be unfavourable for SM operation, especially if inhomogeneous broadening is not negligible.

on the lasing mode and the gain profile need to be separated because firstly, altering the resonator mode directly changes the lasing frequency, whereas SM operation is assumed and secondly, a change of the gain profile shifts the cavity mode relative to it and the laser frequency does not change until a mode-hop occurs, i.e. a different resonator mode is more favourable then. Ideally, the laser mode and the gain profile shift in phase with each other, leading to a truly continuous tunable laser source. As the IF influences the total loss of the cavity, it can in principle be associated to the gain profile effects with respect to the grouping in Table 3.1.

parameter	**effect**	**influence on**	ν	**rel. significance, rate**
$T_{\mathrm{LD}} \uparrow$	material expansion	LD cavity	$\downarrow$	low, $10^{-6}\,\mathrm{K}^{-1}$ [61]
		ext. cavity	$\downarrow$	very low
	refractive index	LD cavity	$\downarrow$	high, $10^{-4}\,\mathrm{K}^{-1}$ [61]
		ext. cavity	$\downarrow$	—"—
	shift of gain peak	LD gain	$\downarrow$	high, Section 3.2.1, [42]
	gain reduction	LD gain	NA	negligible
	gain broadening	LD gain	$*\downarrow$	low [54]
$i_{\mathrm{LD}} \uparrow$	refractive index	LD cavity	$\uparrow$	[62, 54]
		ext. cavity	$\uparrow$	—"—
	shift of gain peak	LD gain	$\uparrow$	high, Section 3.2.1, [42]
	gain broadening	LD gain	$*\uparrow$	low, Section 3.2.1, [42]
	gain increase	LD gain	NA	negligible
	heating	$T_{\mathrm{LD}} \uparrow$	$\downarrow$	significant, but slower
u_{pzt}	ext. cavity length	ext. cavity	$\uparrow\downarrow$	
$\theta_{\mathrm{IF}} \uparrow$	transmittance	cavity losses	$\downarrow$	
	optical path length	ext. cavity	$\downarrow$	

Table 3.1: These parameters are often used to control the lasing frequency ν, whereas the arrows indicate the direction of change. The relative significance is considered with respect to the same external parameter and influence region, in order to evaluate the dominant effect, e.g. LD cavity: there the change of the refractive index due to increasing temperature has a much higher influence on the frequency than the material expansion has on the frequency. Effects on the optical output power are not considered here, e.g. a (uniform) reduction of the gain profile is significant for the output power, but negligible for the laser frequency. * The gain broadening with increasing T_{LD} is due to the shift of the bandgap energy [54], which determines the lower end of the gain profile, see Fig. 3.5. For GaN it shifts to lower energies, wherefore in principle lower frequencies are achievable. But this should not be mixed up with the shift of the gain peak, which is the dominant effect why lower frequencies are achievable with increasing temperature. Analogously for increasing current densities, the upper end of the gain profile is shifted upwards. Also, it needs to be mentioned that during laser operation the temperature of the LD housing, which can be controlled externally, does not coincide with the temperature T_{LD} of the semiconductor material, which influences the laser frequency. This is due to the finite junction-to-case thermal resistance. The direction of change for the piezo voltage u_{pzt} depends on the piezo mount. Where relevant: the change rate and direction is related to GaN LD.

However, the transmission window of the IF at normal incidence can be shifted to lower wavelengths by increasing the angle of incidence (AOI) θ_{IF}. The peak wavelength is thereby determined by [51]

$$\lambda_{\mathrm{IF}}(\theta_{\mathrm{IF}}) = \lambda_0 \sqrt{1 - \left[\frac{\sin(\theta_{\mathrm{IF}})}{n_{\mathrm{eff\,ref}}}\right]^2}, \tag{3.32}$$

with the peak wavelength at normal incidence $\lambda_0 = 407\,\mathrm{nm}$ and the effective refractive index of the IF $n_{\mathrm{eff\,ref}} \approx 2.01$. To reach a wavelength of 404.5 nm an AOI of $\tilde{\theta}_{\mathrm{IF}} \approx 13\,^\circ$ is necessary. Whereby the wavelength sensitivity

$$\frac{\mathrm{d}\lambda_{\mathrm{IF}}}{\mathrm{d}\theta_{\mathrm{IF}}} = -\frac{\lambda_0^2 \sin(2\theta_{\mathrm{IF}})}{2n_{\mathrm{eff\,ref}}^2 \lambda_{\mathrm{IF}}(\theta_{\mathrm{IF}})}\bigg|_{\theta_{\mathrm{IF}}=\tilde{\theta}_{\mathrm{IF}}} \approx -22\,\frac{\mathrm{pm}}{\mathrm{mrad}} \approx -0.39\,\frac{\mathrm{nm}}{^\circ} \tag{3.33}$$

is of peculiar interest as it heavily influences the susceptibility to vibrational noise. The highest sensitivity is reached at an AOI of 45 °, but IFs are designed for a particular AOI, which can usually just be altered in a small region without strong degradation of the transmission properties, especially for different light polarizations a strong separation occurs, too.

For comparison to the grating design ECDL, the grating equation

$$\lambda_{\mathrm{gr}}(\theta_2) = \frac{a}{q}[\sin(\theta_1) + \sin(\theta_2)] \tag{3.34}$$

needs to be considered, with the groove spacing a, the diffraction order q, along with the incident and diffracted beam angles θ_1 and θ_2, respectively. The sensitivity in Littrow configuration, i.e. $\theta_{\mathrm{gr}} := \theta_1 = \theta_2$, is thereby given by the inverse of the angular dispersion

$$\frac{\mathrm{d}\lambda_{\mathrm{gr}}}{\mathrm{d}\theta_{\mathrm{gr}}} = a\cos(\theta_{\mathrm{gr}})\bigg|_{\theta_{\mathrm{gr}}=\tilde{\theta}_{\mathrm{gr}}} \approx 190\,\frac{\mathrm{pm}}{\mathrm{mrad}} \approx 3.3\,\frac{\mathrm{nm}}{^\circ}, \tag{3.35}$$

with an AOI $\tilde{\theta}_{\mathrm{gr}} \approx 47\,^\circ$ for $\lambda_{\mathrm{gr}} = 404.5\,\mathrm{nm}$, $q = 1$, and the groove spacing $a = 3600^{-1}\,\mathrm{mm}$. Thereby the grating[13] with the highest available groove density was chosen to maximize the angular dispersion. Nevertheless, the sensitivity of the IF is still roughly 10 times lower compared to the grating design. Thus, the rotation stage for the IF needs to meet lower requirements regarding the mechanical stability. Additionally, as the alignment of the grating is critical, the rotation axis needs to be well aligned to one of the grating's symmetry axis and perpendicular to the beam propagation axis, otherwise a rotation alters the feedback too. As opposed to the IF design, where a rotation about an axis slightly misaligned to a symmetry axis of the IF or the beam propagation direction, in worst case just affects the transmission window with respect to the light polarization, the effect on the feedback is thereby negligible.

Feedback Sensitivity

An angular or translational displacement of the feedback element, i.e. the OC in cat-eye design and the grating in Littrow design, depicted in Fig. 3.11, misaligns the external cavity and therefore alters the feedback strength of the laser system. Assuming a Gaussian beam well aligned at the feedback element, the feedback strength F can be calculated via the overlap integral between the incident and reflected beam at the feedback element, thus [57]

$$F = \frac{R}{R_0} = \exp\left[-\left(\frac{\alpha\pi w_0}{\lambda}\right)^2\right], \tag{3.36}$$

[13] Thorlabs GH13-36U Reflective Holographic Grating

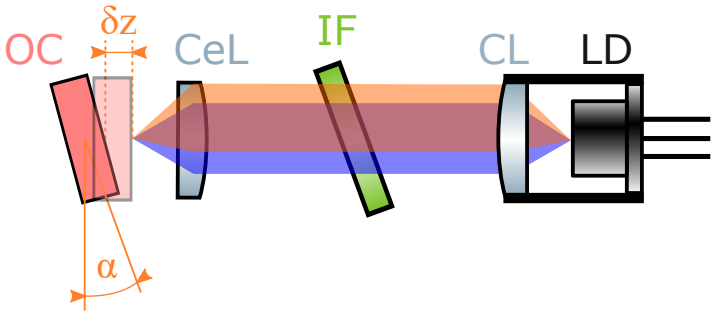

Figure 3.11: Schematic of the possible misalignments of the feedback element of an ECDL in cat-eye configuration. The OC can be angularly misaligned by α or translationally displaced by δz from the focal point of CeL.

with the beam waist[14] w_0 at the OC, the tilt angle α, as well as the reflectivity R_0 and R assuming perfect alignment and with included misalignments, respectively. Whereas the feedback strength is normalized over R_0 for convenience. As a measure of angular alignment tolerance the relation [57, 60]

$$\left|\frac{\mathrm{d}^2F}{\mathrm{d}\alpha^2}\right|^{-\frac{1}{2}} \approx \left|\frac{\mathrm{d}^2F}{\mathrm{d}\alpha^2}\right|^{-\frac{1}{2}}_{\alpha\to 0} = \frac{\lambda}{\sqrt{2}\,\pi w_0} \propto w_0^{-1} \tag{3.37}$$

can be used, whereas the lowest order Taylor expansion was applied. Clearly, a smaller spot size is advantageous.

Solving Eq. (3.36) for α and assuming a feedback decrease of 10 % lead to a maximum tilt angle of

$$\alpha_{\mathrm{IF},10\,\%} = \left.\frac{\lambda\sqrt{-\ln(F)}}{\pi w_0}\right|_{F=0.9} \approx 5\,\mathrm{mrad} \approx 0.3\,^\circ, \tag{3.38}$$

with $\lambda = 404.5\,\mathrm{nm}$, and $w_0 = 9\,\mu\mathrm{m}$. Compared to the grating design, the waist is typically a factor of 100 bigger and thereby the allowable tilt is a 100 times smaller too, thus $\alpha_{\mathrm{gr},10\,\%} \approx 50\,\mu\mathrm{rad}$.

Regarding a displacement δz along the optical axis, the feedback is determined by [60]

$$F = \left[1 + \left(\frac{\delta z \lambda}{\pi w_0^2}\right)^2\right]^{-1} \tag{3.39}$$

and the translational alignment tolerance is given by

$$\left|\frac{\mathrm{d}^2F}{\mathrm{d}\delta z^2}\right|^{-\frac{1}{2}}_{\delta z\to 0} = \frac{\pi w_0^2}{\sqrt{2}\,\lambda} \propto w_0^2. \tag{3.40}$$

Analogously a displacement of

$$\delta z_{\mathrm{IF},10\,\%} = \left.\frac{\pi w_0^2}{\lambda}\sqrt{\frac{1}{F} - 1}\right|_{F=0.9} \approx 0.2\,\mathrm{mm}, \tag{3.41}$$

[14] $1/\mathrm{e}^2$ beam radius

leads to a 10 % feedback decrease. Due to the quadratic relation the grating design retains a 10^4-fold greater value, thus $\delta z_{\mathrm{gr},10\,\%} \approx 2\,\mathrm{m}$, as compared to the IF design. But a mechanical stability of the order of $\delta z_{\mathrm{IF},10\,\%}$ is still conveniently manageable and a value in the metre range is anyhow irrelevant for practical use.

Realisation

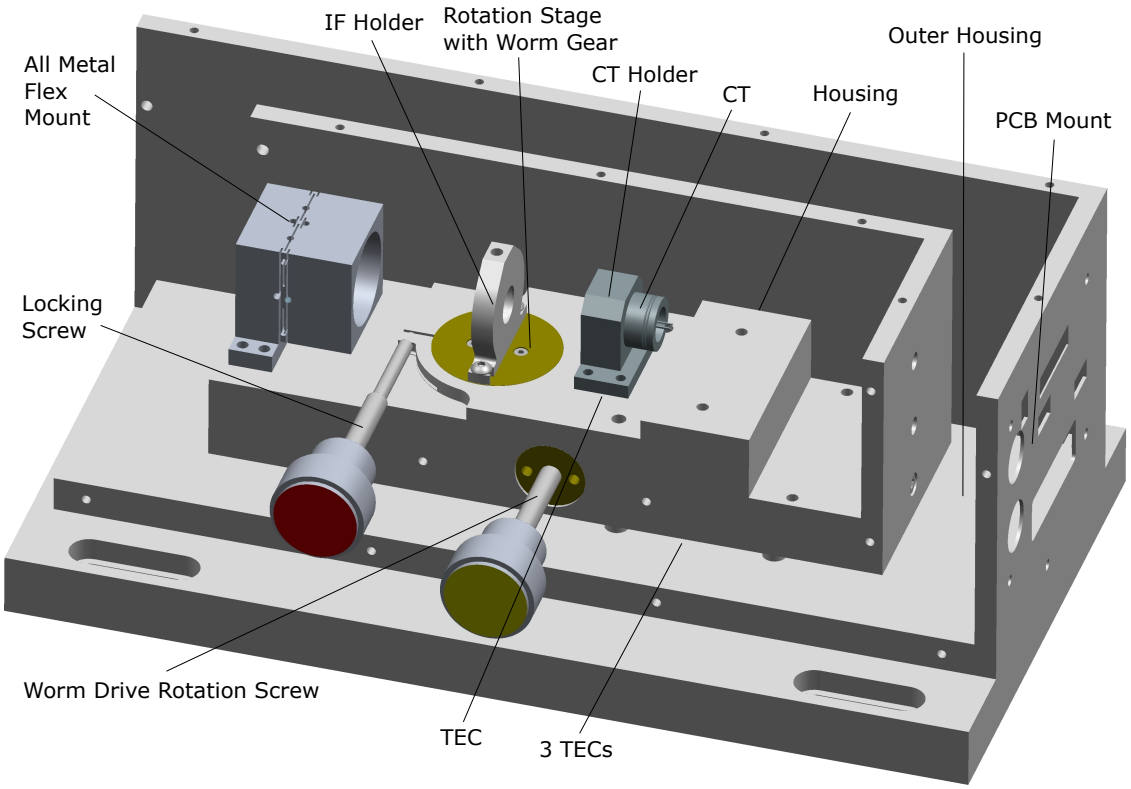

Figure 3.12: 3D model of the complete cat-eye laser system. For good thermal stability a double housing concept is utilized, as well as most of the parts are made out of aluminium. Two independent servo loops control the temperature of the LD and the housing. Whereby NTC resistors, thermally glued to the target, are used as temperature sensors together with several thermoelectric coolers (TEC) as control elements. The collimation tube (CT) is tightly fitted in the CT holder to ensure good thermal contact. The home made flex mount incorporates the OC, the CeL, the PZT, and the collimation lens before laser output. The worm gear driven rotation stage can be locked down after coarse wavelength adjustments. On the front face of the outer housing a home made PCB is mount, internally known as "measurement bridge". The housing design is internally in use for various diode lasers, especially in the infrared spectrum. Within the scope of stability and tunability the blue LDs are in general inferior to IR ones, therefore the cavity spacing is reduced significantly to a value of approximately 60 mm, accepting a linewidth enlargement instead.

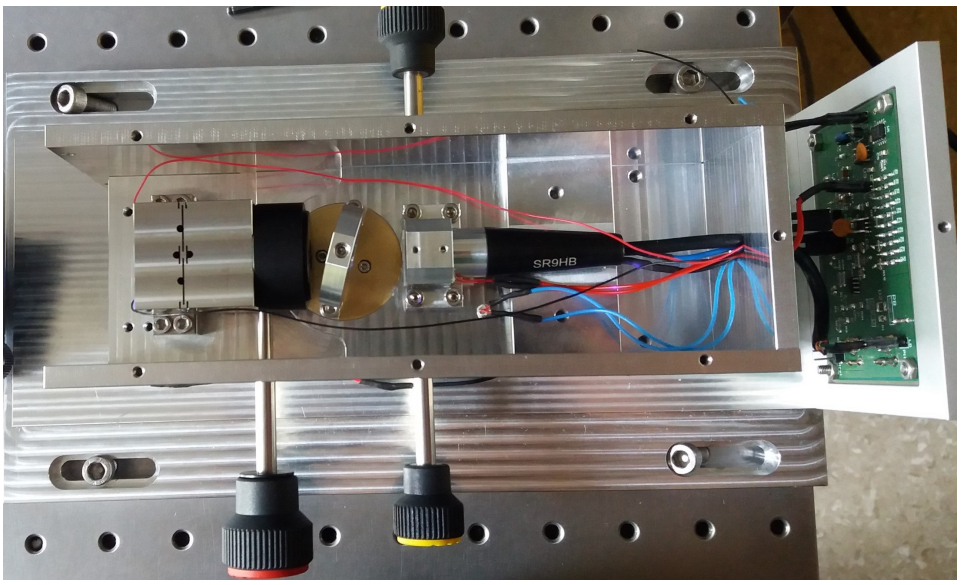

Figure 3.13: The complete cat-eye laser system without the outer housing. A lens tube is installed to use a CeL with higher focal length and therefore less strong focusing onto the OC.

In the desired deep blue wavelength regime the well-known GaN LD manufacturer Nichia[15] offers a LD model with a peak wavelength between 400 . . . 410 nm, thus the tolerance on the center wavelength is bigger than the bandwidth of the gain profile, wherefore the manufacturer was asked to pretest the LD in an ECDL setup for a wavelength of 404.5 nm. The LD comes in a TO 5.6 mm package and is mounted in a collimation tube (CT)[16], which is machined down on the outer diameter to precisely fit our custom made CT holder for a good thermal contact, but still allows a rotation about the optical axis. For temperature measurements a NTC resistor[17] is attached with thermal glue on the CT holder and for electrical contact an ESD protected plug[18] is used. The CT holder is thermally connected to the housing via a small thermoelectric cooler (TEC) and stainless steel[19] screws. The base plate incorporates a worm drive rotation stage for the IF and a locking screw to mechanically block the stage. The key part is the flex mount, which is custom made out of a single piece of steel for high stiffness and consequently a high vibrational resonance frequency, ideally, above sound frequency range. It incorporates the OC, the CeL, the PZT, and the collimation lens before laser output. Thereby the two lenses can be adjusted individually along the optical axis, whereas the PZT as a ring actuator displaces the complete flexible part, while keeping the distance between the OC and the CeL constant. The flex mount is designed by Dr. Emil Kirilov[20]. The

[15] Nichia NDVA111T datasheet https://www.nichia.co.jp/specification/products/ld/NDVA111T-E.pdf
[16] Thorlabs Laser Diode Collimation Tubes
[17] Standard 10 kΩ NTC with glass capsule
[18] Thorlabs ESD Protection and Strain Relief Cable - SR9HB
[19] Stainless steel is a bad thermal conductor in this context.
[20] emil.kirilov@uibk.ac.at

whole body is then doubly enclosed by aluminium plates, with small openings for beam output and electrical wires. Thereby the inner housing is thermally regulated too, by means of three TECs mounted between the base plates of the inner and outer housing. The NTC resistor is mounted in close vicinity to the CT holder. A 3D model of the complete cat-eye laser system is shown in Fig. 3.12 and the manufacture is depicted in Fig. 3.13.

En passant, there is no separate alignment mechanism implemented, which can be advantageous - precise machining obligatory - for a quick setup especially for an AR coated LD. But for small optimizations the clearance of the screws of the flex mount and the CT holder needs to be exploited, which turns out as a tricky work step. However, the Nichia LD just offers a low reflection coated front facet, with unknown reflectivity. In Fig. 3.14 the output power of the bare LD is plotted against the diode current. As the lasing threshold is reached it can be stated that the reflectivity is greater than the total losses of the LD and therefore not negligible. But for alignment steps it is advantageous if the LD emits laser radiation prior external feedback implementation.

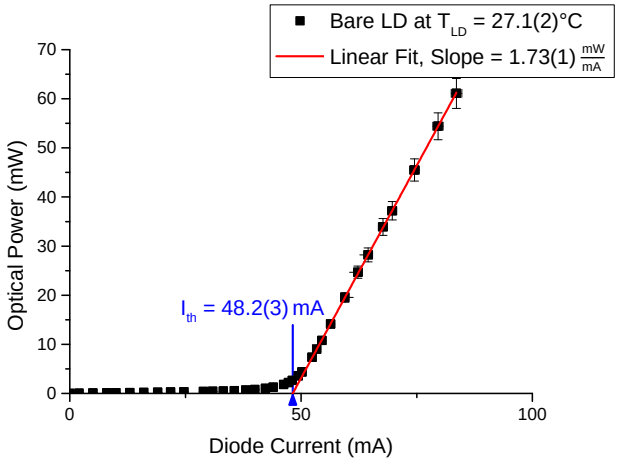

Figure 3.14: L-I curve of the bare low reflection coated LD.

A short summary of the alignment procedure First the light polarization is chosen by rotation of the CT. Then the beam is collimated with the CL while the IF and the flex mount is removed. The PZT together with the OC is clamped into the flex mount as well as the CeL is installed. The reflected beam can then be collimated by means of a beamsplitter (BS), temporarily placed inside the cavity with removed side panels. Alternatively a polarizing BS together with a quarter-wave plate can be used, too. For the cavity alignment the screws of the CT holder and the flex mount need to be loosen slightly, such that the parts can be rotated in the horizontal plane, but without toppling over vertically. If the diode current is set slightly below the threshold value of the bare diode, a successful feedback is recognized by a sudden increase in light intensity. This is because with an additional feedback the threshold current is lowered and the currently set current is above threshold then. Fine adjustments need even more patience

because minor displacements can occur while tightening the screws again. However, after installing the IF the alignment should be optimized once more since the beam is displaced slightly due to the finite thickness of the IF with an AOI above zero. A rough alignment before inserting the IF is highly recommended because the angle of the filter needs to be set correctly, otherwise the light attenuation is too high and the alignment process is nearly impossible. Lastly, the output collimation lens can be installed. For further optimizations it is necessary to check the SM operation of the diode laser, wherefore the beam is coupled into a Fabry-Perot interferometer (FPI)[21]. To prevent unwanted feedback from external parts an optical isolator[22] is installed after an anamorphic prism pair used for beam shaping. Reflections from the prisms are thereby not critical since the incidence angles are well above zero. With the aim of maximum optical power in SM operation, the CL and the CeL are fined tuned, thereby different light polarizations are tested too. Then the alignment procedure is carried out with different aspheric lenses for the CL and the CeL, while keeping in mind the clear aperture of the IF and a compromise between a small spot size at the OC for angle misalignment tolerance and a big spot size for translational tolerance. A good combination is found by the CL[23] and the CeL[24], with an effective focal length of $f_{\mathrm{CL}} = 4.3\,\mathrm{mm}$ and $f_{\mathrm{CeL}} = 13.4\,\mathrm{mm}$ at $\lambda = 400\,\mathrm{nm}$, respectively. With the beam divergence angles[25] $\Theta_{\mathrm{f}} \approx 40\,^\circ$ and $\Theta_{\mathrm{s}} \approx 19\,^\circ$ of the LD the collimated beam diameter $D_{\mathrm{f;\,s}}$ at the IF as well as the spot size at the OC can be calculated for the fast and slow axis, respectively. Thus,

$$D_{\mathrm{f;\,s}} = 2 f_{\mathrm{CL}} \tan\left(\frac{\Theta}{2}\right) \approx \begin{cases} 3.1\,\mathrm{mm} & \text{fast axis} \\ 1.4\,\mathrm{mm} & \text{slow axis} \end{cases} \tag{3.42}$$

$$2w_0^{\mathrm{f;\,s}} \approx \frac{4\lambda f_{\mathrm{CeL}}}{\pi D_{\mathrm{f;\,s}}} \approx \begin{cases} 2.2\,\mu\mathrm{m} & \text{fast axis} \\ 4.9\,\mu\mathrm{m} & \text{slow axis} \end{cases} \tag{3.43}$$

Although a bigger beam diameter would yield a better compromise between angle and displacement tolerance, the highest optical power under SM operation was achieved with this combination. The corresponding laser parameters are $T_{\mathrm{LD}} \approx 23.5(2)\,^\circ\mathrm{C}$, $i_{\mathrm{LD}} \approx 58(3)\,\mathrm{mA}$, and $P_{\mathrm{opt}} \approx 22(1)\,\mathrm{mW}$, with the power measured prior the prism pair. Unfortunately the monitor output of the home made LD current drive has an uncertainty of 3 mA, but the stability of the LD current is by far better. However, the actual value is not important, as it is intended as reference value for laser settings only.

The mode-hop-free range, i.e. the frequency range over which the laser wavelength can be tuned while staying in the same single external cavity mode, utilizing the PZT and thereby the external cavity length, can be stated as $\geq 0.5\,\mathrm{GHz}$, which is low, but sufficient for a fixed wavelength operation. Furthermore, part of the laser light is coupled into a fibre to access a wavemeter[26] or optical spectrum analyser for absolute frequency

[21] Thorlabs SA200-3B Scanning Fabry-Perot Interferometer
[22] Thorlabs IO-3D-405-PBS Free-Space Isolator
[23] Thorlabs C230TMD-A
[24] Thorlabs C560TME-A
[25] $1/e^2$ full angle; taken from the LD's datasheet
[26] HighFinesse Wavelength Meter WS/6-200

reference. It turned out that the tunability by rotation of the IF is below ±1.5 nm and the wavelength of the free-running LD without external feedback is about 402 nm at room temperature. The shift of the gain profile can be stated as 0.06 nm K^{-1}. Thus, it became apparent that a wavelength in the range of 404.5 nm was not achievable under SM operation, even by exhausting the maximum LD temperature of 55 °C. Therefore, no further investigations regarding stability and linewidth are made. As the manufacturer claimed a successful operation at 404.5 nm, with T_{LD} near room temperature, an ECDL in Littrow configuration is implemented as alternative.

3.2.3 ECDL in Littrow Configuration

The Littrow configuration, schematically shown in Fig. 3.15, is a very common diode laser design, as the number of necessary parts can be kept very low as well as the complexity for basic operation. Additionally, due to the inexpense of the reflection grating[27] the costs can usually be kept below those of the cat-eye design. However, it is preferable to

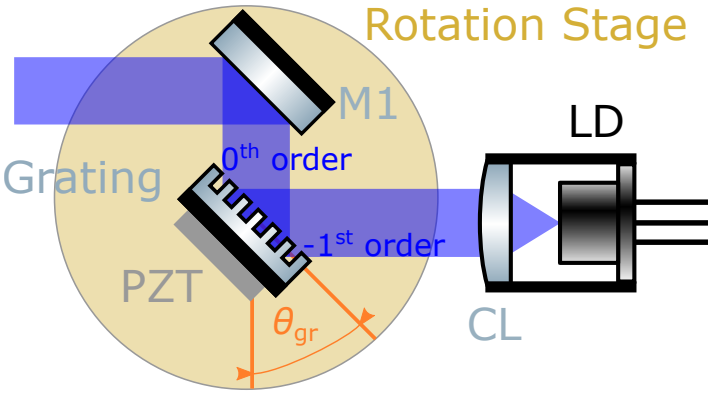

Figure 3.15: Optical setup of an ECDL in Littrow configuration. The laser diode (LD) is mounted together with an aspheric lens (CL) inside a collimation tube, which is also thermally in contact with the LD and a thermal control. The collimated beam is guided to a grating, which is mounted on a rotation stage together with a mirror (M1) that is kept in parallel. To enable cavity length tuning the grating is fitted on a piezoelectric transducer (PZT), whereas the diffracted beam of -1^{st} order is guided back to the LD. Via M1 it is ensured that the angle of the outcoupled beam is kept constant under rotation of the stage, even though a small lateral displacement of the beam is inevitable.

reuse the framework depicted in Fig. 3.12. Therefore the IF and the OC flex mount need to be replaced by the home made grating mount, with the model shown in Fig. 3.16 and the manufacture in Fig. 3.17.

Since the angular wavelength and feedback sensitivities are higher for the grating design, as posed in Eqs. (3.35) and (3.38), main attention is brought to the mechanical

[27] Thorlabs GH13-36U Reflective Holographic Grating is used here.

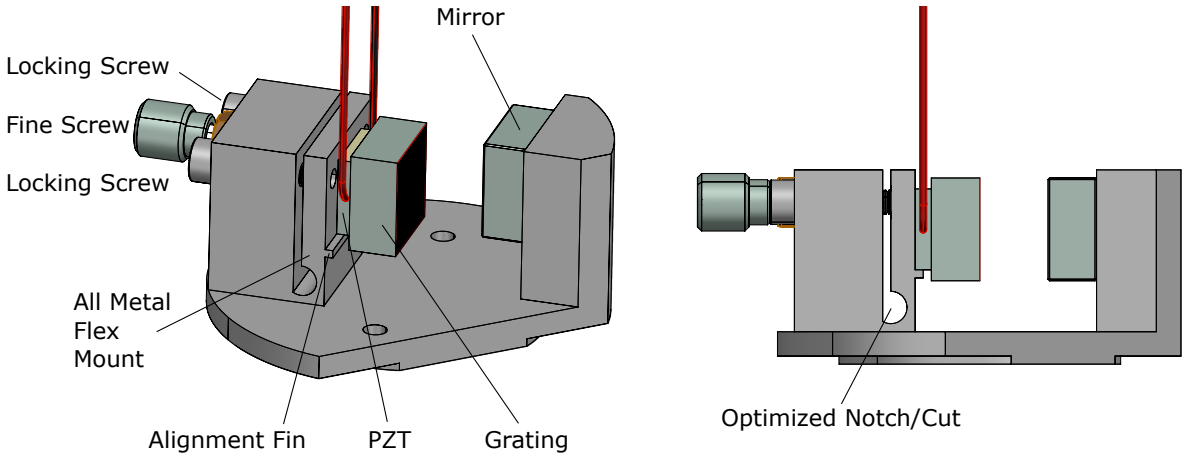

Figure 3.16: 3D model of the monolithic grating mount, which is installed on the rotation stage instead of the IF. The vertical angle of the grating can be precisely tuned by means of a fine screw, which is pushing on the flexible front part of the mount. Thereby a small sapphire pad is inserted at the contact point. Otherwise, on the long-term time scale and under significant tension the tip of the screw can be worked into the material and slightly misalign the laser cavity. Further, the movement can be locked by two standard screws, additionally increasing the rigidity and thereby the mechanical resonance frequency. A small fin is included to facilitate a precise mounting of the grating, whereby the grating is previously glued on a piezoelectric transducer (PZT), but also by utilizing an alignment help in the form of a milled metal step. Finally, the parallelism of the mirror M1 in the horizontal plane is ensured by manufacturing, therefore additional mechanisms for fine adjustments are not necessary.

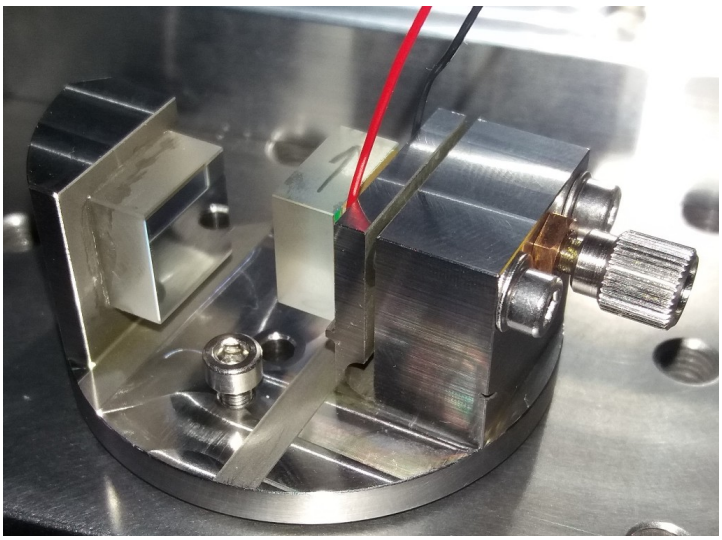

Figure 3.17: The monolithic grating mount is manufactured out of stainless steel by means of electrical discharge machining. Also the optical parts are already glued in place.

rigidity and resonance frequency of the grating mount. Whereas implementing fewer alignment mechanisms allow for a more rigid structure. As a minimum, the vertical angle of the grating needs to be aligned as well as the horizontal one for wavelength tuning, obviously. The horizontal angle is again altered by the worm drive rotation stage and with a mirror in parallel to the grating the outcoupled beam angle can be kept constant. Now, to avoid spring-loaded mounts a monolithic design, made out of stainless steel, was intended to align the grating's pitch angle together with a precise fine screw[28]. By means of a CAD software suite the flexural rigidity and the fundamental frequency of the flexure part is determined and optimized. Ideally, the lowest resonance should be above sound frequency range, implying an excessively high stiffness. But the fragile fine screw permits a maximum load of 85 N and therewith a significant vertical adjustment should still be possible. Finally, with the geometry of the notch represented in Fig. 3.16, the lowest resonance frequency is about 2.2 kHz, corresponding to the flex part alone. But thereby, with a force of 85 N, still a displacement of about 0.1 mm is realisable, as simulated in Fig. 3.18. This leads to a vertical beam adjustment range greater than ±0.5 mm at the position of the LD, what is more than enough for compensation of fabrication tolerances. Nevertheless, the two locking screws are introduced to clamp

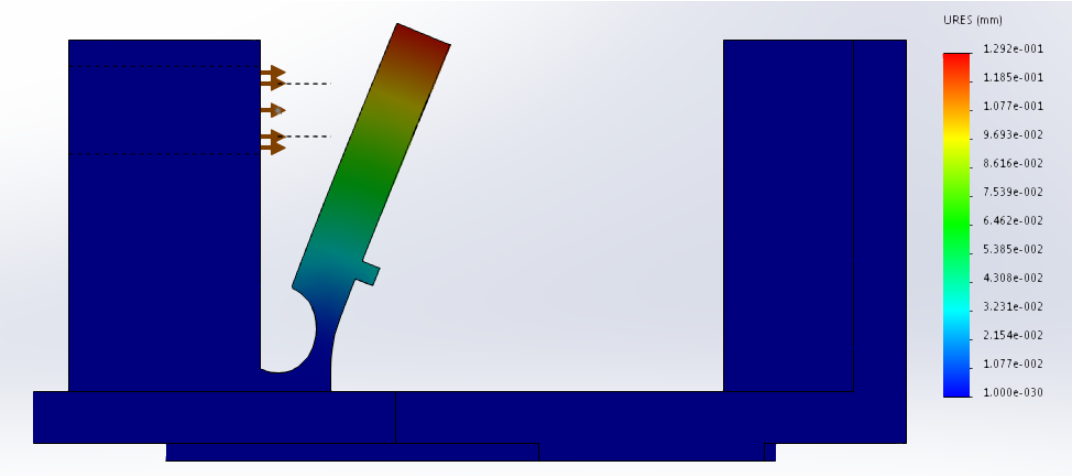

Figure 3.18: Simulation of the grating mount with the final geometry. With a force of 85 N at the tip of the fine screw (orange arrows) a tilt (expressed by the variable U_{RES}) of approximately 0.1 mm is possible. This bending mode also has got the lowest resonance frequency of about 2.2 kHz without including the locking screws.

down the flexure part after adjustment. As a result the new lowest resonance is above 11 kHz.

However, considering the optical properties, the holographic grating exhibits a reflectivity of approx. 8 % for p-polarized light as well as the cavity spacing is slightly smaller with respect to the cat-eye setup, too. Regarding the beam diameter, analogously to the filter design, a compromise between the resolving power and sensitivity needs to be

[28] Thorlabs M3 × 0.25 Adjustment Screw - MAS15

made, whereas a CL[29] with $f_{\mathrm{CL}} = 4.3\,\mathrm{mm}$ yields a satisfying result. Unfortunately, the gear reduction of the worm drive is too low, as it was particularly intended for IF rotation. Hence, the coarse wavelength selection via rotation can be a bit undependable as well as the reverse play of the gear has a greater impact now. Nevertheless, the desired wavelength $\lambda = 404.528\,\mathrm{nm}$ is accessible in SM operation, with a LD housing temperature $T_{\mathrm{LD}} \approx 42.5(2)\,^{\circ}\mathrm{C}$, current $i_{\mathrm{LD}} \approx 70(2)\,\mathrm{mA}$, and an output power $P_{\mathrm{opt}} \approx 26.2(3)\,\mathrm{mW}$ directly after laser output. Also a minimum temperature of $T_{\mathrm{LD}} \approx 40\,^{\circ}\mathrm{C}$ is necessary to achieve a wavelength near $\lambda = 404.5\,\mathrm{nm}$, so significantly above room temperature. The mode-hop-free range is further determined to be $\geq 0.7\,\mathrm{Ghz}$ and the tunability by rotation of the grating is well above $\pm 2\,\mathrm{nm}$, too. Thus decidedly higher with respect to the cat-eye setup. For the laser linewidth $\Delta\nu$, pro tempore, an upper limit of $7.5\,\mathrm{MHz}$ can be stated, given by the resolution of the FPI. Further considerations are made in Chapter 4, specifically in Section 4.1.2.

[29] Thorlabs C230TMD-A

4 Optical Setup

Usually the frequency of a free-running laser is not stable enough, neither on the short nor on the long-term time scale, originating from the change of environmental conditions and often classified into different noise sources depending on the relevant frequency ranges, e.g. acoustic and vibrational noise lead to mechanical movement of the laser components and therefore introduce lasing noise in the range of acoustic frequencies. The stability on the long-term time scale is often termed as *absolute stability*, as the change of the short-term average of the lasing frequency is much slower than the experiment execution time and mostly due to slow changes in environmental conditions, such as temperature, pressure, and humidity, as well as component ageing. But in detail it is different from *absolute frequency calibration*, strictly speaking, therefore it needs to be referred directly or indirectly to the defined frequency standard, i.e. the Cs ground state hyperfine (HF) transition. But experiments of the *national standards laboratories* establish some references of other atomic transitions to the caesium atom and therefore other transitions can be used for absolute calibration, e.g. the well-known 633 nm transition of the He-Ne laser [25]. The lasing noise, i.e. the change in frequency of the laser light, can also be related to the laser linewidth, whereas usually short time fluctuations are investigated when considering a laser for scientific use, except for the research field involving time and frequency standards.

Now, to increase the stability, or in other words calibrate the relative frequency of a given laser, one can utilize a more stable reference to lock at. Therefore a closed loop control needs to be set up to dynamically compare the actual lasing frequency with the reference system. Subsequently the difference, denoted as error signal, is used to change the parameters of the laser system until the signal vanishes. The feedback can thereby be realized optically and/or electronically, whereby as a reference often an external cavity, an atomic transition, or another laser system is used [42]. To realize such a feedback control system, respectively the error signal, several techniques have been established, such as the modulation transfer spectroscopy [63] or the Pound-Drever-Hall method [64].

I first want to focus on locking to a potassium vapour cell via modulation transfer spectroscopy, as the laser is designed to image ^{40}K, so it seems natural to use an atomic transition of potassium as a reference. Thus, to clarify

- the feedback is accomplished electronically based on a PID controller,
- the laser parameters to be changed, based on the error signal, are the external cavity length via a piezo and the internal optical path length of the semiconductor via the LD current. Hence, the controlling elements are voltage and current.

- The reference is given by Doppler-free laser spectroscopy, obtained via saturation absorption spectroscopy of a potassium vapour cell
- and the error signal is generated via modulation transfer spectroscopy, which is fed into the PID-controller and closes the loop.

4.1 Locking to a Potassium Vapour Reference Cell

The reference cell[1] contains potassium isotopes in natural abundance (^{39}K: 93.258(4) %, ^{41}K: 6.730(4) %, and ^{40}K: 0.0117(1) % [65]) and is filled with an approximate pressure of 10^{-7} mbar at room temperature[2]. Though the vapour pressure of potassium at room temp is roughly 10^{-8} mbar [65], wherefore part of the gas condenses and subsequently reaches the vapour pressure in equilibrium again. Due to the natural abundance the spectroscopy signal will be dominated by contributions of the ^{39}K isotope, therefore it will be used as a reference to ensure a strong laser lock. But then the level scheme of ^{40}K needs to be set in relation to ^{39}K, as shown in Fig. 4.1.

The frequency of a laser locked to the ground state crossover transition of ^{39}K, explained in the following subsection, is denoted by f_{lock} and needs to be shifted by an amount of 739 MHz to reach the desired imaging transition of ^{40}K, $|4S_{1/2}, F = 9/2\rangle \leftrightarrow |5P_{3/2}, F' = 11/2\rangle$. Still, the shift can conveniently be achieved with a single acousto-optic modulator (AOM) in double-pass configuration, i.e. the laser beam is passing the same AOM twice, thus frequency-shifted twice. Now, to actually determine the required shift the following considerations were made in relation to Fig. 4.1:

- The starting point is the ground state crossover situated midway between the two HF states of ^{39}K. It then needs to be related to the $4S_{1/2}$ degenerate state of ^{39}K, thus $-\frac{288.6+173.1}{2} + 173.1 = -57.8$ MHz.
- Next, including the energy shift of the $|4S_{1/2}, F = 9/2\rangle$ HF state of ^{40}K: +571.5 MHz,
- as well as the isotope shift of the $5P_{3/2}$ degenerate excited state of ^{40}K $\approx +240$ MHz,
- and the energy shift of the $|5P_{3/2}, F = 11/2\rangle$ HF state of ^{40}K: -15.0 MHz,

lead to a total amount of 739 MHz, with the highest uncertainty introduced by the value of the isotope shift [37].

4.1.1 Saturated Absorption Spectroscopy

Considering an atomic sample at room temperature illuminated by monochromatic light with frequency ω and wavenumber $k = 2\pi/\lambda$. The atom velocities then can be well described by the Maxwell speed distribution and the light as seen from the atoms frame of reference is shifted by an amount of $\delta\omega_{\text{D}} = kv$ due to the optical Doppler effect,

[1] Thorlabs GC25075-K Potassium Borosilicate Reference Cell, ⌀25.4 mm × 71.8 mm
[2] Taken from the *Thorlabs webshop*.

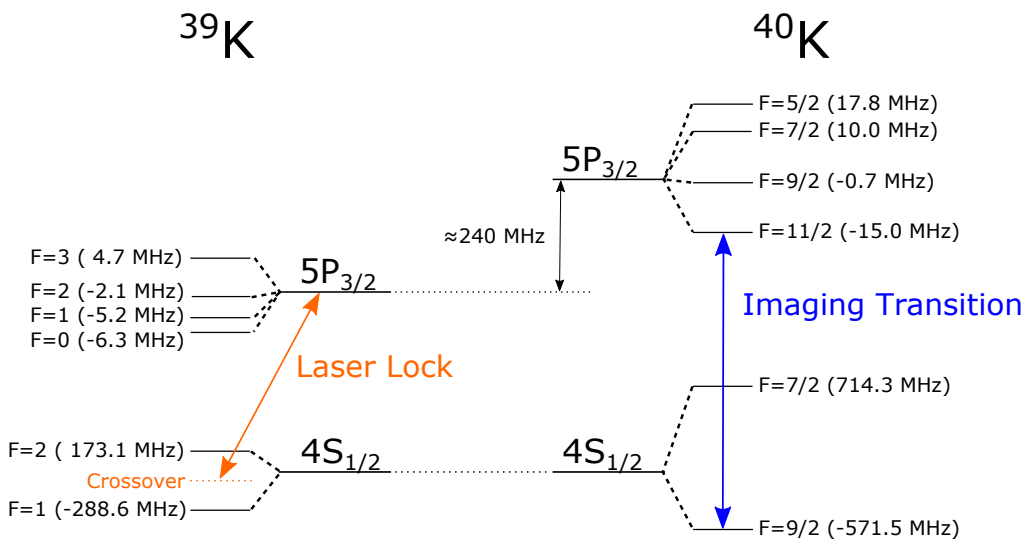

Figure 4.1: Comparison of the level schemes of the two potassium isotopes ^{39}K and ^{40}K, in order to relate the lock transition on ^{39}K to the imaging transition on ^{40}K, indicated by the orange and blue arrow, respectively. The laser lock is performed between the ground state crossover transition and the $5P_{3/2}$ excited state of ^{39}K, thereby the HF splitting of the latter cannot be resolved with the current setup. The isotope shift is approximated in a very similar setup to about 240 MHz [37]. The data for the HF structures of the ground states are taken from [65], the excited state of ^{40}K from [46], and the excited state of ^{39}K is determined from the data in [47]. The uncertainties of all values are omitted as they are negligible compared to the imprecisely known isotope shift. But in the experiment this is not an issue since the exact shift will be determined in the experiment afterwards.

with the current atom velocity v in the laboratory frame of reference. Therefore the light is only resonant with the atomic transition, with frequency ω_0, if the detuning Δ compensates the Doppler shift, thus $\Delta = \omega - \omega_0 = kv$, yielding a relation between the atom velocity and light frequency then. Subsequently, the Maxwell speed distribution can be translated into a Gaussian line shape function of the atom's absorption cross section, with its maximum value at $\omega = \omega_0$, the full width at half maximum (FWHM) $\Delta\omega_\mathrm{D} = {}^{2\omega_0}\sqrt{\ln(2)}\,u/c$, and most probable speed $u = \sqrt{2k_\mathrm{B}T/M}$ of the atoms with mass M at temperature T [25]. Inserting the numbers for ^{40}K at room temperature lead to a fractional width of $\Delta\omega_\mathrm{D}/\omega_0 \approx 2 \times 10^{-6}$, respectively $\Delta\omega_\mathrm{D} \approx 2\pi \times 1.45\,\mathrm{GHz}$ for the blue D2 line, which is more than three orders of magnitude broader than the natural linewidth Γ. For ^{39}K it is slightly worse due to the lower mass, making it impossible to resolve any HF structure without compensation of the Doppler broadening. Additionally, as it is an inhomogeneous broadening mechanism, i.e. only atoms in the velocity range $(v, v + \Delta v)$, corresponding to the appropriate detuning $\Delta = kv$ and velocity spread $k\,\Delta v \approx \Gamma$, interact with the monochromatic light field, leading to an effective reduction of the absorption cross section. Thereby the following relation between the cross sections

with and without Doppler broadening can be given, considering the on-resonance case $\omega = \omega_0$ [25]

$$\frac{\sigma_{\text{Doppler}}}{\sigma_0} = \sqrt{\pi \ln(2)} \frac{\Gamma}{\Delta\omega_{\text{D}}}. \tag{4.1}$$

Thus, for ^{40}K on the blue D2 line one can obtain approximately a factor of 1200 at room temperature, which implies that only about 0.1 % of the atoms are in the appropriate velocity class to interact with the monochromatic light field. In comparison, the IR D2 line exhibits a reduction ratio of roughly 120. Additionally, by regarding Table 2.1 and the 28 times smaller cross section σ_0, the effective cross section σ_{Doppler} of the blue transition reveals an overall 280 times smaller value compared to the effective cross section of the IR D2 line, which finally leads to a much weaker spectroscopy signal. To partly compensate for that the vapour cell is heated well above room temperature, leading to a higher vapour pressure, subsequently to an increase in density and finally to a stronger absorption signal [37]. Whereas the effect of the density increase with temperature T, is much stronger than the reduction of the atom light interaction due to the increment of $\Delta\omega_{\text{D}}$ in Eq. (4.1). But there is an upper limit for the temperature increase. Firstly, it is technically limited due to the withstand capabilities of the reference cell material and practically more limiting is a too high optical density at the upper end. However, the optimal temperature is chosen afterwards by maximizing the SNR of the error signal.

Heating the Reference Cell

The heating is achieved by running current through an amount of copper wire spooled separately on both sides of the cell, which are thereby kept in place with some high temperature resisting tape. Further, to ensured that cooled potassium vapour less likely condenses on the transmission windows, the space in the middle of the cell is not covered with heating wires, as depicted in Fig. 4.2. Next, underneath the heating wires thin aluminium foil is placed to distribute the heat more evenly. But it is crucial to keep both sides at the same temperature to further avoid condensation on either window. Therefore two NTC resistors are used to measure the temperature and in order to get a more accurate reading of the glass rather than the wire's temperature, they are placed slightly beside them. Then the whole cell is wrapped into a few layers of aluminium foil and will finally be covered by an isolating box to reduce temperature fluctuations even more[3]. To minimize the magnetic field generated by the coiled copper wires, it is important to spool them antiparallel onto the cell, which can be done by bending the wire in half prior coiling and paying attention in not overlapping the wires.

The required length and diameter of the wires is roughly estimated via consideration of the thermal losses at the desired cell temperature. The major part is given by the thermal radiation, with power P_{th}, described by the well-known Stefan-Boltzmann law,

[3] Usually a box out of thick pasteboard is sufficient to greatly reduce the temperature fluctuations due to environmental influences, wherefore it is not necessary to implement a control loop. Moreover applying a constant, but separately adjusted current on both sides is usually sufficient.

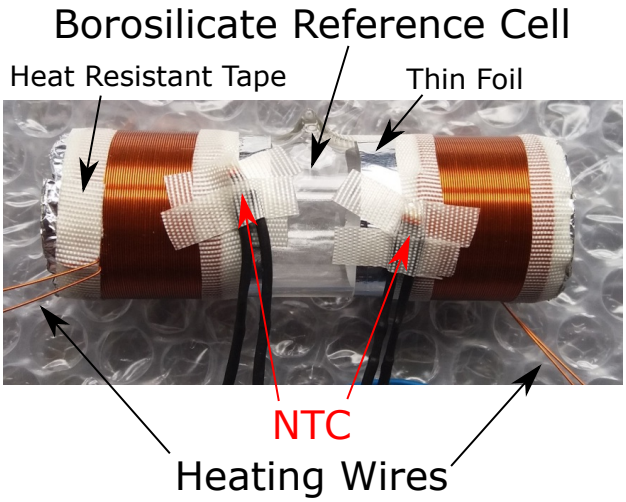

Figure 4.2: The potassium reference cell is heated by passing current through some copper wires spooled on both sides of it. The temperature is measured with two NTCs and the magnetic field generation is minimized by coiling the wires antiparallel onto the cell. Thin heat conducting foil underneath the wires ensures a more even heat distribution.

resulting in a value of $P_{\text{th}} \approx 5\,\text{W}$ for $T \approx 70\,^{\circ}\text{C}$ and a cell size of $\varnothing 25.4\,\text{mm} \times 71.8\,\text{mm}$. The second part is given by natural convection $P_{\text{conv}} = \alpha_{\text{htc}} A \Delta T \approx 1.5\,\text{W}$, with the temperature difference ΔT, the surface area A, and the heat transfer coefficient α_{htc} roughly approximated to[4] $\alpha_{\text{htc}} \approx 5\,\text{W}\,\text{m}^{-2}\,\text{K}^{-1}$. Thermal conductivity as third process of heat transfer is neglected, as the cell mount[5], consisting of three adjustable fingers, is just minimally touching the cell. Next, the applied voltage U, to achieve an electrical power of at least $P_{\text{total}} = 7\,\text{W}$, should be near $U \approx 12\,\text{V}$ to conveniently handle it with a standard power supply, whereby the necessary resistance is calculated via Ohm's law. To ensure a slightly colder spot at the middle of the cell, just $^2/_4$ to $^2/_3$ of the cell's length should be covered with copper wires, leading to an equation containing the wire diameter, the number of turns, and the wire length. Together with the electric conductivity of copper an equation system can be established and solved for the diameter and length of the wire. Then the closest value conveniently available is chosen to be $\varnothing 0.3\,\text{mm}$ in diameter, with a required length of 9 m to achieve a resistance of $\approx 2.5\,\Omega$. Thereby enough margin is left in order to achieve higher temperatures with a maximum voltage of 12 V. Practically, a dual-output power supply with an adjustable current limit is used, whereas the temperature is increased in small steps to the desired value while keeping the left/right NTC values as close as possible. After small optimizations over a longer period of time the temperature should have stabilized and it is usually not necessary to implement a control loop.

[4] Thereby the ideas provided by `https://www.schweizer-fn.de/waerme/waermeuebergang/waerme_uebergang.php` are used.

[5] Thorlabs LH1/M Adjustable Lens Mount

Now, the idea of saturated absorption spectroscopy is to divide the laser beam, with frequency ω, into two parts, the one with higher intensity ($I > I_{\text{sat}}$) is called the *pump beam* and the other one with lower intensity ($I \ll I_{\text{sat}}$) is called the *probe beam*. The two beams are then aligned on each side of the cell in counterpropagating directions, hence the Doppler shift contributes with different sign but same absolute value. Therefore only the atoms in the velocity range $(0, 0+\Delta v)$ can be resonant to both beams simultaneously, what is the case when the laser frequency meets the resonance condition $\omega \approx \omega_0 \pm \Gamma$, assuming a TLS for now. Then the pump beam *burns a hole*[6] in the ground state population for atoms near zero velocity, whereas the absorption of the probe beam is reduced subsequently, as it addresses the same atom velocity class, thus, visible as a narrow positive peak on the photodiode signal, which is recording the probe beam. Further away from the resonance the probe and pump beams are not acting on the same atom velocity classes anymore and the photodiode records the residual Doppler-broadened absorption again [66, 25].

Next, a system with a single excited state and two ground states separated by less than the Doppler width is considered. Then a so-called crossover peak can be recorded, which is located exactly midway between the two transitions. This occurs as the pump beam addresses two different velocity classes on the two transitions, one compensates the red shift of transition one and the other one the blue shift of transition two. The population of each ground state is pumped into the corresponding other ground state and as the probe beam is resonant exactly to the corresponding other transition, it exhibits a much higher attenuation due to a higher population density and therefore a negative peak occurs in the spectroscopy signal. If the considered three-level atom has a single ground state, but two excited states the emerging crossover peak is positive because the ground state population is reduced and the probe beam again addresses the corresponding other transition than the pump beam, due to the oppositely signed Doppler shift. Nevertheless, the spectroscopy signal can be considered Doppler-free then, the recorded peak is usually still broader than the natural linewidth. Whereas two prominent explanations are given by the power and pressure broadening [25].

With the setup shown in Fig. 4.3 a Doppler-free spectroscopy signal is recorded and depicted in Fig. 4.4, whereas the residual Doppler envelope, occurring due to experimental imperfections like beam misalignment or bad beam shapes, has been subtracted already. The power-broadening factor, given by $\sqrt{1 + I/I_{\text{sat}}}$, where I represents the sum of the probe and pump beam intensities, for the used setup can be estimated to a linewidth of $\Delta\omega_{\text{pow}} \approx 8 \cdot \Gamma \approx 2\pi \times 10\,\text{MHz}$, implying a pump beam intensity much bigger than the saturation intensity. Generally, one wants to avoid too high intensities in order to keep the power broadening small, but for this particular spectroscopy signal the setup was optimized to achieve at most a high peak-to-peak value and a broadened transition yields a stronger interaction while scanning the laser frequency through the resonance.

[6] The population density of the ground state as a function of the atom velocity is selectively reduced for a small velocity range. In this case it is done via excitation by means of the pump beam, wherefore a *hole* is left in the population, thus known as hole burning. The strongest effect can be seen, if the pump beam is intense enough to saturate the transition of the atoms in the corresponding velocity class.

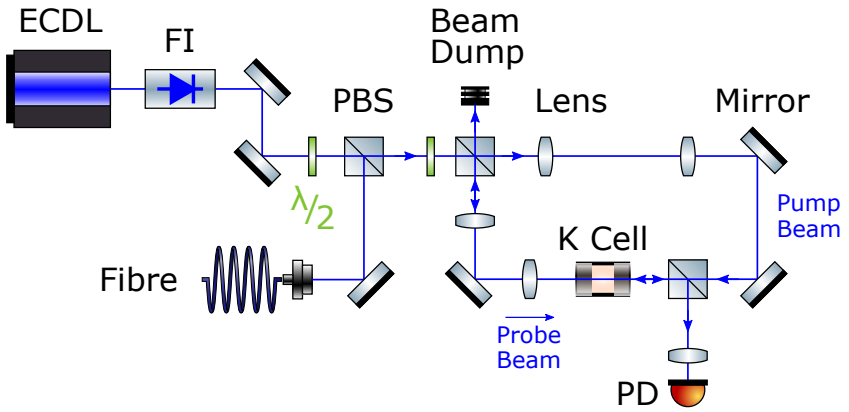

Figure 4.3: Optical setup for saturated absorption spectroscopy. As a single-mode (SM) blue laser source a homemade diode laser in Littrow configuration is used. After the Faraday isolator (FI) the beam is split into two parts with a polarizing beam-splitter (PBS) and guided on the one hand to the spectroscopy setup and on the other hand, via a SM fibre, to a wavemeter or spectrometer. With the second half-wave plate and PBS combination the pump and probe beam is separated and guided on each side of the heated potassium cell, indicated by the little arrows. With two 4f telescopes and several mirrors the two counterpropagating beams are carefully overlapped inside the cell and due to the orthogonal polarizations of the two beams it is possible to fully guide the probe beam to a photodiode (PD) via a third PBS, whereas the pump beam is dumped in a beam dump.

However, the plot in Fig. 4.4 was mainly recorded for the demonstration of the saturated absorption spectroscopy and more importantly to calibrate the frequency axis to the time axis of the oscilloscope, subsequently the error signal. For that purpose the accuracy of the spectroscopy is sufficient.

Next, the linewidth $\Delta\omega_{\text{coll}}$ due to collision broadening, also known as pressure broadening, can be approximated by $\Delta\omega_{\text{coll}} = \Gamma + 2n\sigma_{\text{coll}}\bar{v}$ [25], with the mean velocity $\bar{v} \approx 400\,\text{m}\,\text{s}^{-1}$, the collision cross section $\sigma_{\text{coll}} = 4\pi a^2 \approx 5 \times 10^{-16}\,\text{m}^{-3}$ [67], the scattering length a, and the atom number density $n \approx 2.4 \times 10^{15}\,\text{m}^{-3}$ utilizing the ideal gas law. Inserting the numbers, results in a completely negligible effect in the kHz-regime because of the very low pressure in the reference cell, thus $\Delta\omega_{\text{coll}} \approx \Gamma$.

Considering Fig. 4.4, the HF structure of the $5P_{3/2}$ excited state of ^{39}K cannot be resolved and therefore also needs to be taken into account as "broadening" of the recorded spectroscopy signal, with an approximate value of 10 MHz for feature A, 3 MHz for feature B, and 8 MHz for feature C due to the different HF states involved, as seen with the level scheme in Fig. 4.1.

Finally, the linewidth of the laser needs to be considered too. With respect to the setup in Fig. 4.3, the ECDL is yet operated in an unlocked condition, i.e. without calibration to an external reference. Additionally, only an upper bound of the laser linewidth, in particular 7.5 MHz, can be stated yet, given by the resolution limit of the

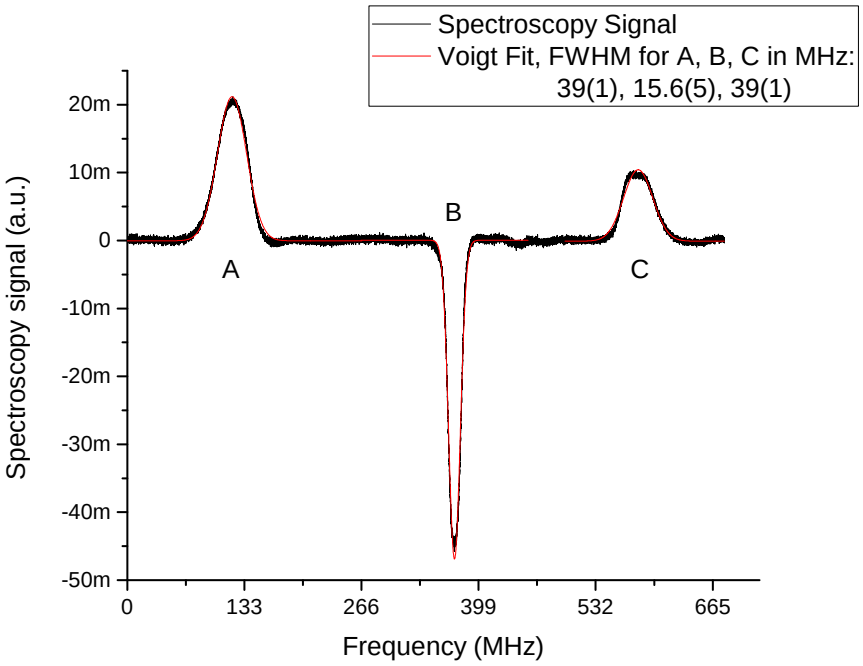

Figure 4.4: Saturated absorption spectroscopy signal, after subtraction of the Doppler envelope or background. The potassium cell is heated to 72(1) °C and the signal is averaged over 16 shots to reduce the noise contribution. The sweep signal to tune the laser has a frequency of 20 Hz. Thereby just contributions of the most abundant ^{39}K isotope can be recorded. Thus, A is representing the transition from $|4S_{1/2}, F = 2\rangle$ to the unresolved $|5P_{3/2}, F'\rangle$ excited state manifold, with $F' \in \{1, 2, 3\}$, B the ground state crossover to the $|5P_{3/2}, F' \in \{1, 2\}\rangle$ manifold, and C the transition from $|4S_{1/2}, F = 1\rangle$ to the $|5P_{3/2}, F' \in \{0, 1, 2\}\rangle$ manifold. The peaks are fitted with a Voigt function, whereas the Gaussian contribution is dominating over the Lorentzian part. The center frequencies and FWHM values are obtained from the fit, hence the frequency axis can be calibrated with the known HF splitting of the $4S_{1/2}$ ground state from Fig. 4.1. The recorded transition linewidths $\Delta\nu$ (A, C: 39(1) MHz and B: 15.6(5) MHz) are significantly broadened due to various effects, discussed in the running text.

FPI[7] coupled via an optical fibre. Thus, compared to the extracted widths of the peaks in Fig. 4.4 the rough estimations from the considerations above are on the same order of magnitude, but admittedly the peaks are still significantly broader. Nevertheless, there are even more effects leading to a broadening of the transition, e.g. Zeeman splitting due to an external magnetic field or residual Doppler broadening. Especially the latter one would also explain the Gaussian lineshape of the peaks, as all the other effects stated so far are homogeneous broadening mechanisms resulting in a Lorentzian shape. Residual Doppler broadening can occur if the probe and pump beams are mismatched, thus either the spatial profiles are not matching sufficiently well or the beams are not collinear inside

[7] Thorlabs Scanning FPI SA200-3B, with 1.5 Ghz FSR and > 200 Finesse.

the cell. Whereas the effect of the latter is minimized by careful beam alignment, the former cannot be minimized that easy because on the one hand the path lengths of both beams differ significantly and on the other hand the ECDL has an unfavourable spatial profile, as it is not lasing in the transverse Gaussian ground mode. But as long as the pump beam can saturated the atoms where the probe beam is probing, the influence should be small.

4.1.2 Modulation Transfer Spectroscopy (MTS)

Directly using a Doppler-free absorption peak as a reference for a laser lock has two distinct disadvantages, firstly one cannot distinguish whether the frequency is drifting up- or downwards because of the symmetry of the peak and secondly the signal is very sensitive to external fluctuations especially the optical power. Therefore it is favourable to deduce an error signal through phase modulation together with a phase-sensitive detector [68], e.g. modulation transfer spectroscopy with the setup depicted in Fig. 4.5. Thus, the phase of the pump beam is modulated by passing through an electro-optic modulator (EOM)[8] driven by a local oscillator (LO). The LO generates a sine wave with constant frequency $f \approx 1\,\mathrm{MHz}$, whereas best results are achieved by choosing a frequency below but near the natural linewidth of the transition, with $\Gamma \approx 2\pi \times 1.2\,\mathrm{MHz}$ [63]. To enhance the modulation due to the electro-optic effect a RLC resonance circuit is attached to the EOM crystal. Since the crystal electrically mainly acts as a capacitor C, just an appropriate coil with inductance L needs to be added. The resistance R is included a priori because of the non-ideal component behaviour, but should be kept low in order to maximize the resonance magnification. The resonance frequency of a simple LC circuit is given by $\omega_{\mathrm{LC}} = \sqrt{LC}^{-1}$, but the capacitance of the crystal is too low to be measured adequately without special equipment, therefore it is easier to utilize a network analyser and do a trial-and-error investigation with the currently available inductors. In the case of a frequency around 1 MHz together with a small capacitance usually a huge inductance would be necessary, implying high resistive losses, too. Thus, ceramic capacitors, with low series resistance, are put in parallel to the crystal to increase the capacitance and subsequently the resonance magnification with respect to the voltage, which is sufficient, as the electro-optic effect is in turn dependent on the electric field across the crystal, hence on the applied voltage and not on the current nor the electrical power [42]. Finally, the resonance frequency of the circuit could be set to $f \approx 1.02(5)\,\mathrm{MHz}$ and the magnification to 30(2) dB, measured with a network analyser[9].

Additionally, to minimize the reflection losses at the EOM facets, a crystal with two parallel Brewster ends at 65.6° is used, what is advantageous compared to an AR coating because it reduces the so-called *etaloning effect*, which can occur whenever two parallel surfaces are present along the beam path. Thus, interference can lead to resonance effects and subsequently reduces the reliability of the spectroscopy setup. Thereby the

[8] LiNbO3 phase Modulator with size $2 \times 40 \times 2\,\mathrm{mm}$ and Chrome/Gold electroded sides from Döhrer Elektrooptik GmbH

[9] HP Agilent 3577 Network Analyzer

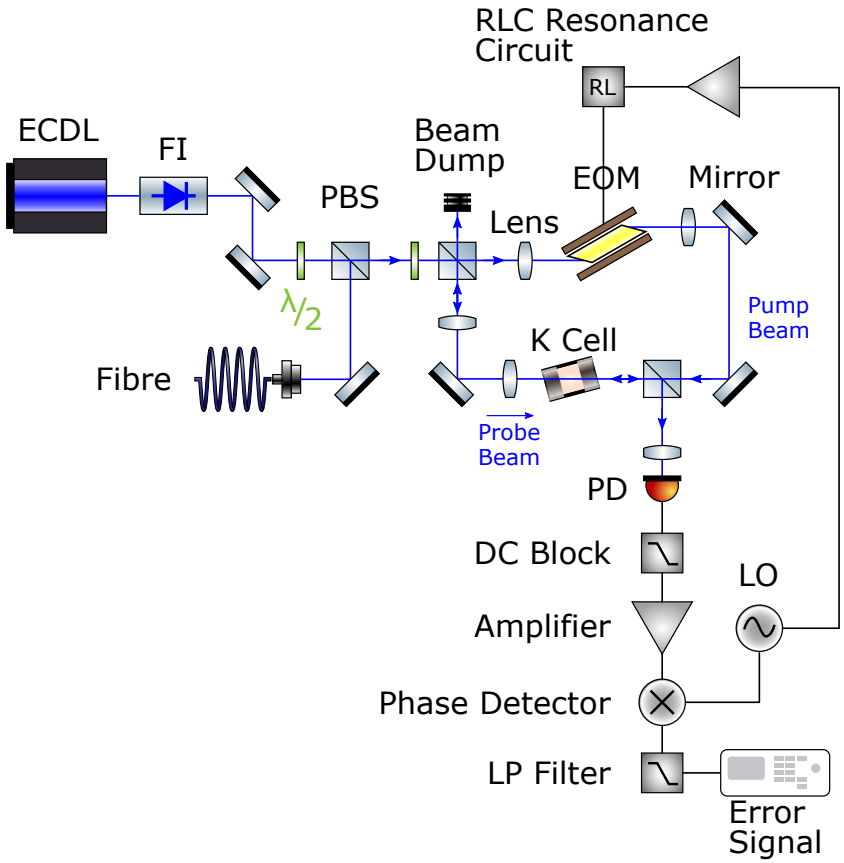

Figure 4.5: Optical setup for MTS. With respect to the setup for saturated absorption spectroscopy in Fig. 4.3, the pump beam is phase modulated by an EOM (electro-optic modulator) with parallel Brewster ends driven by a local oscillator (LO) as well as enhanced by a RLC resonance circuitry. With the potassium atoms acting as a nonlinear medium the modulation is transferred via a four-wave mixing scheme to the probe beam [63] and is detected by the photodiode (PD). After subtracting the DC component from the PD signal it is amplified and feed into a phase detector together with the LO signal. Thus, the signal is demodulated and results in the desired error signal after a low-pass (LP) filter. The relative phase between the LO and PD signal can be adjusted together with the amplitude of the LO.

utilized blue LD is especially sensitive to back-reflections, wherefore the potassium cell is installed under an angle, too.

With the EOM driven by a sinusoidal source, with frequency ω_m considered as modulated sideband frequency, first order sidebands at frequencies $\omega_c \pm \omega_m$ are imprinted on the spectrum of the pump beam, with (optical) frequency ω_c considered as carrier frequency, whereby higher order sidebands usually are negligible. Thus, with a collinear alignment of the pump and probe beam inside the vapour cell, nonlinear interactions are possible and if third order nonlinearities are strong enough, they lead to a generation of a *fourth wave* and subsequently the sidebands can be transferred to the probe beam [63, 69]. Second order processes would not be sufficient, as two frequency components of

the pump and one of the probe beam are necessary to generate a frequency component with frequency $\omega_c \pm \omega_m$ of the probe beam. This behaviour can easily be imagined by trying to achieve a frequency component $\omega_c \pm \omega_m$ of the probe just by calculating the sum and difference of the available components of the pump: $\{\omega_c, \omega_c \pm \omega_m\}$ and of the probe: $\{\omega_c\}$.

However, a fast enough photodiode, with a bandwidth higher than the modulation frequency, together with a homemade amplifier circuit is used to detect the modulated probe beam. Afterwards, from the electrical signal the DC component, which en passant contains the saturated absorption signal, is removed with a bias tee[10] and the AC signal is amplified twice[11] before being fed into a phase detector[12] together with the LO signal, resulting in a signal proportional the the phase difference. Then a homemade Butterworth low-pass filter with a 1 MHz cutoff frequency together with another low-pass filter[13] with a 0.3 MHz passband frequency is used to remove higher frequency components from the mixing process as well as to reduce the noise level at higher frequencies. The obtained error signal, as shown in Fig. 4.6, can be well described by the derivative of the absorption peak [68] and is well-suited to be used as a frequency reference because the peak center is located exactly at the zero crossing of the signal.

Referring to [68], the strongest signals should be obtain with closed transitions, whereas usually crossover transitions are greatly suppressed, but in the case of the blue D2 line all available transitions are open. Hence, after several optimization steps including changes in cell temperature, pump/probe beam powers and diameters, different light polarizations inside the cell, and some photodiodes with different bandwidths, it turned out that the crossover transition exhibits the strongest error signal and is therefore chosen for subsequent laser lock. Further, the best SNR was obtained with

- a focused beam through the EOM crystal and a beam diameter just small enough not to be clipped at the crystal ends;
- a collimated pump and probe beam through the potassium cell, with an approximate diameter of 1 mm, a pump/probe beam power ratio of at least 4, and a probe beam power of at least 1 mW;
- and a potassium cell temperature of 72(1)°C.

But all other combinations with different beam shapes, i.e. collimated or (slightly) focused beams, and different light polarizations through the EOM crystal as well as potassium cell did not make a huge difference in the SNR, after a obligatory optimization of each combination in terms of beam alignment, LO voltage, relative phase of the LO, and pump/probe beam power ratio. Although the signal should usually improve by just expanding the beams inside the reference cell, with keeping the beam power constant [63], but it is mostly related to closed transitions, which are not available on the blue D2 line.

[10] Mini-Circuits Bias-Tee ZFBT-6GW-FT+
[11] Mini-Circuits Low Noise Amplifier ZFL-500LN and Mini-Circuits Monolithic Amplifier ERA-3SM+
[12] Mini-Circuits Phase Detector ZRPD-1
[13] Mini-Circuits Low-Pass Filter LPF-B0R3+

However, as the error signal always can be additionally amplified, the setup needs to be optimized in relation to the SNR not the peak-to-peak value, as long as the electronic noise is negligible, which can be figured out easily by monitoring the error signal and blocking once the pump, then the probe beam. For the former the optical together with the electronic noise is visible, while for the latter just the electronic noise contributes.

Next, from the error signal depicted in Fig. 4.6 a few laser parameters can be deduced, subsequently. Firstly, the slope of the zero crossing sets the limit of the overall servo

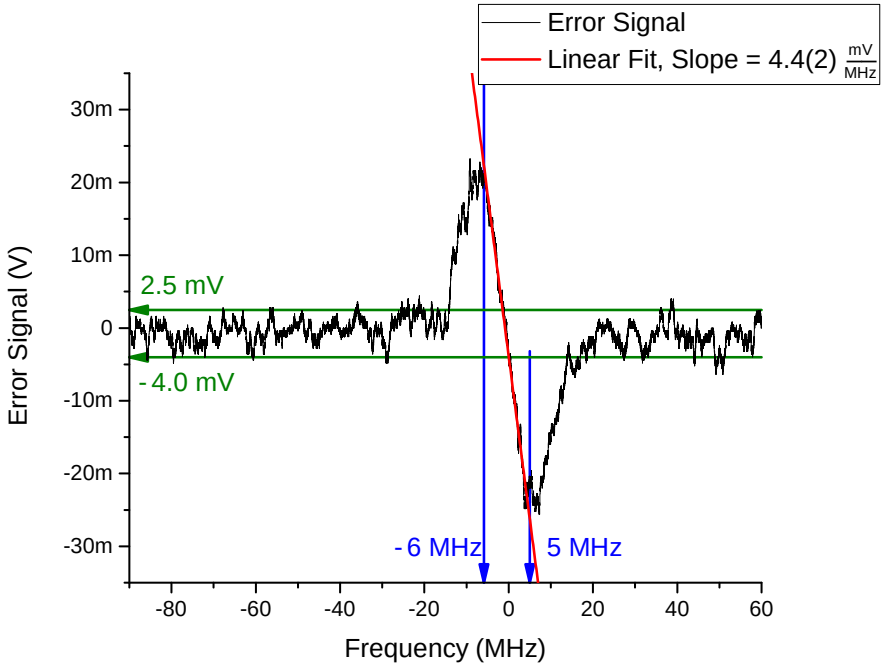

Figure 4.6: Modulation transfer spectroscopy signal of the ground state crossover transition of ^{39}K. The potassium cell is heated to 72(1) °C and the sweep signal to tune the laser has a frequency of 30 Hz. The frequency axis can be calibrated with the known HF splitting of the $4S_{1/2}$ ground state similar to the saturated absorption spectroscopy, whereas its zero point is arbitrarily set to the zero crossing. A linear fit applied to the error signal facilitates a correlation between voltage and frequency fluctuations, with a slope of 4.4(2) mV MHz^{-1}. The peak-to-peak noise voltage is marked with green arrows and can be approximated to 6.5(10) mV. Finally, the blue arrows denote the capture range of approximately 11 MHz.

gain of the locking system, wherefore steeper slopes are preferable, as the reduction of frequency fluctuations can be made higher when the laser is locked [68]. In the case of Fig. 4.6 the slope is relatively weak and not really sufficient to narrow down the laser linewidth substantially, but it is suitable for a low frequency lock of the laser to an absolute reference. Further, the capture range of 11 MHz can be declared as the frequency region where the slope of the error signal does not change its sign, thus the laser stays locked while the fluctuations are smaller than the capture range. Clearly, a bigger capture range is favourable as long as the slope stays the same, implying a

higher amplitude of the error signal, which is a priori advantageous. Finally, the voltage amplitude of the noise together with the slope can be used to express an estimation of the laser linewidth on the time scale of a few milliseconds. Thus,

$$\Delta\nu \approx \frac{6.5}{4.4}\,\mathrm{MHz} \approx 1.5(2)\,\mathrm{MHz}, \tag{4.2}$$

assuming a negligible electronic noise contribution.

On the long-term time scale a wavemeter[14] with an absolute accuracy of 0.2 pm, respectively 200 MHz is used, revealing infrequent changes on the order of 0.2 pm over a ten seconds period of time. With respect to the time scale, thermal influences from the environment are a possibility, but can be compensate easily even with a weak and slow lock to the reference cell. Thus, with that done, the frequency stays below the resolution limit of the wavemeter over at least a four hours period of time, whereas the wavelength was not monitored for a longer period of time.

To establish a laser lock, i.e. a closed feedback loop, the error signal is fed into a homemade two-channel PID controller with widely adjustable parameters, whereas one channel is used to control the piezo voltage of the ECDL and the other one to control the current of the LD. Both are correlated to the frequency of the ECDL and therefore the feedback loop can be closed. The parameters of the PID circuit need to be chosen iteratively and are strongly dependent on the individual system, wherefore they are not stated here. However, for the piezo voltage usually a small integral coefficient is sufficient, as the influence on the light frequency by the piezo voltage is much slower than the diode current and usually should just maintain a slow absolute frequency stability. The PID channel for the current can be optimized by monitoring the noise of the error signal while increasing the proportional and integral part. A too high value leads to an effectively positive feedback and the frequency noise increases again. A differential component can be added to increase the phase margin after acceptable values for the proportional and integral parts are found. Thereby both can be increased further with a differential part present until the same phase margin is reached as without, leading to an overall faster PID loop.

4.2 Complete Optical Setup

With an ECDL in Littrow configuration locked to a reference cell by MTS, part of the light is branched off, with a half-wave plate along with a PBS, and guided into an AOM in double-pass configuration, depicted in Fig. 4.7. The frequency shifted beam is coupled into a polarization-maintaining (PM) fibre connected to the experiment main chamber. Regarding the AOM branch only, the first half-wave plate is used to optimize the transmission through the subsequent PBS. The following two mirrors guide the beam through the AOM crystal, whereby two lenses in 4f configuration adapt the diameter in order to maximize the diffraction efficiency. By minding the clear aperture, a bigger beam

[14] HighFinesse Wavelength Meter WS/6-200

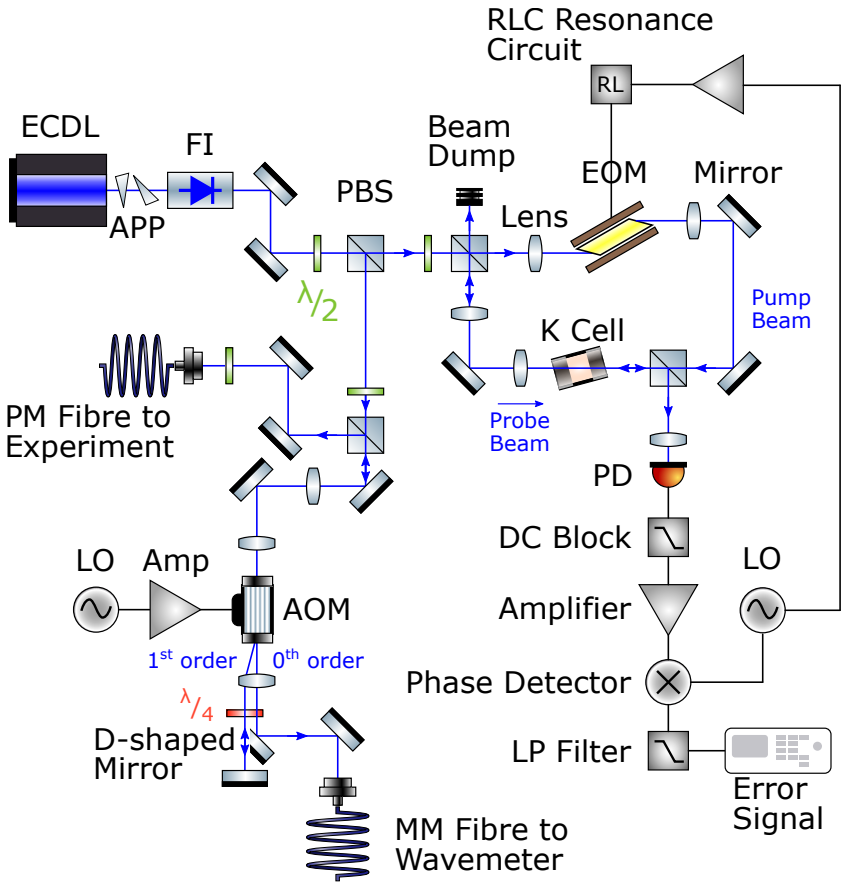

Figure 4.7: Complete optical setup of the laser source for imaging potassium in the blue regime. With respect to the MTS setup, shown in Fig. 4.5, a branch is added for an AOM in double-pass configuration as well as a fibre coupling stage with a polarization-maintaining (PM) fibre. The residual 0^{th} order beam after the AOM is still sufficient for a wavemeter coupled via a multi-mode (MM) fibre. For the sake of completeness the anamorphic prism pair (APP) used for beam shaping is included too.

yields a higher efficiency, but the dynamic response decreases as well, due to the finite acoustic velocity. But in this setup the dynamic response is negligible since the AOM is operated with a single frequency signal without the necessity of signal modulations. Nevertheless, the diffraction angle depends, inter alia, on the acoustic frequency, thus on the LO signal, wherefore a cat-eye lens positioned at its focal distance behind the AOM is introduced. Next, the quarter-wave plate is passed twice and adjusted to rotate the light polarization by 90 ° in total. Thereby, after passing the AOM a second time only the light fraction, which is shifted twice, is in line with the incoming beam and therefore guided to the fibre via the PBS. A wave plate prior to the fibre coupler is used to align the polarization angle to the PM fibre.

The applied parameters of the ECDL are: $T_{\text{LD}} \approx 42.5(2)\,^{\circ}\text{C}$, $i_{\text{LD}} \approx 70(2)\,\text{mA}$, and

$P_{\text{opt}} \approx 26.2(3)\,\text{mW}$. Thereupon, the APP[15] exhibits a transmission efficiency of approximately 85 % and the optical isolator[16] about 84 %, which are still within the manufacturers specifications. Therefrom approximately 9 mW is spent for the MTS-part and another 9 mW for the AOM branch, leading to an optical power of approximately 1 mW at the experiment via a PM single-mode fibre. Unfortunately the fibre coupling efficiency is about 50 %, mostly due to the bad spatial profile of the LD. Additionally, the AOM shows a double-pass diffraction efficiency of roughly 30 %, including some significant losses due to facet reflections and absorption. By subtracting out these losses a single conversion efficiency of about 65 % can be achieved, which is not exceptional but acceptable regarding an 80 % single-pass efficiency.

In the following chapter the available laser power is used to attempt absorption as well as fluorescence imaging of potassium ^{40}K on the blue D2 line.

[15] Thorlabs PS873-A N-KZFS8 Unmounted Anamorphic Prism Pair
[16] Thorlabs IO-3D-405-PBS Free-Space Isolator

5 Blue Imaging of ^{40}K

To attempt blue imaging of ^{40}K a circularly polarized laser beam with at most 1 mW optical power and a linewidth comparable to the natural linewidth of the transition is available. Although, evidently not the ideal conditions for an imaging laser, it should be sufficient for some absorptive images. In return, the saturation effects are clearly negligible at this low intensities, with respect to the properties of the D2 line, summarized in Table 2.1.

At first, the potassium atoms are collected in a 3D MOT in the main chamber operating on the IR D2 line, thereby the pump and repump frequencies, depicted in Fig. 2.5, are incorporated into the MOT beams. Thus, with a loading time of 3 s typically 2×10^6 atoms of ^{40}K can be collected. Next, the MOT is compressed[1] within 4 ms by ramping down the wavelength detuning, the beam intensities, and ramping up the magnetic field gradient, leading to cloud temperatures in the order of 100 µK. For further details consider [24].

In this chapter I will first present the results of resonant absorption imaging of ^{40}K utilizing the $4S_{1/2}$ to $5P_{3/2}$ transition, whereof the number of atoms can be deduced subsequently. Additionally, by sweeping the AOM frequency, thus the laser wavelength, an upper limit of the laser linewidth can be derived too. Finally, fluorescence imaging is also attempted on the blue transition.

5.1 Absorption Imaging

To test the blue imaging of Potassium ^{40}K the established imaging path for Dysprosium ^{161}Dy is used, as both wavelengths are in close vicinity to each other and the IR imaging path of ^{40}K can be utilized in parallel. At first the AOM frequency, strictly speaking the laser frequency, needs to be calibrated although the necessary shift, specified in Section 4.1, is principally known. But in the laser locking setup a manually set offset can be introduced as well as the isotope shift is not known very precisely. Utilizing absorption imaging the calibration can be done easily by sweeping through the AOM frequency and determining the surface integral of each optical density profile, yielding a relation to the detuning via the scattering cross section. Although the background light without atoms as well as probe light is already accounted by calculation of the optical depth via Eq. (2.11), it is necessary to subtract any residual offset prior surface integration. Also, in the high temperature limit ($T \gg T_\mathrm{F}$), a 2D Gaussian fit can be utilized together with the Gaussian integral to obtain the surface area of the 2D

[1] referred to as cMOT;

optical depth. The AOM frequency is swept from 363 MHz to 375 Mhz in steps of 0.5 Mhz, en passant, mind the double-pass configuration, whereas ten images are taken each in order to create statistics, with the results depicted in Fig. 5.1. An applied

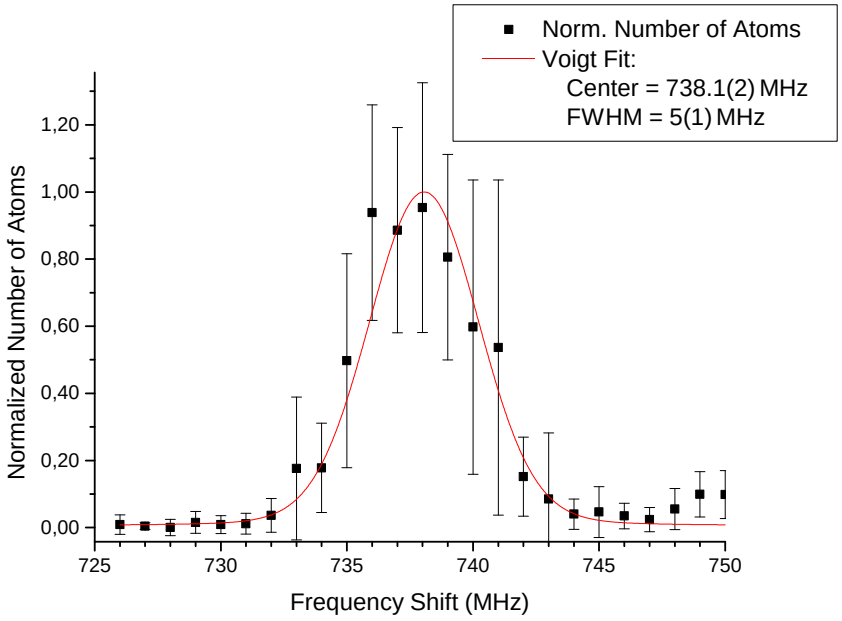

Figure 5.1: By sweeping the AOM frequency and monitoring the pseudo atom number the linewidth of the imaging laser as well as the necessary frequency shift can be obtained. Obviously the actual number of atoms is not changing, but the number of atoms seen by the imaging light because the scattering cross section is reduced by enhancing the detuning. In the plot the ordinate is normalized to the maximum of the fit function. A Voigt fit is applied to account for Gaussian and Lorentzian broadening effects.

Voigt fit reveals an optimum frequency shift of 738.1(2) MHz, which is slightly lower than the deduced value of 739 MHz. But can be explained by the offset adjustment possibility present in the controller of the laser lock, which is tuned manually, together with the imprecisely known value of the isotope shift [37]. Regarding Fig. 4.6, the residual voltage offset of the error signal can be approximated to an upper limit of 1 mV $\widehat{=}$ 0.2 MHz. Considering the isotope shift, values between 235(2) MHz and 240 MHz are termed [70, 37]. However, from the width of the fit function the linewidth of the laser can be calculated, but on the short-term time scale, since the imaging laser pulse is typically a few microseconds long. Additionally, it needs to be considered that the recorded spectrum is a convolution of the laser spectrum and the lineshape of the blue transition. Thus, $\Delta\nu_{\mathrm{FWHM}} \approx \sqrt{(5\,\mathrm{MHz})^2 - (1.2\,\mathrm{MHz})^2} \approx 5(1)\,\mathrm{MHz}$. Unfortunately it is significantly broader compared to the upper limit evaluated with Eq. (4.2). This is mostly due to the rebuild of the laser system in order to move it to another location for the imaging. Whereas the complete optical setup depicted in Fig. 4.7 remained unaltered. But the crucial issue is probably given by the rotation stage of the diode

laser box, where the grating mount is installed on because the locking screw, included to solidify the stage after adjustment, can only be tightened lightly. Otherwise it would change the alignment of the grating significantly due to the mechanical force exerted on the stage. Thereby the selection of the laser mode by rotation of the grating would become even more unreliable - virtually impossible.

However, with the AOM frequency fixed to 369 MHz ten consecutive absorption images are successfully taken, whereas the average is depicted in Fig. 5.2. Therefore the atoms are kept within the cMOT as well as the repumper stays on during the imaging process. Unfortunately the absorption signal is very weak, leading to a poor SNR, although the imaging pulse length is increased to 50 µs, with typical values near 10 µs, in other respects. As main noise source the camera read noise can be called, whereas the

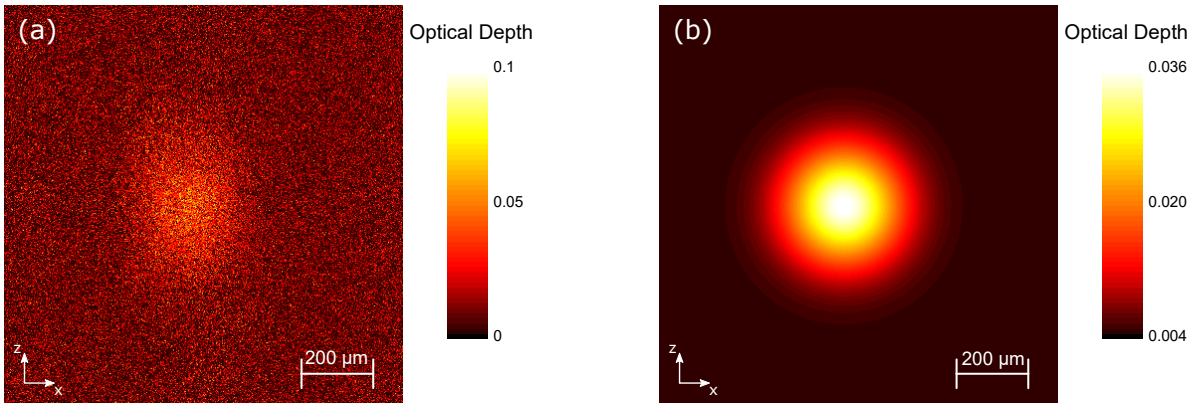

Figure 5.2: (a) Horizontal absorption imaging on the blue transition is utilized to determine the density profile of ^{40}K atoms inside the cMOT stage. The plot incorporates the average out of ten successive absorption images, whereby the IR MOT is kept active during the imaging process to achieve a higher atom density, thus bigger signal. (b) 2D Gaussian fit applied to the density profile, with an offset value of 0.0042(1), an amplitude of 0.032(1), and a width of 120(1) µm. Due to the bad SNR the fit algorithm was restricted to symmetric functions only. Also, mind the different colour map on each plot.

influences due to environmental light should be negligible, since the camera acceptance angle is small and static background values are subtracted anyway. Also fluctuations of the laser intensity are not relevant for imaging noise, as they affect the imaging area uniformly. But for the true value of the optical depth the intensity variations on the time scale of 10 µs to 50 ms, the time between taking the picture with and without atoms, are critical and should be as small as possible. However, increasing the light intensity is advantageous for a bigger SNR as the additive noise would be less significant, although the value of the optical depth stays the same. The applied intensity is roughly 0.5 % of the saturation value I_{sat}, thus clearly in the low intensity regime. Nonetheless, the absolute noise level is similar to the case utilizing IR imaging.

The weak recorded optical depth is a result of the small scattering cross section, which is on the one hand due to the properties of the blue transition and on the other hand

due to the broad laser linewidth, since the cross section drops rapidly with the detuning, thus falsely implying a smaller density. To roughly estimate the impact of the laser linewidth on the cross section a weighted average of Eq. (2.3) can be calculated, leading to a value of approximately $0.2\,\sigma_0$ compared to the on-resonance cross section σ_0 and by assuming a Lorentzian laser lineshape. For comparison a laser linewidth resembling the transition linewidth would result in a value of $0.5\,\sigma_0$. Estimating the peak optical depth of Fig. 5.2 with respect to the IR transition would lead to a value well above unity, thus IR absorption imaging would not be feasible at such high densities due to extensive light attenuation.

To validate the 2D Gaussian fit cuts through the 2D optical depth along the x and y direction are realised and depicted in Fig. 5.3. A residual offset is clearly visible via the

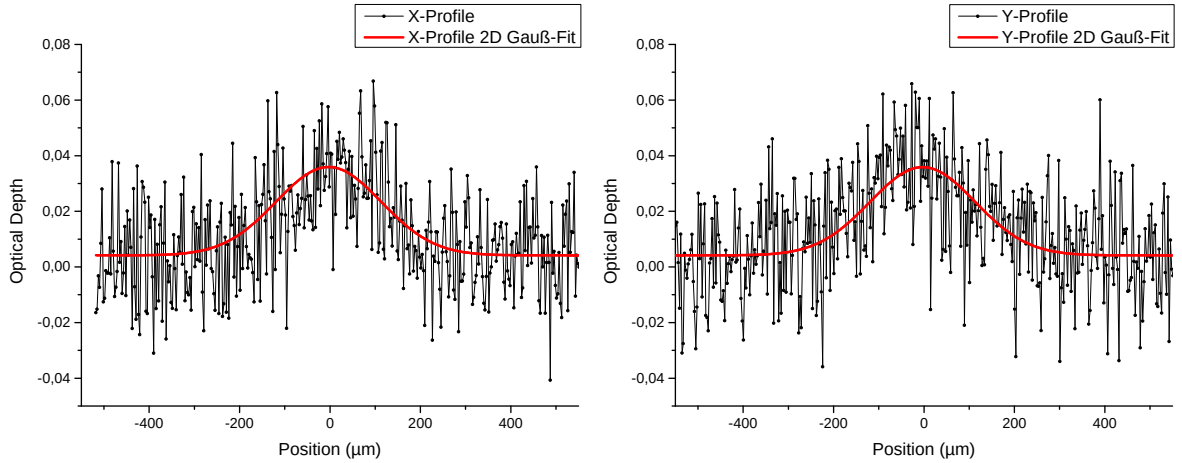

Figure 5.3: Cuts through the 2D optical depth along the x and y direction, respectively. The solid black lines connect the data points and are only displayed to guide the eye. The solid red lines show a corresponding cut through the 2D Gaussian fit function.

Gaussian fit, but an average of the imaging data apart from the atom cloud results in a similar value. By integrating over the imaging area, with prior subtraction of the offset, the number of atoms can be calculated referring to Eq. (2.12). By further considering the 2D Gaussian fit this can be done by utilizing the Gaussian integral, thus

$$N = \frac{1}{\tilde{\sigma}} \iint_{\mathbb{R}^2} \tilde{\tau}(x,z)\,\mathrm{d}x\,\mathrm{d}z \approx \frac{1}{\tilde{\sigma}} \iint_{\mathbb{R}^2} a \exp\left[-\frac{(x-x_\mathrm{c})^2}{2w_\mathrm{x}^2} - \frac{(z-z_\mathrm{c})^2}{2w_\mathrm{z}^2}\right] \mathrm{d}x\,\mathrm{d}z = \frac{a}{\tilde{\sigma}}\sqrt{2\pi w_\mathrm{x}^2}\sqrt{2\pi w_\mathrm{z}^2} = \frac{2\pi a w_\mathrm{x} w_\mathrm{z}}{\tilde{\sigma}}, \quad (5.1)$$

with the optical depth $\tilde{\tau}$, the amplitude a of the 2D Gaussian fit, as well as the center positions x_c, z_c, and corresponding widths w_x, w_z, respectively. For the cross section the prior estimated weighted-average is used, thus $\tilde{\sigma} = 0.2\,\sigma_0$. Leading to a value of $N_\mathrm{blue} \approx 1.5(2) \times 10^6$ atoms. Calculating the number of atoms via integration over the

offset-subtracted imaging data yields a similar result, in respect of the error margins. In comparison, by utilizing the IR absorption imaging system with prior TOF expansion a value of $N_{\mathrm{IR}} \approx 2.4(1) \times 10^6$ atoms can be deduced. Although N_{blue} is roughly one third off, it is at least at the same order of magnitude, whereas no calibration effort is done yet for the blue in situ imaging to account for systematic errors, as well as the blue laser intensity is not stabilized. Also the cMOT is operated simultaneously at an intensity of $0.5\, I_{\mathrm{sat,IR}}$, with the saturation intensity of the D2 line $I_{\mathrm{sat,IR}}$, thus it cannot be considered as low intensity regime and is thereby reducing the scattering probability of the blue light. Finally, the viewports of the main chamber are specifically AR coated, but with the lowest wavelength of 421 nm and not including 405 nm. Nevertheless, the influence on absorption imaging should be small, as it is assumed that the light is most probably just uniformly attenuated in intensity.

5.2 Fluorescence Imaging

Similar to the absorption imaging setup the atoms are probed within the cMOT stage, but by cause of the six times smaller probability of a direct blue photon decay, due to the unfavourable branching ratio listed in Table 2.1, it was not possible to obtain a fluorescence image. Therefore the laser beam is focused by more than a factor of two in order to attain a fluorescence signal nevertheless. The result is depicted in Fig. 5.4, with an exposure time of 0.5 s as well as the EM (electron multiplying) gain is set to 50, as an additional amplification step of the camera. By means of optical filters it is assured that the IR fluorescence light is below the detection threshold of the camera and thereby negligible.

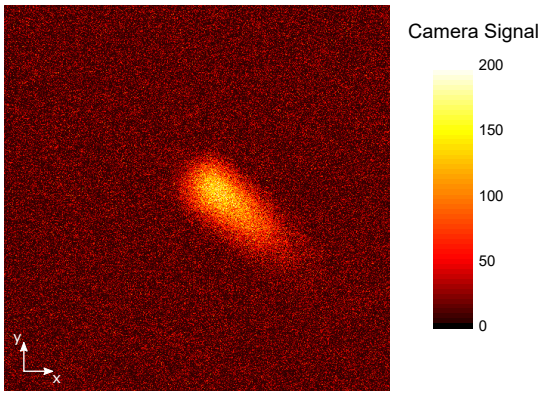

Figure 5.4: Vertical fluorescence image of ^{40}K atoms inside the cMOT stage utilizing the blue transition. Due to the small absorption cross section and unfavourable branching ratio the imaging laser is focused roughly to the size of the atom cloud in order to obtain a fluorescence signal once. But thereby the atoms are displaced significantly as well as the substantial atom losses during the 0.5 s long exposure time. The camera signal is not calibrated and displayed in arbitrary units.

6 Conclusion and Outlook

In this thesis I presented the realization of an ECDL in Littrow configuration at a wavelength of 405 nm and successful first attempts of absorption as well as fluorescence imaging of ^{40}K on the blue transition $4S_{1/2} \leftrightarrow 5P_{3/2}$. Priorly, an ECDL in cat-eye configuration on the basis of a narrow-band IF was set up, which is conceptually superior in the areas of feedback stability and cavity misalignments. But turned out to exhibit a worse tunability in connection with the used low reflection coated LD, with respect to SM operation only. Switching to an AR coated LD would most probably extend the tunability significantly [56], e.g. Sacher Lasertechnik is one of the few who offers exceptional AR coatings for blue LDs, but is demanding payment accordingly. Whereas in general the overall performance of blue LDs is just not comparable to the well-known IR counterpart, especially with respect to tunability and stability.

The laser lock is accomplished by means of MTS of a heated potassium vapour cell, whereas the error signal is sufficient to achieve an absolute reference on the long-term time scale, but insufficient for significant reduction of the laser linewidth due to the weak amplitude, respectively SNR, and slope of the signal, whereby it needs to be mentioned that an unfavourable open transition has to be utilized. A feasible approach for linewidth reduction is to add an additional high frequency feedback loop to reduce noise on the short-term time scale, more precisely a linear cavity consisting of two high-reflection coated mirrors can be utilized together with a PZT to enable cavity length tuning. Then with an additional AOM or EOM for sideband generation a laser lock can be established via the Pound-Drever-Hall method. Thereby the LD injection current is driven as fast controlling element of the laser frequency and the PZT of the ECDL as slow controlling element. To compensate for slow drifts of the reference cavity the MTS of the potassium cell is used to very slowly drive the PZT of the external cavity for absolute reference. The different bandwidths of the feedback loops are necessary in order to not interfere with each other as well as the controlling elements have a limited bandwidth, too. An alternative approach would be to lock the ECDL to the external cavity by means of the LD current as well as to the vapour cell by means of the PZT of the ECDL. Lastly, the PZT of the external cavity is driven by the error signal from the MTS, too, but on a very low bandwidth. Since both approaches require the same setup the second is slightly advantageous as the laser frequency is directly related to an absolute reference and the low bandwidth noise of the external cavity is irrelevant, too.

Further, the optical power at the experiment table is only enough for attempts of low intensity absorption imaging of dense ^{40}K clouds, yet. But some optical components in the setup of Fig. 4.7 are not especially fitted to achieve high efficiencies at a wavelength of 405 nm. As main issues the unfavourable spatial mode, respectively the beam profile, of the ECDL, the AOM for frequency shifting, and the APP can be identified. The

former strongly depends on the LD of the ECDL, whereas alignment optimizations with respect to the Gaussian ground mode yielded a much worse feedback and optimizations with respect to the optical feedback yielded a superposition of higher modes, but with a dominating Gaussian ground mode. For the second a high frequency AOM, not be confused with a high bandwidth for signal modulations, is needed for a signal frequency above 350 MHz. The achieved single-pass diffraction efficiency of 80 % is satisfactory, but with overall reflection and absorption losses slightly above 50 %, in double-pass configuration, there is room for improvement, but the used AOM is not especially optimized for 405 nm light. For the latter alternatively cylindrical lens pairs can be utilized, which can easily improve the acceptable efficiency of 85 % of the APP to good values above 90 %, but they are not as compact and as flexible, with respect to the beam magnification, as the APP. Additionally, regarding the single-stage optical isolator, efficiencies near 85 % represent typical values for the transmission of optical isolators.

Another point concerns the used rotation stage for the grating mount of the ECDL, where the worm drive offers a too low reduction ratio and too high reverse play, which can be replaced in order to achieve a finer and more reliable wavelength selection. Alternatively, for example PZTs can be engineered to the worm screw and facilitate a fine adjustment, too.

However, an alternative for blue LDs is the method of second-harmonic generation (SHG) utilizing a nonlinear crystal pumped by an ECDL incorporating an IR LD [71]. Thereby a feasible approach comprises a beta-barium borate (BBO) or lithium triborate (LBO) crystal put into a ring cavity for resonator-enhanced SHG. Both crystal types and IR LDs are widely available, offer decent amount of optical power, and are usually cost-effective compared to a decent blue LD. Nevertheless it adds an additional stage, raising the complexity of the laser system.

Bibliography

[1] W. D. Phillips and H. Metcalf. *Laser deceleration of an atomic beam*, Phys. Rev. Lett. **48** (1982), pp. 596–599.

[2] E. L. Raab, M. Prentiss, A. Cable, S. Chu, and D. E. Pritchard. *Trapping of neutral sodium atoms with radiation pressure*, Phys. Rev. Lett. **59** (1987), pp. 2631–2634.

[3] R. Grimm, M. Weidemüller, and Y. B. Ovchinnikov. *Optical dipole traps for neutral atoms*, volume 42 of *Advances in Atomic, Molecular, and Optical Physics*, pp. 95–170. Academic Press **42** (2000).

[4] W. Ketterle, D. Durfee, and D. Stamper-Kurn. *Making, probing and understanding Bose-Einstein condensates,* in *Bose-Einstein Condensation in Atomic Gases*, volume 140 of *Proceedings of the International School of Physics "Enrico Fermi"*. IOS Press **140** (1999).

[5] M. H. Anderson, J. R. Ensher, M. R. Matthews, C. E. Wieman, and E. A. Cornell. *Observation of Bose-Einstein condensation in a dilute atomic vapor*, Science **269** (1995), pp. 198–201.

[6] C. C. Bradley, C. A. Sackett, J. J. Tollett, and R. G. Hulet. *Evidence of Bose-Einstein condensation in an atomic gas with attractive interactions*, Phys. Rev. Lett. **75** (1995), pp. 1687–1690.

[7] K. B. Davis, M. O. Mewes, M. R. Andrews, N. J. van Druten, D. S. Durfee, D. M. Kurn, and W. Ketterle. *Bose-Einstein condensation in a gas of sodium atoms*, Phys. Rev. Lett. **75** (1995), pp. 3969–3973.

[8] B. DeMarco and D. S. Jin. *Onset of Fermi degeneracy in a trapped atomic gas*, Science **285** (1999), pp. 1703–1706.

[9] A. G. Truscott, K. E. Strecker, W. I. McAlexander, G. B. Partridge, and R. G. Hulet. *Observation of Fermi pressure in a gas of trapped atoms*, Science **291** (2001), pp. 2570–2572.

[10] F. Schreck, L. Khaykovich, K. L. Corwin, G. Ferrari, T. Bourdel, J. Cubizolles, and C. Salomon. *Quasipure Bose-Einstein condensate immersed in a Fermi sea*, Phys. Rev. Lett. **87** (2001), p. 080403.

[11] C. Ravensbergen. *Creation of a Fermi-Fermi mixture of dysprosium and potassium with resonant interactions*. PhD thesis, University of Innsbruck (2020).

[12] M. Lu, S. H. Youn, and B. L. Lev. *Spectroscopy of a narrow-line laser-cooling transition in atomic dysprosium*, Phys. Rev. A **83** (2011), p. 012510.

[13] C. Ravensbergen, E. Soave, V. Corre, M. Kreyer, B. Huang, E. Kirilov, and R. Grimm. *Resonantly interacting Fermi-Fermi mixture of* ^{161}Dy *and* ^{40}K, Phys. Rev. Lett. **124** (2020), p. 203402.

[14] B. DeMarco and D. S. Jin. *Onset of Fermi degeneracy in a trapped atomic gas*, Science **285** (1999), pp. 1703–1706.

[15] M. Lu, N. Q. Burdick, and B. L. Lev. *Quantum degenerate dipolar Fermi gas*, Phys. Rev. Lett. **108** (2012), p. 215301.

[16] R. Grimm. *Efimov states in an ultracold gas: How it happened in the laboratory*, Few-Body Systems **60** (2019).

[17] J. Levinsen and D. S. Petrov. *Atom-dimer and dimer-dimer scattering in fermionic mixtures near a narrow feshbach resonance*, The European Physical Journal D **65** (2011), pp. 67–82.

[18] P. Fulde and R. A. Ferrell. *Superconductivity in a strong spin-exchange field*, Phys. Rev. **135** (1964), pp. A550–A563.

[19] A. I. Larkin and Y. N. Ovchinnikov. *Inhomogeneous state of superconductors*, Soviet Physics JETP **20** (1965).

[20] J. Wang, Y. Che, L. Zhang, and Q. Chen. *Enhancement effect of mass imbalance on Fulde-Ferrell-Larkin-Ovchinnikov type of pairing in Fermi-Fermi mixtures of ultracold quantum gases*, Scientific Reports **7** (2017), p. 39783.

[21] G. Sarma. *On the influence of a uniform exchange field acting on the spins of the conduction electrons in a superconductor*, Journal of Physics and Chemistry of Solids **24** (1963), pp. 1029–1032.

[22] K. Gubbels and H. Stoof. *Imbalanced Fermi gases at unitarity*, Physics Reports **525** (2013), pp. 255 – 313.

[23] K. Aikawa, A. Frisch, M. Mark, S. Baier, R. Grimm, and F. Ferlaino. *Reaching Fermi degeneracy via universal dipolar scattering*, Phys. Rev. Lett. **112** (2014), p. 010404.

[24] C. Ravensbergen, V. Corre, E. Soave, M. Kreyer, E. Kirilov, and R. Grimm. *Production of a degenerate Fermi-Fermi mixture of dysprosium and potassium atoms*, PHYSICAL REVIEW A **98** (2018).

[25] C. J. Foot. *Atomic Physics*. Oxford University Press (2005).

[26] D. A. Steck. *Sodium D line data* (rev. 2.2.1, November 2019). Available online at `http://steck.us/alkalidata`.

[27] W. Ketterle and M. W. Zwierlein. *Making, probing and understanding ultracold Fermi gases,* in *Ultracold Fermi Gases*, volume 164 of *Proceedings of the International School of Physics "Enrico Fermi"*. IOS Press **164** (2008).

[28] V. Dribinski, A. Ossadtchi, V. A. Mandelshtam, and H. Reisler. *Reconstruction of Abel-transformable images: The Gaussian basis-set expansion Abel transform method*, Review of Scientific Instruments **73** (2002), pp. 2634–2642.

[29] C.-L. Hung and C. Chin. *In situ imaging of atomic quantum gases,* in *Quantum Gas Experiments*, chapter 6, pp. 101–120. Imperial College Press (2014).

[30] R. E. K. Landig. *Quantum phases emerging from competing short- and long-range interactions in an optical lattice*. PhD thesis, ETH Zurich (2016).

[31] G. Reinaudi, T. Lahaye, Z. Wang, and D. Guéry-Odelin. *Strong saturation absorption imaging of dense clouds of ultracold atoms*, Opt. Lett. **32** (2007), pp. 3143–3145.

[32] M. Horikoshi, A. Ito, T. Ikemachi, Y. Aratake, M. Kuwata-Gonokami, and M. Koashi. *Accurate in situ acquisition of column density of a dense cloud of ultracold* ^{6}Li *atoms using absorption imaging*, arXiv:1608:07152v1 (2016).

[33] K. Hueck, N. Luick, L. Sobirey, J. Siegl, T. Lompe, H. Moritz, L. W. Clark, and C. Chin. *Calibrating high intensity absorption imaging of ultracold atoms*, Opt. Express **25** (2017), pp. 8670–8679.

[34] J. W. Goodman. *Introduction to Fourier Optics*, 3rd edition. Roberts & Co., Greenwood Village (2005).

[35] C.-L. Hung, X. Zhang, L.-C. Ha, S.-K. Tung, N. Gemelke, and C. Chin. *Extracting density–density correlations from in situ images of atomic quantum gases*, New Journal of Physics **13** (2011), p. 075019.

[36] A. J. E. M. Janssen. *Extended Nijboer–Zernike approach for the computation of optical point-spread functions*, J. Opt. Soc. Am. A **19** (2002), pp. 849–857.

[37] D. C. McKay. *Quantum Simulation in Strongly Correlated Optical Lattice*. PhD thesis, University of Illinois (2012).

[38] D. Jervis. *A Fermi Gas Microscope Apparatus*. PhD thesis, University of Toronto (2014).

[39] C. Chin, R. Grimm, P. Julienne, and E. Tiesinga. *Feshbach resonances in ultracold gases*, Rev. Mod. Phys. **82** (2010), pp. 1225–1286.

[40] F. Schwabl. *Statistical Mechanics*. Springer, Berlin, Heidelberg (2006).

[41] G. M. Bruun and C. W. Clark. *Ideal gases in time-dependent traps*, Phys. Rev. A **61** (2000), p. 061601.

[42] B. E. A. Saleh and M. C. Teich. *Fundamentals of Photonics*, 2nd edition. John Wiley & Sons Inc. (2007).

[43] L. D. Turner. *Holographic imaging of cold atoms.* PhD thesis, School of physics, University of Melbourne Australia (2004).

[44] M. R. Matthews. *Two-component Bose-Einstein condensation.* PhD thesis, University of Colorado at Boulder (1999).

[45] J. E. Sansonetti. *Wavelengths, transition probabilities, and energy levels for the spectra of potassium (KI through KXIX)*, Journal of Physical and Chemical Reference Data **37** (2008), pp. 7–96.

[46] D. C. McKay, D. Jervis, D. J. Fine, J. W. Simpson-Porco, G. J. A. Edge, and J. H. Thywissen. *Low-temperature high-density magneto-optical trapping of potassium using the open 4S→ 5P transition at* 405 nm, Phys. Rev. A **84** (2011), p. 063420.

[47] E. Arimondo, M. Inguscio, and P. Violino. *Experimental determinations of the hyperfine structure in the alkali atoms*, Rev. Mod. Phys. **49** (1977), pp. 31–75.

[48] R. Berends, W. Kedzierski, J. Atkinson, and L. Krause. *The radiative lifetimes of the potassium 5P, 6P and 7P states*, Spectrochimica Acta Part B: Atomic Spectroscopy **43** (1988), pp. 1069 – 1073.

[49] W. D. Phillips. Nobel Lecture: *laser cooling and trapping of neutral atoms*, Rev. Mod. Phys. **70** (1998), pp. 721–741.

[50] F. Traeger (editor). *Springer Handbook of Lasers and Optics*, 2nd edition. Springer-Verlag Berlin Heidelberg (2012).

[51] W. Demtroeder. *Laserspektroskopie 1*, 6th edition. Springer-Verlag Berlin Heidelberg (2011).

[52] A. L. Schawlow and C. H. Townes. *Infrared and optical masers*, Phys. Rev. **112** (1958), pp. 1940–1949.

[53] R. Gross and A. Marx. *Festkoerperphysik*, 2nd edition. DE GRUYTER OLDENBOURG (2014).

[54] S. Nakamura, S. Pearton, and G. Fasol. *The Blue Laser Diode.* Springer, Berlin, Heidelberg (2000).

[55] H. Sun. *A Practical Guide to Handling Laser Diode Beams.* Springer, Dordrecht (2015).

[56] H. Loh, Y.-J. Lin, I. Teper, M. Cetina, J. Simon, J. K. Thompson, and V. Vuletić. *Influence of grating parameters on the linewidths of external-cavity diode lasers*, Appl. Opt. **45** (2006), pp. 9191–9197.

[57] P. Zorabedian and W. R. Trutna. *Interference-filter-tuned, alignment-stabilized, semiconductor external-cavity laser*, Opt. Lett. **13** (1988), pp. 826–828.

[58] E. Kirilov, M. J. Mark, M. Segl, and H.-C. Nägerl. *Compact, robust, and spectrally pure diode-laser system with a filtered output and a tunable copy for absolute referencing*, Applied Physics B **119** (2015), pp. 233–240.

[59] D. J. Thompson and R. E. Scholten. *Narrow linewidth tunable external cavity diode laser using wide bandwidth filter*, Review of Scientific Instruments **83** (2012), p. 023107.

[60] X. Baillard, A. Gauguet, S. Bize, P. Lemonde, P. Laurent, A. Clairon, and P. Rosenbusch. *Interference-filter-stabilized external-cavity diode lasers*, Optics Communications **266** (2006), pp. 609 – 613.

[61] N. Watanabe, T. Kimoto, and J. Suda. *The temperature dependence of the refractive indices of* GaN *and* AlN *from room temperature up to* 515 °C, Journal of Applied Physics **104** (2008), p. 106101.

[62] M. Roewe, P. Michler, J. Gutowski, V. Kuemmler, A. Lell, and V. Haerle. *Influence of the carrier density on the optical gain and refractive index change in* InGaN *laser structures*, physica status solidi (a) **200** (2003), pp. 135–138.

[63] D. J. McCarron, S. A. King, and S. L. Cornish. *Modulation transfer spectroscopy in atomic rubidium*, Measurement Science and Technology **19** (2008), p. 105601.

[64] E. D. Black. *An introduction to Pound-Drever-Hall laser frequency stabilization*, American Journal of Physics **69** (2001), pp. 79–87.

[65] T. Tiecke. *Properties of potassium* (v1.03, June 2019). Available online at `http://www.tobiastiecke.nl/archive/PotassiumProperties.pdf`.

[66] T. W. Hänsch, M. D. Levenson, and A. L. Schawlow. *Complete hyperfine structure of a molecular iodine line*, Phys. Rev. Lett. **26** (1971), pp. 946–949.

[67] J. L. Bohn, J. P. Burke, C. H. Greene, H. Wang, P. L. Gould, and W. C. Stwalley. *Collisional properties of ultracold potassium: Consequences for degenerate Bose and Fermi gases*, Phys. Rev. A **59** (1999), pp. 3660–3664.

[68] L. Mudarikwa, K. Pahwa, and J. Goldwin. *Sub-Doppler modulation spectroscopy of potassium for laser stabilization*, Journal of Physics B: Atomic, Molecular and Optical Physics **45** (2012), p. 065002.

[69] R. K. Raj, D. Bloch, J. J. Snyder, G. Camy, and M. Ducloy. *High-frequency optically heterodyned saturation spectroscopy via resonant degenerate four-wave mixing*, Phys. Rev. Lett. **44** (1980), pp. 1251–1254.

[70] A. Behrle, M. Koschorreck, and M. Köhl. *Isotope shift and hyperfine splitting of the $4S \rightarrow 5P$ transition in potassium*, Phys. Rev. A **83** (2011), p. 052507.

[71] W. P. Risk, T. R. Gosnell, and A. V. Nurmikko. *Compact Blue-Green Lasers.* Cambridge University Press (2003).